Solvent Evaporation and Particle Deposition of Colloidal Drops in Inkjet Printing Process

A Thesis

Submitted to the Faculty

of

Drexel University

by

Viralsinh Chhasatia

In partial fulfillment of the

requirements for the degree

of

Doctor of Philosophy

January 2012

Dedications

To my wife, Unnati; my parents: Harendrasinh and Anilaben; my brother: Anup, and my colleagues and friends.

Acknowledgements

I would like to thank my advisor Prof. Ying Sun for her support and guidance throughout the course of my Ph.D. research. Her dedication and passion for fundamental research laid a solid foundation for my dissertation. I greatly appreciate her contribution to my growth as a researcher in the area of self assembly of particles in suspensions. I would also like to thank my colleagues (Abhijit, Brandon, Gabe, Gang, Han, Marie, Richard, Steve, Xin) and friends (Chris, Dion, Eric, Ersin, Jaime, Mike, Nussair) to make my stay pleasant at Hess Lab.

I greatly appreciate Prof. Nicholas Cernansky, Prof. Bakhtier Farouk, Prof. Hongseok (Moses) Noh and Prof. Adam Fontecchio for their critical assessment and positive suggestions during my candidacy exam, proposal and my defense.

I would like to thank my wife Unnati for supporting me when I was working on my dissertation. I also thank my parents Harendrasinh and Anilaben for their unwavering support during my studies.

I also appreciate the financial support of National Science Foundation (Grant CAREER-0968927).

.

Table of Contents

LIST OF TABLES

LIST OF FIGURES

LIST OF SYMBOLS

A	contact area of the deposition
A_{123}	Hamaker constant between polystyrene particle and glass in water
A_{131}	Hamaker constant between polystyrene particles in water
Bo	Bond number
C	water vapor concentration in air
C_s	saturated water vapor concentration in air
C_∞	water vapor concentration in air far away from the drop
d	drop diameter
d_n	nozzle diameter
$\frac{dR_b}{dt}$	contact line velocity
D	diffusion coefficient of water vapor in air
E	total free energy of a surface
f	friction coefficient
fF_a	friction force
F_a	total attractive force
F_d	drag force
F_{eps}	particle-substrate electrostatic force
F_{epp}	particle-particle electrostatic force
F_g	gravitational force
F_s	surface tension force
F_{epp}	particle-particle electrostatic force
F_{wps}	particle-substrate van der Waals force
F_{wpp}	particle-particle van der Waals force
g	gravitational acceleration
k_L	thermal conductivity of the liquid
k_R	ratio of thermal conductivities of solid substrate to liquid
k_S	thermal conductivity of the solid substrate
J	evaporation rate
Oh	Ohnesorge number
n	number of particles
$\mathbf{n}$	unit normal

r	particle radius
R	drop radius
R_b	base radius of a sessile drop
Re	Reynolds number
RH	relative humidity
t	time
t_0	total evaporation time
t_b	capillary relaxation time
t_d	diffusion time
t_e	inviscid inertial time
t_i	viscous inertial time
t_{pinned}	time interval of the pinned stage of an evaporating drop
$\mathbf{t}$	tangential unit vector
U_{CL}	fluid velocity near the contact line parallel to the substrate
v	velocity of evaporative flow
v_d	drop velocity
v_s	particle settling velocity
V	drop volume
We	Weber number
x	separation distance
z	particle-substrate separation distance

Greek symbols

∇_s	surface gradient
ΔH_v	specific latent heat of evaporation
ε	permittivity of water
η	viscosity
θ	contact angle
θ_A	instantaneous (dynamic) advancing contact angle
θ'_A	dynamic advancing contact angle in the presence of evaporation
θ_{ACA}	static advancing contact angle
θ'_{ACA}	static advancing contact angle in the presence of evaporation

θ_{RCA}	static receding contact angle
κ	reciprocal of Debye length
ρ	density
ρ_p	particle density
σ	surface tension
ϕ_1	surface potential of polystyrene
ϕ_2	surface potential of glass

ABSTRACT

Solvent Evaporation and Particle Deposition of Colloidal Drops in Inkjet Printing Process

Viralsinh Chhasatia

Advisor: Ying Sun, Ph.D.

Inkjet printing has garnered much attention due to its ability to dispense precise amounts of functional materials onto targeted areas. It is a low-cost and scalable manufacturing process for a wide range of applications including thin film solar cells, electronic circuits and flexible displays. To realize the potential of inkjet printing, the evaporation, contact line (CL) dynamics, and particle deposition of inkjet-printed aqueous colloidal drops have been investigated by using fluorescence microscopy and a high resolution goniometer. The results show that the relative humidity affects the extent to which the drop is able to spread, the evaporation rate at the drop surface, the evaporation-driven flow inside the drop, and finally the particle deposition morphology. The deposition behavior of inkjet-printed colloidal mixture of micro and nanoparticles on a substrate with varying wettability is investigated. It is found that particles inside an evaporating drop rearrange themselves near the CL according to their sizes, where smaller particles deposit closer to the CL. By increasing substrate wettability, particles in the bi-dispersed mixture can be further separated. Forces acting on the particles determine the role of particles in enhancing CL pinning, which ultimately determines the final deposition morphology of a bi-dispersed colloidal mixture.

The dynamics of drop coalescence, evaporation, and particle deposition of two inkjet-printed consecutive drops have been studied by jetting the second drop on the pre-wetted region of the first drop with various temporal delays and drop spacings. As drop

separation distance increases, the circularity of the deposition decreases. Moreover, a longer delay between two drops causes the formation of two separate coffee rings as more particles are pulled and deposited in the first drop region due to capillary pressure. The effect of particle shape on the deposition morphology is also studied to suppress the coffee ring effect for spherical particles.

Finally, applications of inkjet printing for conducting lines and organic solar cells are explored. The conditions under which stable lines and uniform films are formed have been examined. The knowledge obtained will benefit a wide range of applications that involve evaporation-driven assembly of complex fluids ranging from printable electronics to tissue engineering.

Chapter 1 : INTRODUCTION

1.1. Background and motivation

Inkjet printers are widely used for graphical applications in which drops of inks are jetted from a small orifice directly to a specified position on a substrate to create characters and images. Inkjet printing is a material-conserving, non-contact, maskless, additive fabrication technique that operates under atmospheric temperature and pressure. Drop formation and ejection can be performed by applying an electrical voltage in the piezoelectric printhead to generate a pressure pulse by the movement of the piezo element or by applying heat in the thermal printhead to generate a pressure pulse by a vapor bubble.

In the electronics industry, an alternative technology used to pattern function materials is photo-lithography. This multi-step process is capable of making patterns as small as 100 nm. First, a continuous layer of the functional material is applied on the substrate. Then a uniform layer of the photo-resist is coated on top of the functional material, and is allowed to form cross-link bonds. Using a photo-mask, a light pattern is applied on the photo-resist to break up the cross-linked bonds that are in contact with the light. Photo-resist with the broken cross-linked bonds is then removed by using a suitable solvent and only the resist pattern remains. This resist pattern protects the functional material from etching away during the etching step. In the end, the resist is stripped and a pattern of functional material is obtained.

In inkjet printing, however, these complex microfabrication steps are avoided, and the drop meniscus serves as a template and directs materials deposition. The printing nozzle does not come in contact with the substrate; the ejected drop travels until it

impinges on a substrate, spreading under inertia and surface tension. The ease of fabrication via low temperature evaporation and/or solution processing during inkjet printing opens up a potentially wide market for devices made of these materials since they can be integrated onto or into other products such as textiles, packages, and portable electronics. The major advantages of inkjet printing over other commonly used low temperature deposition techniques such as spray deposition and spin coating is its ability to deliver droplets of well-controlled size and volume onto desired locations and enables high throughput production of heterogeneous structures in a roll-to-roll format. One of the applications of inkjet printing is to fabricate low cost electronics on flexible substrates, thus, replacing the silicon-based photolithography method.

Deposition of the functional materials through inkjet printing can be distinguished into three physical stages as shown in Fig. 1.1: (i) drop formation, (ii) drop impact and spreading, and (iii) evaporation of the carrier liquid leaving deposition of functional materials on a substrate. Detailed studies involving formation[1, 2], impact[2-5] and evaporation[6] of pico liter pure liquid drops in inkjet printing have been carried out. Drop evaporation and functional materials deposition in inkjet-printed pico liter colloidal drops has not been studied in detailed. Fundamental understanding of transport processes associated with inkjet printing colloidal drop forms the focal point of the present study.

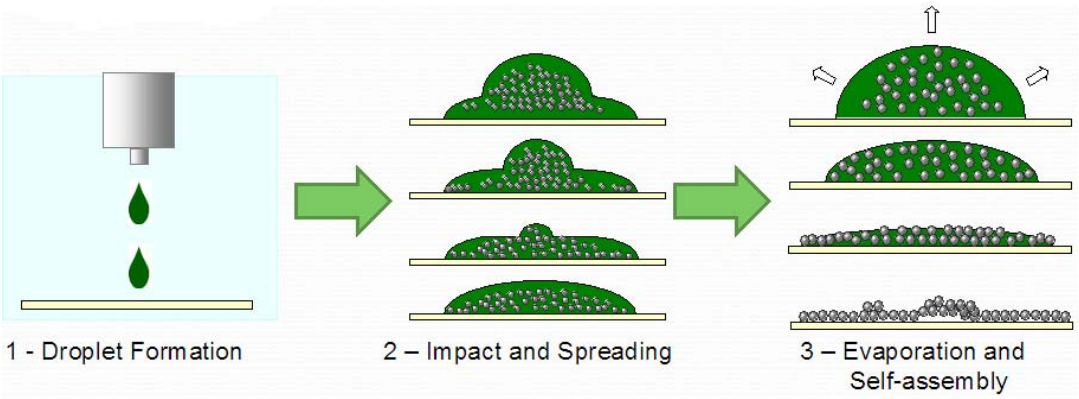

Figure 1.1. Physical stages of inkjet printing.

1.2. Physics of inkjet printing

Continuous and *drop-on-demand* (DOD) are two common mechanisms used to generate droplets in inkjet printers. Figure 1.2 shows the basic classification of the inkjet printing technology[7]. In continuous printing, drops are formed by a continuous jet of liquid. These drops are charged and then deflected by a high voltage deflection plate. Uncharged drops are however deflected into a gutter for recirculation. Depending upon the method of deflection, a continuous printing device can be designed with a binary or multiple deflection system. In a binary deflection continuous jetting system, the drops are either charged or uncharged, whereas in a multiple deflection continuous jetting system, the drops are charged and deflected to the media at different levels.

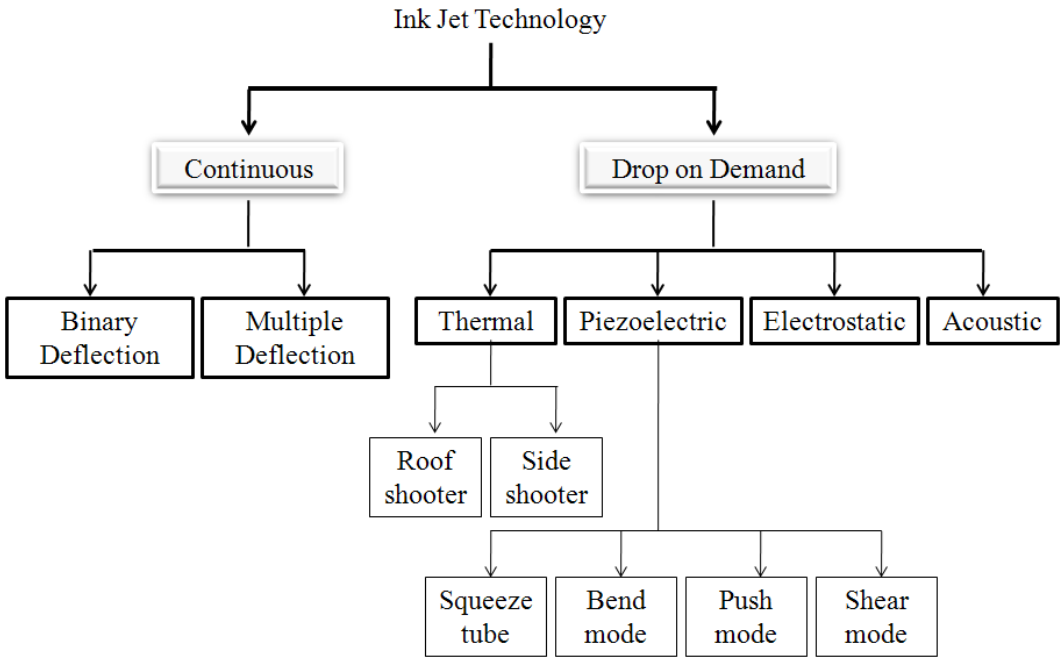

Figure 1.2. Categories of inkjet technologies[7].

In contrast to continuous inkjet printing where uncharged drops have to be intercepted and returned to the system by means of a pump and filters, in a drop-on-demand printer, a single drop is generated when needed thereby reducing waste of the ink[8]. Depending on the specific mechanism used in the drop formation process, the drop-on-demand technology can be categorized into thermal, piezoelectric, electrostatic, and acoustic systems. In a thermal inkjet system, a resistor is used to heat the ink inside the nozzle. The expanding bubble generated inside the nozzle pushes the ink to eject from the nozzle. Advantages of thermal inkjet printers are low equipment cost and wide knowledgebase in ink development. However, only low viscosity non-flammable inks can be used.

Piezoelectric inkjet printing can however use high viscosity and even inks made with flammable liquids. It also has very high reliability and can achieve high resolution as compared to other inkjet printing systems. Depending upon the way electrical current deforms the piezoelectric activator plate, the piezoelectric printheads can be classified into the following four categories: shear mode, bend mode, push-piston mode, and squeeze tube. In this study, a squeeze tube type piezoelectric print head is used and under the influence of an electric pulse, the piezo element squeezes the ink out of the nozzle to form drops.

Physical processes involved in inkjet deposition of functional materials include drop formation in a piezoelectric nozzle, impact and spreading of pico-liter drops onto a substrate, carrier liquid evaporation, and subsequent particle deposition. The following discussion describes some fundamental phenomena associated with each of these physical stages.

1.2.1. Drop formation in piezoelectric nozzle

Drop formation is ubiquitous in daily life. It is important in many technological applications including mixing, spray deposition, chemical processing, and inkjet printing. The viscosity, density, and surface tension of the printing fluid (i.e., the ink) influence the drop formation mechanism, stability of the ink jetting process and drop volume.

The stability of an ink is important during drop formation as the diameter of a nozzle orifice in an inkjet printer is often smaller than 100 μm. For suspension inks, the particle diameter should be less than 2% of the nozzle diameter to avoid nozzle clogging[9] and the particles should be fluidphilic. The suspension stability can also be improved by

matching the density between the carrier liquid and the particulate phase, and by decreasing the particle size.

In this thesis, a piezoelectric print head with a nozzle diameter of 60μm (MicroFab Technologies Ltd) is used to generate pico liter drops of suspensions. The amplitude and pulse width of the voltage waveform (both of which determine the volume of the ejected drop) are controlled by a waveform generator. A typical applied voltage waveform for the drop generation is demonstrated in Fig. 1.3. The increase in the applied voltage expands the glass chamber to suck the ink from the reservoir. After the ink is sucked in, it is allowed to settle by keeping the voltage constant. Then the voltage is decreased to shrink the volume of the glass chamber. This pushes the ink out of the chamber. The voltage is again kept constant to damp out the pressure waves in the chamber. Finally, the voltage is increased to expand the volume of the chamber. The increase in volume of the chamber prevents pinch-off of the liquid flowing from the nozzle. The amplitude of the voltage dictates the expansion and compression of the glass chamber and thereby controlling the drop volume. The rate of change in voltage controls the pressure in the chamber and the speed that pushes the ink out of the nozzle. It is an important parameter to avoid nozzle clogging.

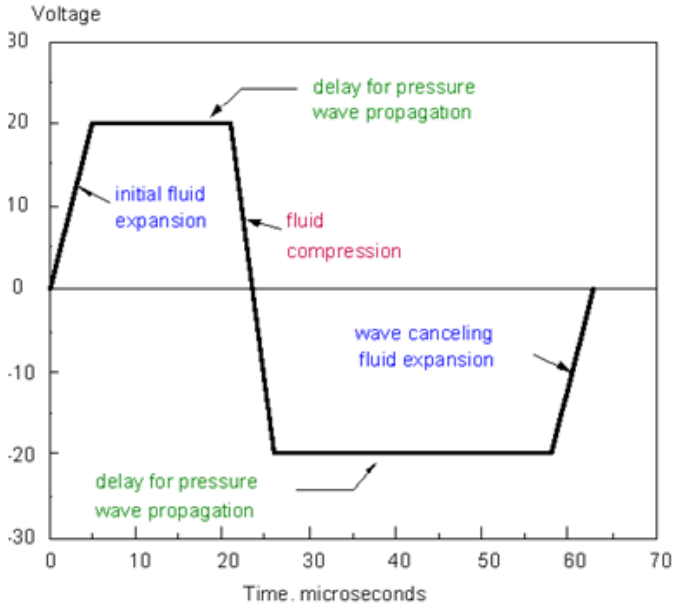

Figure 1.3. A typical voltage waveform applied to the piezoelectric element of the nozzle of an inkjet printer.

1.2.2. Impact and spreading of pico-liter drops

In drop impact and spreading, density, viscosity, and surface tension of the ink, and size and impacting velocity of the printed drop are important parameters. In addition, important dimensionless numbers governing drop impact and spreading dynamics are the Weber ($\mathrm{We} = \frac{\rho d v_d^2}{\sigma}$), Reynolds ($\mathrm{Re} = \frac{\rho d v_d}{\mu}$), and capillary ($\mathrm{Ca} = \frac{\mu v}{\sigma}$) numbers. The Weber number is defined as the ratio of inertia to surface tension. The increase in We number changes the drop impact on a substrate from deposition to splashing[10, 11]. The Reynolds number is defined as the ratio of inertia to viscosity. The increase in Re number increases drop spreading on a substrate. The capillary number is the ratio of viscosity to surface tension and it governs the drop spreading velocity. The kinetics of sessile drop spreading has been studied extensively where the relationship between advancing contact angle (depends upon surface wettability) and the capillary number can be shown in Fig.

1.4. It can be seen that as the apparent dynamic contact angle increases, the spreading velocity of the drop increases. Moreover, as the liquid wets the substrate, the driving force – the difference between apparent contact angle and equilibrium contact angle – decreases and so does the spreading velocity. As the viscosity of the ink increases, either due to the increase in solute concentration or filler particle volume fraction[12], spreading of the drop reduces. Solute composition also changes the spreading kinetics[13]. When a concentration gradient driven Marangoni flow is in the direction of droplet spreading, the rate of ink spreading is higher than that of individual components. However, when the Marangoni flow is in the opposite direction of spreading, the rate of ink spreading is lower than individual components.

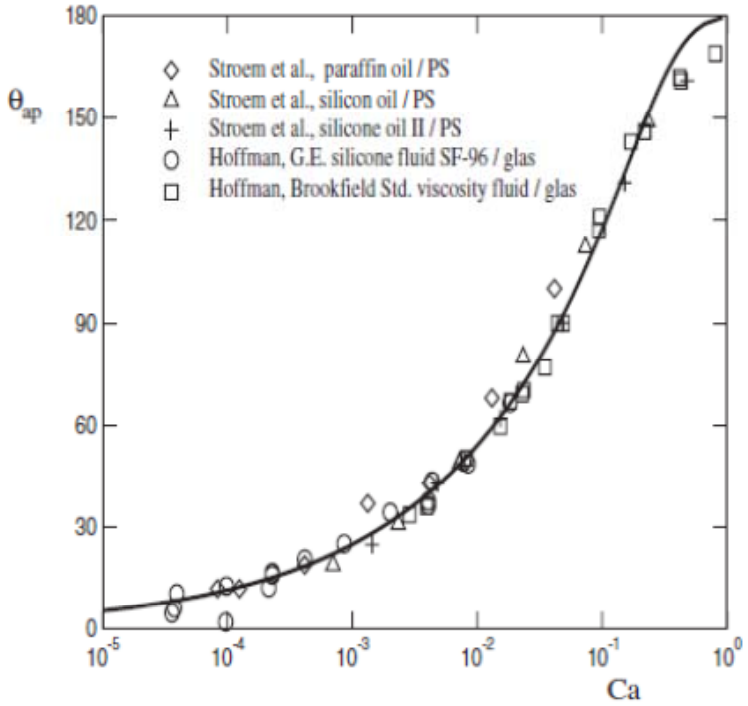

Figure 1.4. Apparent dynamic contact angles of perfectly wetting fluids measured in capillary number[14] and for a plunging plate[15]. Each symbol corresponds to a different fluid and/or substrate. The solid line is based on [16] $\mathrm{Ca}\ln\left(x/L\right)=\int_0^{\theta}\frac{x-\sin x\cos x}{2\sin x}dx$ with $x/L=10^{4}$ [17].

1.2.3. Carrier liquid evaporation

Evaporation of a pure liquid drop has been studied in detail[18-27]. During drop evaporation, the vapor pressure, thermal conductivity, and latent heat of evaporation of the ink drop, as well as the wettability and thermal conductivity of the substrate, affect the evaporation process. Different stages exist for evaporation of pure liquid drops according to the movement of the drop contact line and the decrease in the contact angle[19, 26]. When the contact line is pinned, the evaporation flux along the liquid-vapor interface is non-uniform as shown in Fig. 1.5 (a). This is in contrast with the case when the drop is receding with uniform evaporation rate along the liquid-vapor interface.

During drop evaporation, the latent heat is extracted from the substrate. As the drop apex is further away to the substrate than the drop edge, the drop apex is cooler than the edge as shown in Fig. 1.5 (b).

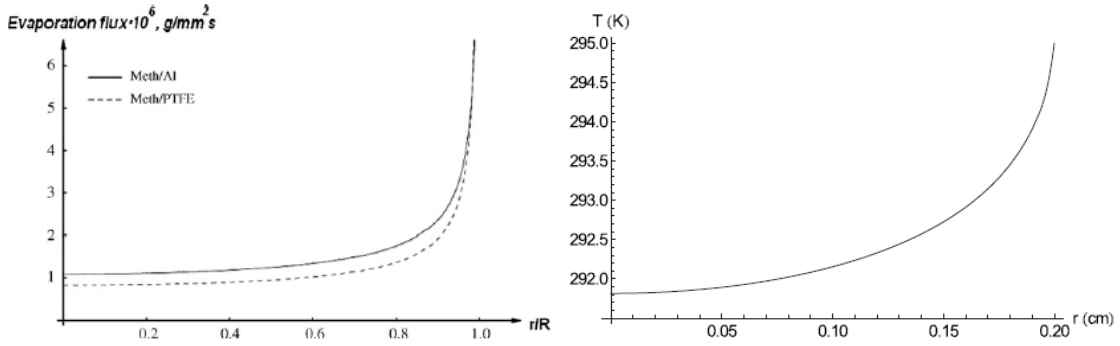

(a) (b)

Figure 1.5. Evaporation flux and temperature profiles along the liquid-vapor interface of a pinned drop. (a) Evaporation flux[23] and (b) temperature profiles[25].

The temperature difference along the liquid-vapor interface induces a temperature gradient driven Marangoni flow inside the drop. The direction of this temperature gradient driven Marangoni flow depends upon the ratio of the thermal conductivities of the substrate and liquid[28]. The evaporation process is assumed to be diffusion limited. The drop withdraws energy from the substrate and the evaporative flux is highest near the pinned contact line as compared to the drop apex. The schematic of an evaporating sessile drop is shown in Fig. 1.6 (a) with a non-uniform evaporative flux along the surface of the drop. As shown in the magnified section the pinned triple line, the interfacial energy balance for negligible heat conduction and convection in air is given as $-k_L \mathbf{n}\cdot\nabla T = \Delta H_v j(x)$ at $y = h(x)$, where ΔH_v is the specific latent heat of evaporation, $\mathbf{n}$

is the unit normal, and k_L is the thermal conductivity of the liquid. During evaporation, due to the variation of the evaporation rate $j(x)$ along the drop surface, the surface temperature varies. A gradient in surface tension is hence created along the drop surface and is balanced by the viscous stress. In the direction tangential to the interface, it follows $\tau = \mathbf{t}\cdot\nabla_s\gamma = \beta(\mathbf{t}\cdot\nabla_s T)$ at $y = h(x)$, where $\mathbf{t}$ is the tangential unit vector, ∇_s is the surface gradient, and $\beta \equiv \partial\gamma/\partial T$ is the material parameter that is negative for most liquid. At the drop-solid interface, the continuity of temperature $T_L = T_s$ applies and the heat flux follows $k_L\mathbf{n}\cdot\nabla T_L = k_S\mathbf{n}\cdot\nabla T_S$. For the Marangoni flow inside a drop, the circulation direction is controlled by the temperature gradient at $\theta = \theta_c$, which yields the following asymptotic solution $\left.\frac{\partial T_1}{\partial r}\right|_{\theta=\theta_c} = Cr^{\lambda-1}\left(\frac{1+k_R\tan(\lambda\pi)\tan(\lambda\theta_c)}{\tan(\lambda\theta_c)-k_R\tan(\lambda\pi)}\right)$ where $C \equiv \Delta H_v j_0 / k_L(2\cos\theta_c)^{\lambda-1}$ and $\lambda = 1/2 + \theta_c/\pi$. Here, the direction of the temperature gradient depends only on the sign of the numerator $1+k_R\tan(\lambda\pi)\tan(\lambda\theta_c)$. For large values of k_R, the numerator is negative and the temperature of the drop decreases from the edge to the center of the drop as shown in Fig. 1.6 (b). However, for values of k_R below the critical value $k_R^{crit} = \tan(\theta_c)\cot\left(\frac{\theta_c}{2}+\frac{\theta_c^2}{\pi}\right)$, the numerator is positive and the temperature of the drop increases from the edge to the center of the drop as shown in Fig. 1.6 (c).

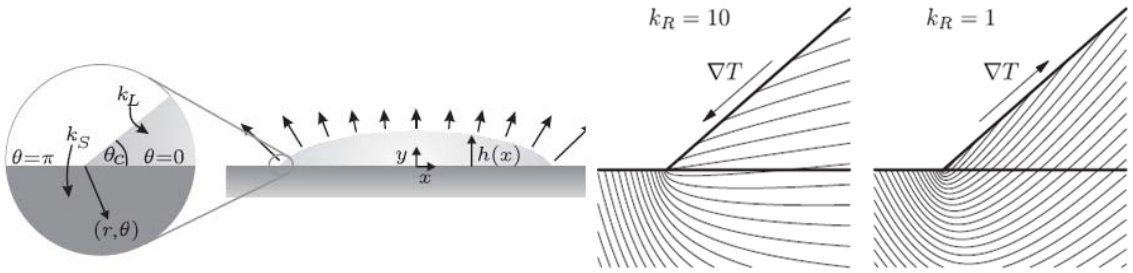

(a) (b) (c)

Figure 1.6. Variation in evaporative flux and temperature gradient in an evaporative drop. (a) Sketch of an evaporating liquid drop on a solid substrate, with a magnified three-phase contact line. (b-c) Asymptotic temperature distribution near the contact line of an evaporating drop with $\theta_c = \pi/8$. Arrows indicate direction of increasing temperature. (b) Isotherms for $k_R = 10$. The heat flux is approximately normal to the substrate. (c) Isotherms for $k_R = 1$. The heat flux has a large component tangential to the substrate.[28]

1.2.4. Particle deposition

Deposition of particles in a colloidal drop depends upon the density, wettability, diameter, and volume fraction of the particles, as well as the substrate wettability, viscosity and surface tension of the carrier liquid. The deposition morphologies in Fig. 1.7 demonstrate that at any contact angle, increasing the initial particle volume fraction resulted in the deposition of more particles at the center of the drop. Moreover, at any fixed initial particle volume fraction, lowering contact angle resulted in deposition of particles in the vicinity of the contact line. In the initial stage of evaporation, particle volume fraction does not affect the evaporation, however with the contact line pinning, there is less remaining liquid to push the particles to the contact line and to rearrange the particles at the late stage of evaporation. For the case of higher particle volume fractions of colloid the lack of carrier liquid at the later stage of evaporation results in a spherical cap shape deposition. The constant contact angle mode of evaporation that often exists on

hydrophobic surfaces results in continuous depinning of the contact line during evaporation. Due to depinning, particle deposition remains concentrated in the center of the drop, resulting in a flat deposition as compared to a ring type deposition on hydrophilic surfaces.

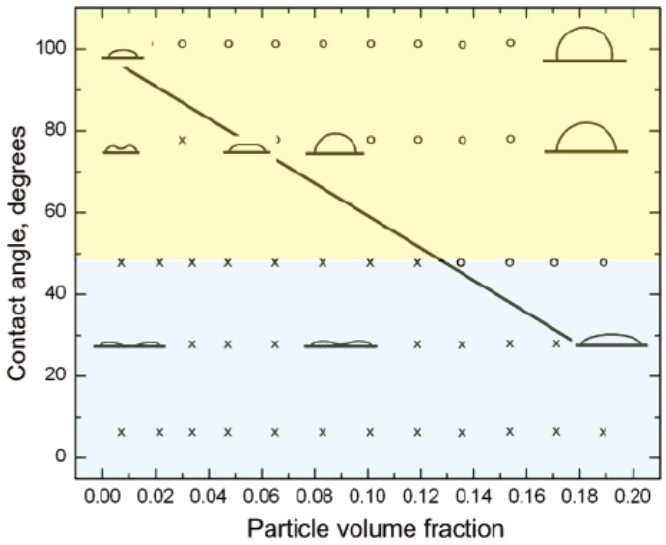

Figure 1.7. Categorized particle deposition shape as a function of particle volume fraction and contact angle of the liquid with the substrate[29]. The open circles are experimental data points corresponding to convex shape, and the crosses show concave shape[30].

1.3. Literature review

Previous sections summarize the importance of the present research and illustrate the wide range of physical phenomena in inkjet printing. The succeeding section provides a brief overview of the literature concerning drop formation, impact and spreading, evaporation, and particle deposition, as well as the applications of inkjet printing into patterns and functional devices.

1.3.1. Drop formation

Formation of drops of a pure liquid has been studied for over 250 years. Eggers[31] conducted an extensive review about breakup of a liquid jet into drops and drop formation from a dripping faucet. Drop formation in drop-on-demand piezoelectric devices was examined by Dong et al.[1, 2] A synchronized flash photography setup was used to obtain sufficient brightness with a temporal resolution of 1 μs and a spatial resolution of 0.81 μm. Drops containing different liquids were studied. Glycerin was added in water to create glycerin-water (GW) in 48:52 w/w with an increased viscosity of 5cP while keeping the surface tension of 68 mN/m and density of 1.1 g/cm^3. In addition, isopropanol was added into the GW mixture to create glycerin-water-isopropanol (GWI) in 34:53:13 w/w with a decreased surface tension of 35 mN/m while keeping viscosity of 5 cP and density of 1.04 g/cm^3. The effects of the applied voltage on the piezo element were examined. The criteria for selecting the surface tension and viscosity of the liquid were developed to avoid the satellite drop formation and to improve the resolution of the inkjet printing method. An increase in travelling velocity of the ejected liquid was observed for the driving voltage varying from 21.6 V to 25.6 V. This holds true for liquids of different viscosities and surface tensions as it can be seen from Figs. 1.8 (a) and (b) for all three liquid solutions (water, GW and GWI). An increase in viscosity from 1 cP to 5 cP changes the liquid thread profile from nearly flat to parabolic at the early stage of the ejection. At the early stage of ejection, surface tension does not play a significant role in determining the shape of the ejected liquid. However, during the stretching process, a low surface tension liquid necks slowly and forms a smaller bulbous head resulting in a long tail.

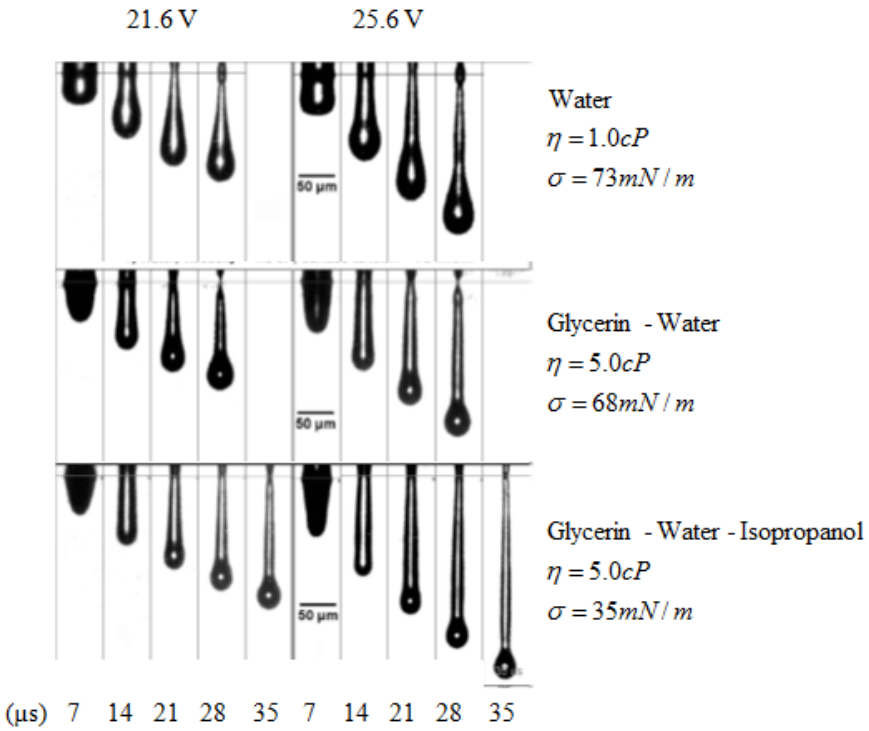

Figure 1.8. Sequential images of ejection and stretching of three liquids (top to bottom: water, glycerin-water and glycerin-water-isopropanol)[1].

Jang et al.[32] investigated the relationship between inkjet printability and fluid properties by monitoring the drop formation. It was concluded that the printable range is $0.07 \le \mathrm{Oh} \le 0.25$, where $\mathrm{Oh} = \dfrac{\eta}{(d_n \rho \sigma)^{1/2}}$ is the Ohnesorge number which relates to the viscosity (η), diameter of the nozzle (d_n), surface tension (σ), and density of the fluid (ρ).

Furbank and Morris[33] carried out experiments to study the effect of particles on drop formation in colloidal suspensions. They found that, for a particle volume fraction below 10%, the effect of particles on drop formation is not significant. However, for higher particle volume fractions, the particles form thick cone-like structures both near the orifice and at the trailing edge of the forming drop stabilizing the drop formation.

1.3.2. Drop impact and spreading

The impact and spreading of the liquid drop on the solid surfaces have been studied in detail and reviewed by Yarin[10] and Bonn et al.[17]. Rioboo et al.[34] studied impact and spreading of water drops on glass, wax and PVC substrates of different surface roughness. The authors observed four distinct phases of spreading as shown in Fig. 1.9. These stages are kinematic, spreading, relaxation and wetting/equilibrium phases. At the beginning of the spreading (the kinematic phase), the diameter of the drop increases with $t^{0.5}$ and then during the spreading phase, the substrate wettability, as well as the surface tension and viscosity of the liquid play important roles. During the kinematic phase, liquid inside the drop is compressed and a shock wave is formed and detaches after reaching a critical angle. After this first phase, a radially expanding film of liquid spreads on the substrate under the effect of impact inertia. With time increases, a lamella is ejected from the base of the drop and forms a thin film bounded rim. The spreading phase is then followed by a relaxation phase, and depending on the wettability of the substrate, the drop can either spread or recede. The last phase is the wetting/equilibrium phase, during which the drop will attain its final shape following Young's equation $\theta = \cos^{-1}\left(\frac{\sigma_{sv} - \sigma_{sl}}{\sigma}\right)$, where θ is the contact angle of the liquid with the solid surface, σ is the surface tension between the liquid and vapor phases, σ_{sv} is the surface tension between the solid and vapor phases and σ_{sl} is the surface tension between the solid and liquid phases.

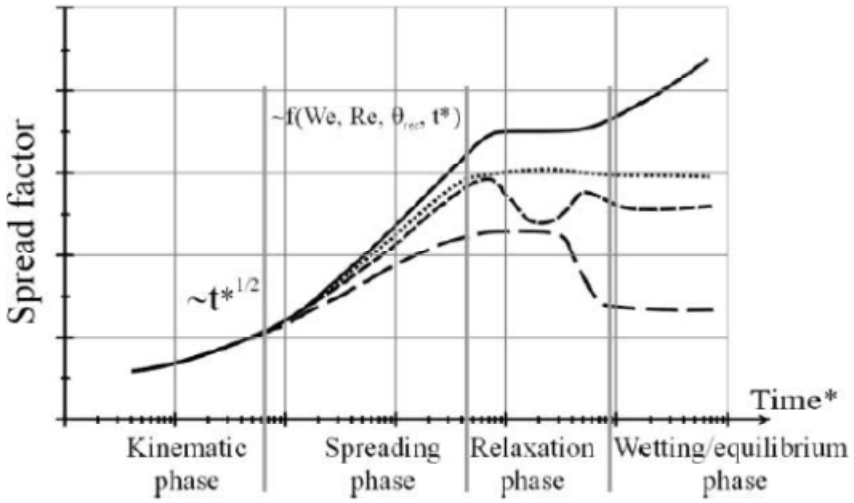

Figure 1.9. Schematic representation of the drop spreading with time on a solid substrate. The different lines correspond to an arbitrary choice of possible spreading histories, depending on the drop impact velocity, liquid surface tension, viscosity, and density and substrate wettability[35].

High-speed repeatable phenomena can be studied by using a low frame rate camera by flash photography. In flash photography, a repeatable phenomena is observed in cycle with a fixed temporal delay. The sequence of images can then be used to study the phenomena as the evolution of a single event. As an example, a repeatable drop formation at 1 Hz can be observed by using 10 frames per second camera, where the drop formation can be observed with a temporal resolution of 10 μs. Dong et al.[2] observed spreading of pure liquid drops on surfaces with different wettabilities. Flash photography was used in their study and the drop observations were quantified by scaling the height and diameter of drops and plotting the evolution of height and diameter as a function of time as shown in Fig. 1.10. It can be seen that during the first 10 μs, the drop spreads on the substrate irrespective of the substrate wettability during the kinematic stage. After the kinematic phase is over, the substrate wettability comes in play and the drop spreads (Fig.

1.10 (a)) or recedes (Fig. 1.10 (b)) as the drop reaches the equilibrium stage. After the drop reaches the equilibrium further changes in height and spreading diameter subsides.

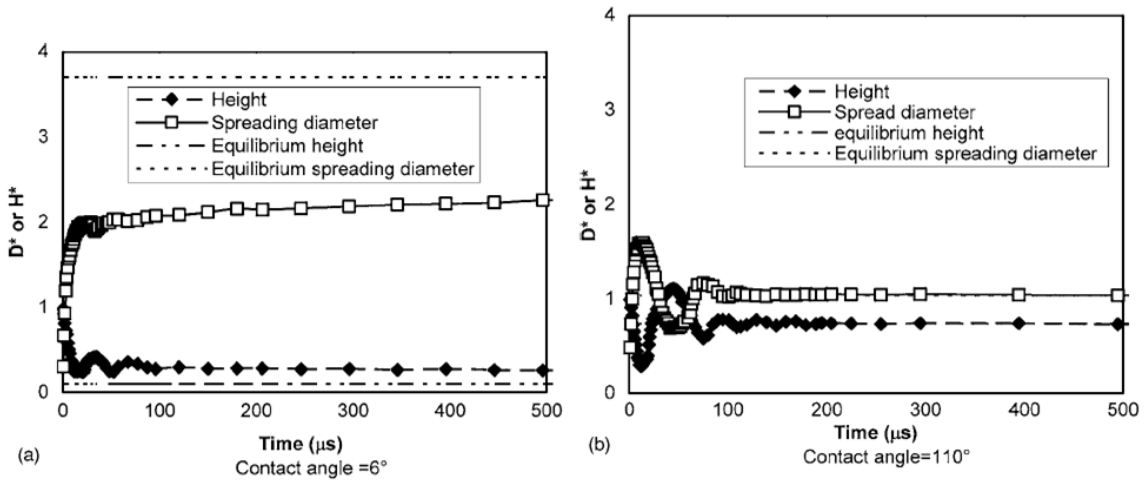

(a) (b)

Figure 1.10. Dimensionless spreading diameter, D^*, and thickness, H^*, for drops impacting on two surfaces with contact angle of (a) 6° and (b) 110°[2].

Similar studies have also been carried out by Dam and Clerc[4], Dong et al.[3] and Lim et al.[5]. It was found[3-5] that inkjet printed drops that are on the order of microns in diameter behave similarly compared with drops on the order of millimeters in diameter during the impact and spreading stage.

Nicolas[12] studied the effect of particle volume fraction on spreading of colloidal drops. It was found that, the increase in particle volume fraction increases the suspension viscosity and in turn decreases the, drop spreading kinetics. However, the size of particles does not have significant influence in drop spreading kinetics.

1.3.3. Evaporation of pure liquid drop

Kim et al.[19] explained the evaporation mechanism of water drops on polymer surfaces. Three distinct stages were observed during drop evaporation as shown in Fig 1.11. In the first stage, the contact area is fixed and the contact angle decreases from an equilibrium contact angle to static receding contact angle as the contact line is pinned. In the second stage, the contact angle remains constant but the contact area decreases. Moreover, in the third and the final stage, both contact area and contact angle decrease as the drop disappears completely.

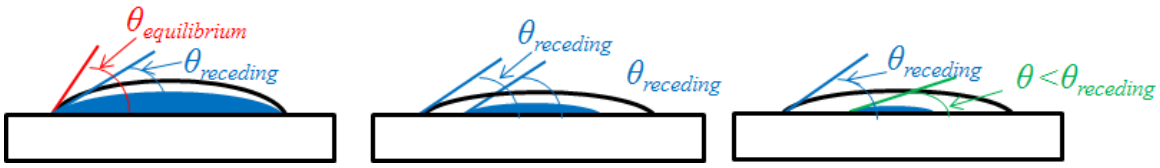

Figure 1.11. Schematic of evaporating liquid drop on a solid surface, from left to right we can observe the constant contact area, constant contact angle and mixed stages of evaporation.

Bourges-Monnier and Shanahan[26] observed evaporation of distilled water and n-decane on epoxy and glass substrates. As shown in Fig. 1.12, during the first stage of evaporation (i.e., the constant contact area stage), the height and contact angle of the drop decrease (Stages I and III). When the contact angle reaches the receding contact angle, the constant contact angle stage begins with the decrease in diameter and height of the drop as represented by Stage III in Fig. 1.12. During the last stage of the evaporation height, diameter and contact angle all decrease.

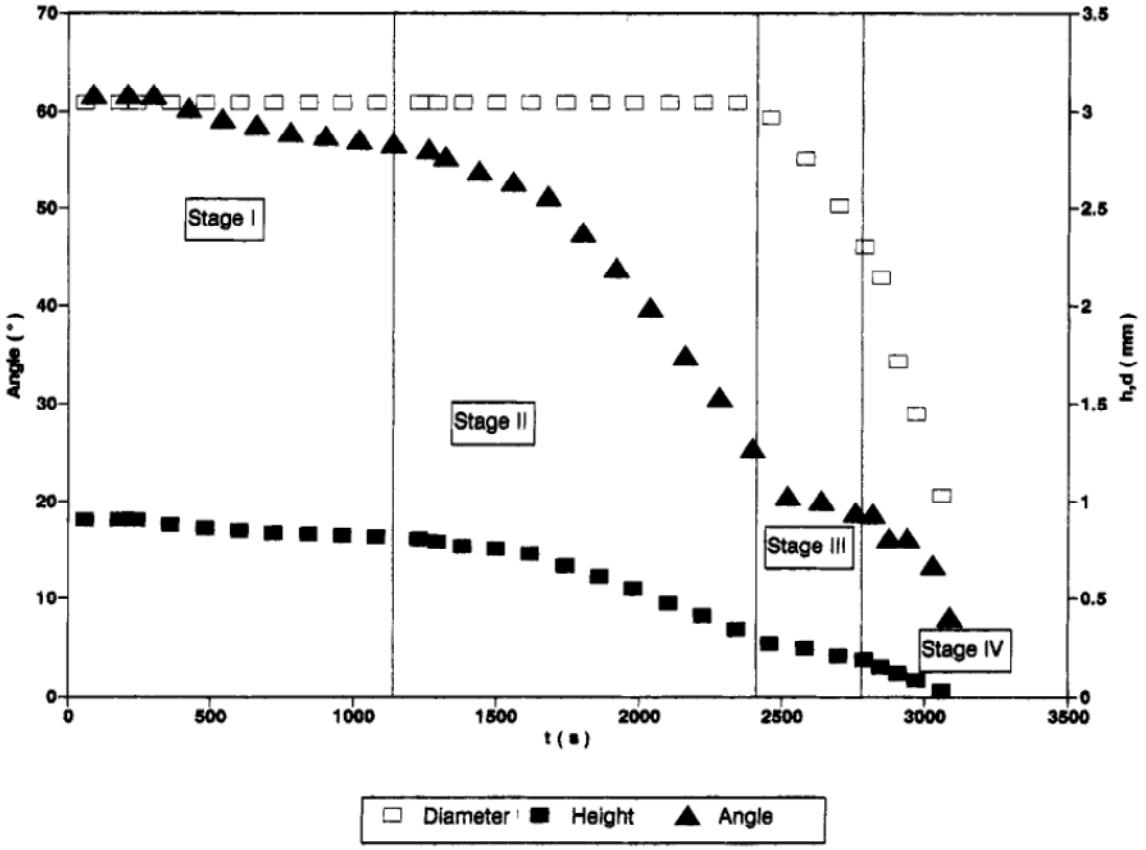

Figure 1.12. Evolution of contact angle (θ), height (h) and diameter (d) of an evaporating water drop of 4 μL on polished epoxy resin substrate[26].

Birdi et al.[18] measured the weight of evaporating drops as a function of time. It was found that the drop volume decreases linearly with time as shown in Fig. 1.13 (a). The initial shape of the drop is assumed to be a spherical cap. The drop remains pinned during the evaporation. From Fig. 1.13 (b), it was concluded that the evaporation rate is linearly proportional to the radius of the drop instead of the area of the drop. The rate of the evaporation was dependent on the diffusion rate of water vapor in surrounding air.

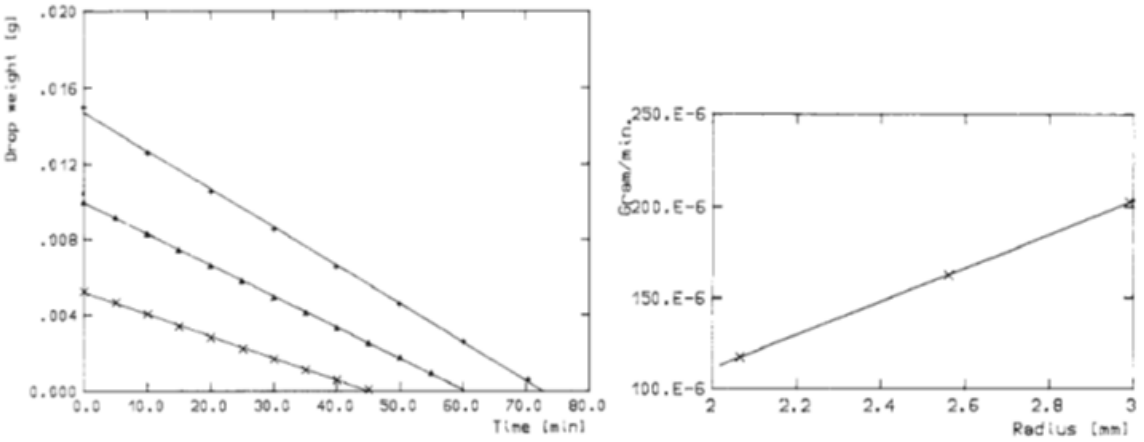

Figure 1.13. Drop weight as a function of time and evaporation rate as a function of drop radius. (a) Weight of evaporating drops as a function of time. Initial drop mass shown in figure are 15, 10 and 5 mg. (b) Evaporation rate as a function of drop radius[18].

Starov and Sefiane[24] change the temperature of the substrate from 25 to 40 °C to observe the corresponding change in the drop evaporation behavior. The theoretical prediction for the evaporation flux as a function of drop radius is shown in Fig. 1.14. For a pinned drop, the evaporation rate peaks near the pinned contact line, similar to the observation of Deegan[36, 37].

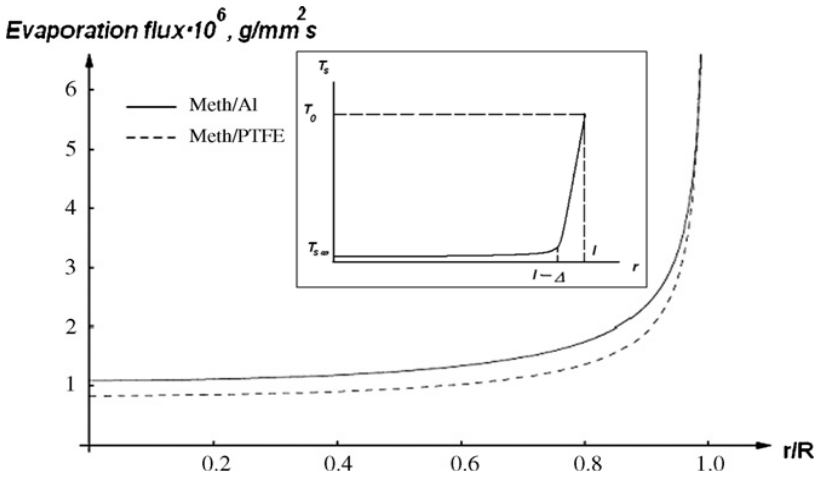

Figure 1.14. Local evaporation flux as a function of location on drop radius[23] for the drop methanol on Al/PTFE substrate. In the box, temperature of the drop at the surface of the drop as a function of location on drop radius[24].

Temperature of the drop also varies along the surface of the drop during evaporation. An evaporating drop extracts latent heat of evaporation from the substrate. Thermal conductivity of the liquid drop is usually lower than the substrate, thus the liquid near the contact line gets latent heat of evaporation from the substrate, whereas liquid near the center of the drop loses temperature during evaporation. This result in a higher temperature at the edge of the drop compared to the center of the drop as shown in the inset of Fig. 1.14. Girard et al.[22] observed evaporation of water drop on a heated substrate of 40 °C. It was observed that the temperature of the drop center decreases during evaporation as shown in Fig. 1.15.

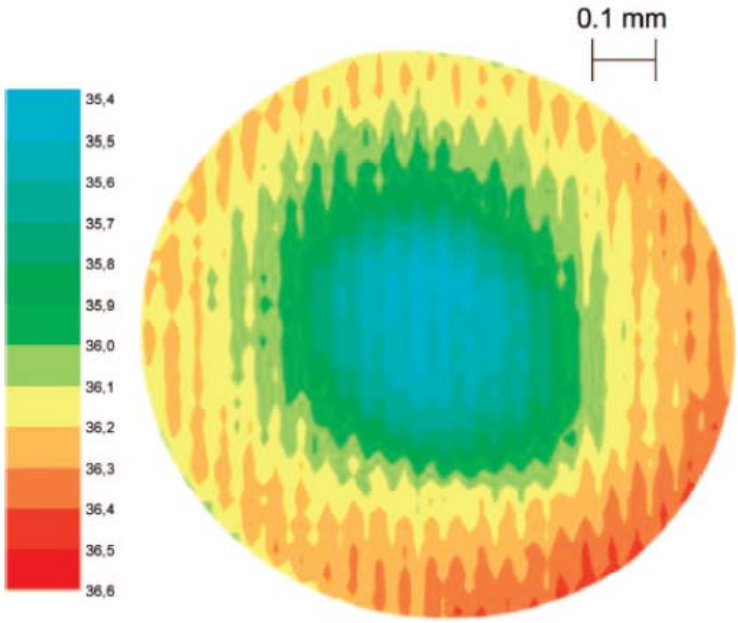

Figure 1.15. Infrared image of an evaporating sessile drop on aluminum substrate at 40 °C. The color coding on the left indicates the values of the actual temperatures in °C[22].

1.3.4. Evaporation and particle deposition of colloidal drop

The addition of particles in a pure liquid drop extends the constant contact area stage of drop evaporation due to the accumulation of particles at the contact line region that further enhances pinning[38*]. This extended constant contact area stage results in a coffee ring deposition from a colloidal drop for the case of a volatile drop evaporating on a hydrophilic substrate surface[37].

---

* Chhasatia, V. H.; Sun, Y., Interaction of bi-dispersed particles with contact line in an evaporating colloidal drop. *Soft Matter* 2011**,** 7, 10135-10143.

1.3.4.1. Spherical particles

Deegan et al.[36, 37] explored evaporation of a dilute colloid drop and found that during the constant contact area stage of evaporation, evaporation rate along the liquid-vapor interface is not uniform. It was found that, for diffusion limited evaporation, vapor concentration near the drop attains steady state quickly (diffusion time scale $t_d = \frac{4R^2}{D}$, where R is the drop radius and D is diffusion coefficient of water vapor in air). Therefore, the diffusion equation can be reduced to a Laplace's equation ($\nabla^2 u = D\partial_t u \approx 0$ where u is the mass of vapor per unit volume of air. For time longer than t_d, the boundary conditions are that (1) along the surface of the drop the air is saturated with vapor so that u is a constant, (2) the evaporative flux is normal to the substrate (i.e, $J \cdot \mathbf{n} = D\partial_{\mathbf{n}} u$ is zero as the vapor cannot penetrate the substrate), and (3) u converges to the ambient vapor concentration, u_∞, far from the drop. Solving the Laplace equation for the aforementioned boundary conditions, the evaporation rate is obtained as $J_s(r,t) \sim (R-r)^{-\lambda}$, where $\lambda = \frac{\pi - 2\theta_c}{2\pi - 2\theta_c}$ and θ_c is the contact angle of the evaporating drop. The evaporation rate is higher near the pinned contact line as shown in Fig. 1.16.

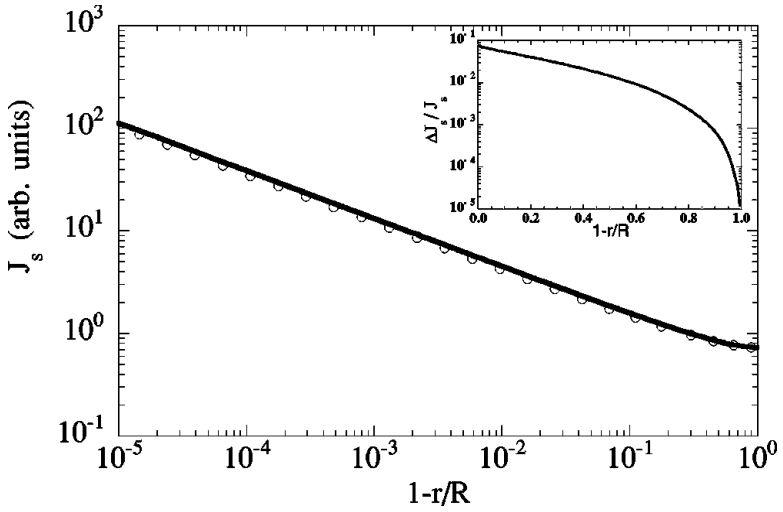

Figure 1.16. The value of J_s calculated with the full analytic form compared to the approximated form. The two curves are approximately equal. As is shown in the inset, the upper bound on the difference is 10%.

The evaporative flow drags particles toward the edge of the drop and creates a "coffee ring" effect where a large number of particles are deposited at the edge of the drop compared to the center. The deposition morphologies from three identical drops dried under different conditions were studied as shown in Fig. 1.17.[36] Fig. 1.17 (a) shows a drop that was allowed to evaporate normally. The second (Fig. 1.17 (b)) was mounted on a pedestal and surrounded by a bath of water such that the level of the bath coincided with the base of the drop so that the evaporation rate is spatially uniform. The third drop (Fig. 1.17 (c)) was surrounded by a chamber with a small hole above the center of the drop so that evaporation primarily occurred at the center. The results show that the first drop has a singular profile, the second drop has a uniform profile, and the third has a profile that is largest at the center and goes to zero at the edge. When the change of the interface height is different from the evaporation profile, a ring is produced as in the first and second drop. However, if profiles are similar then a uniform deposit is formed[36].

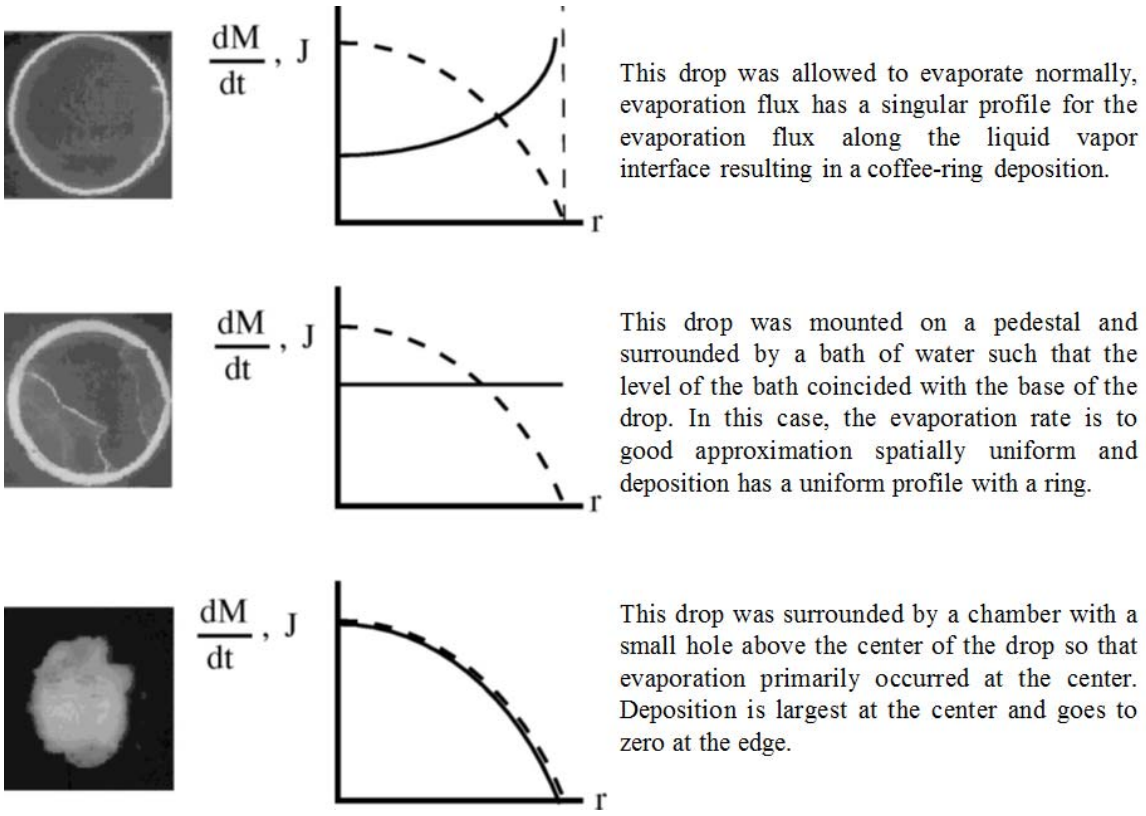

Figure 1.17. Photographs of the resulting deposit left by three identical drops dried under different conditions[36]. The radius of the initial drop was approximately 4 mm. The evaporation rate is plotted schematically in the right column. The second curve (dashed line) in the right column represents the change of the interface height.

Kaneda et al.[6] printed polystyrene/xylene drops on lyophobic glass substrate and found that the local film thickness near the periphery is governed by pinning time at the contact line, and higher evaporation rate results in ring-like deposition compared to dot-like deposition at low evaporation rate.

Hu and Larson[39] explored the role of Marangoni flow in evaporation of octane based inks. The authors found that Marangoni flow counters the evaporative flow and restricts the contact line pinning enhancement and suppresses the coffee ring effect. The

presence of Marangoni flow in the octane based ink suppresses coffee ring effect and the absence of Marangoni flow facilitates the coffee ring effect on fluidphilic substrates.

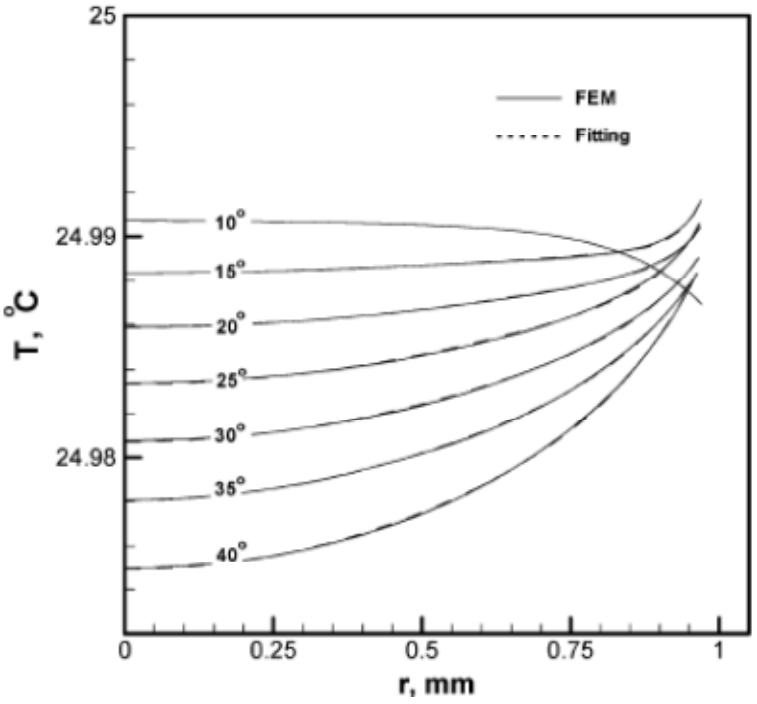

Figure 1.18. The temperature profiles along the droplet surface at contact angles of 40°, 35°, 30°, 25°, 20°, 15°, and 10°. The solid lines are the finite element results, and the dashed lines are the fitting results using $T/\Delta T_0 = a\tilde{r}^{\,b} + (1-a)\tilde{r}^{\,2} + c$.

Elimination or enhancement of this coffee ring deposition can be accomplished by a surface tension driven Marangoni flow. Surface tension gradient in an evaporating drop can be induced by either a concentration or temperature gradient. Coffee ring effect can be suppressed by adding a low vapor pressure, low surface tension liquid to the original drop. The high vapor pressure, high surface tension liquid evaporating faster at the edge of the drop reduces the surface tension at the edge. This surface tension gradient establishes a Marangoni flow in the direction opposite to the evaporatively-driven flow, preventing particles from segregating at the contact line during the constant contact area

mode of evaporation[40]. Direction of the Marangoni flow depends upon the surface tension gradient, which can be reversed by adding a low vapor pressure, high surface tension liquid in the colloidal mixture. Lim et al.[41] took advantage of this concentration induced surface tension driven Marangoni flow to deposit 6,13-bis(triisopropylsilylethynyl) pentacene in a mixture of chlorobenzene and hexane/dodecane/o-dichlorobenzene. The authors observed Marangoni flow aiding and suppressing the coffee ring effect by addition of dodecane and o-dichlorobenzene in chlorobenzene respectively. Surface tension of the liquid varies inversely with temperature. The substrate provides energy for evaporation of the drop, and as the center of the drop is away from the substrate it is usually at a lower temperature compared to the edge. This temperature difference can produce a surface tension gradient in the drop. Direction of the temperature gradient induced Marangoni flow can be reversed by selecting liquids and substrates such that the ratio of thermal conductivities of solid substrate to liquid less than 1.4[28].

1.3.4.2. Ellipsoid particles

Loudet et al.[42] observed open branched aggregations of ellipsoid particles on the water-oil interface. The ellipsoid particles trapped at the liquid-liquid interface interact through strong, long range capillary attractions compared to spherical particles[43]. This strong interactions among the ellipsoid particles can actually suppress the coffee-ring effect as shown by Yunker et al.[44] in Fig. 1.19 (a).

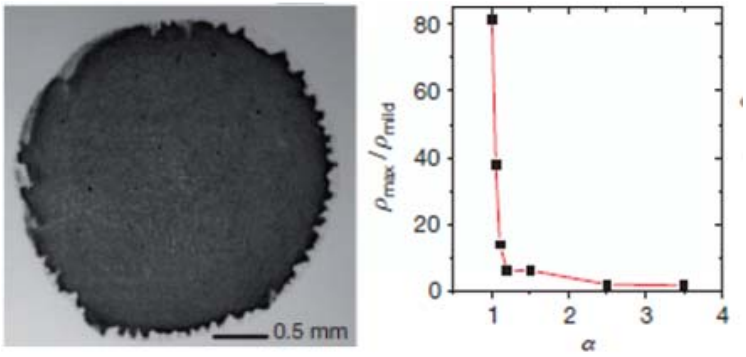

(a) (b)

Figure 1.19. Deposition of ellipsoid particles. (a) Dried deposit of ellipsoid particles and (b) deposition density as the aspect ratio of the ellipsoid particles (aspect ratio = major axis/minor axis)[44].

Yunker et al.[44] dispersed the ellipsoid particles in DI water and water mixed with surfactants and observed their deposition behavior. The authors found that capillary attraction is the major factor in the suppression of the coffee-ring, as the ellipsoids dispersed in surfactant mixed water exhibits coffee-ring but ellipsoids dispersed in DI water have uniform deposition. The surface tension of the surfactant mixed water is lower than that of the water reducing the attraction of the ellipsoid particles.

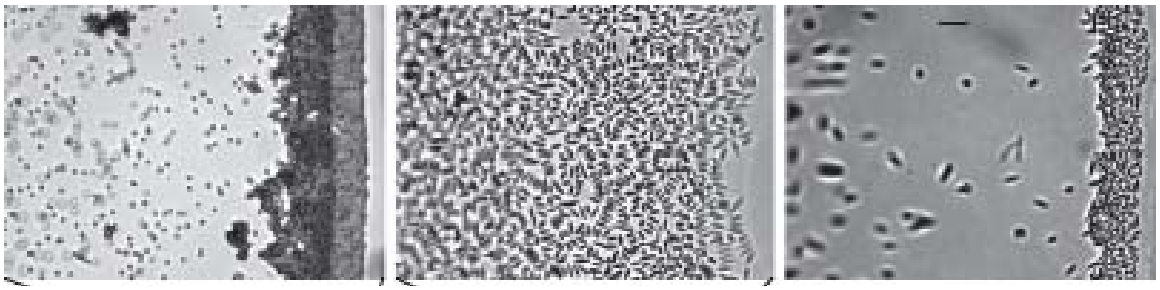

(a) (b) (c)

Figure 1.20. Magnified image of the contact line region of evaporating drop. (a) Spherical particles in water, (b) Ellipsoid particles in water and (c) Ellipsoid particles in water mixed with surfactant[44].

Yunker et al.[44] also mixed the ellipsoid particles with spheres and found that when the minor axis of the ellipsoid is larger than the diameter of spherical particle the spherical particles can move under or pass through open branched aggregations of ellipsoid particles and exhibit coffee-ring. However, if the diameter of the spherical particles is larger than the minor axis of the ellipsoid particles than these spherical particles cannot reach to the edge of the drop and suppressing the coffee-ring deposition.

1.3.5. Line and film printing

Duineveld[45] studied the stability of inkjet-printed lines of poly(3,4-ethylenedioxythiophene) poly(styrenesulfonate) (PEDOT:PSS) on homogeneous substrates. Conducting polymer, PEDOT:PSS, was dispersed in water with a surface tension of 0.07 Nm^{-1} and viscosity of 20 cP at room temperature. Spherical droplets of 67.4 ± 1.0 μm in diameter were generated by a single-nozzle piezoelectric drop-on-demand ink-jet system with a 50 μm nozzle diameter and a 2 m/s travelling velocity. The substrate movement was controlled by a x-y stage with a variable speed (V_s). Glass substrates were modified by UV-O_3 oven or CF_4 plasma to obtain different wetting properties, as summarized in Table 1.1. The effect of advancing contact angle on line stability was examined. The stage speed and the jetting frequency were varied to change the distance between successive drops (Δx). Images of the evaporated lines were taken by a CCD camera.

Table 1.1 Contact angle of PEDOT-PSS on different substrates.

Case	Substrate	Advancing contact angle (θ_a)	Receding contact angle (θ_r)
1	UV-O_3 (treated)	24°	0°
2	Glass substrate(non-treated)	65°	0°
3	CF_4 (treated)	97°	32°

The results show that overlapping drops printed on substrates with finite receding contact angles (e.g., θ_r = 32° for the CF_4 treated glass substrate) do not merge to form a stable line, but break into individual drops due to contact line dewetting. Each broken drop-shaped deposit contains multiple printed drops as shown in Fig. 1.21 (a). Liquid rivulet on a solid substrate with a finite receding contact angle is unconditionally unstable[46], where the wavelength (λ) of the occurring drops was predicted by $\lambda \approx \frac{1}{0.15}\sqrt{\frac{2V_s}{\pi \Delta x}}$ as shown in Fig. 1.21 (d)[47].

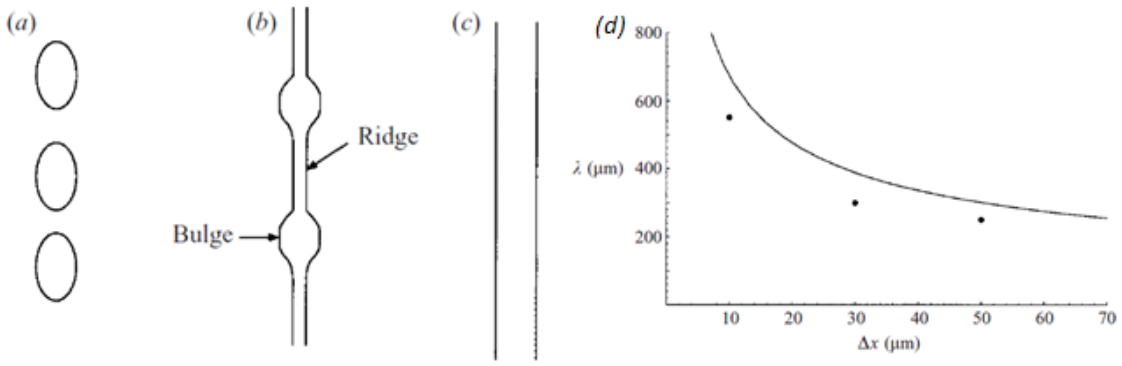

Figure 1.21. Different modes of a printed line on a substrate; (a) the line breaks up into individual droplets; (b) the line forms liquid bulges connected by a ridge of liquid; (c) stable printed line; and (d) Wavelength (λ) of the instability for finite receding contact angle as a function of Δx. Experimental results[45] (•) are compared with theoretical results[47].

For untreated glass substrates with a zero receding contact angle, the instability of the line can be observed in Figure 1.21 (b). As the liquid does not dewet the substrate, the width of the ridge can never become smaller than the diameter of a single drop. All perturbations in the line can only increase the line width as the liquid does not recede; therefore bulges in lines occur when the contact angle in the liquid ridge is larger than the advancing contact angle due to disturbance as shown in Figure 1.22 (a).

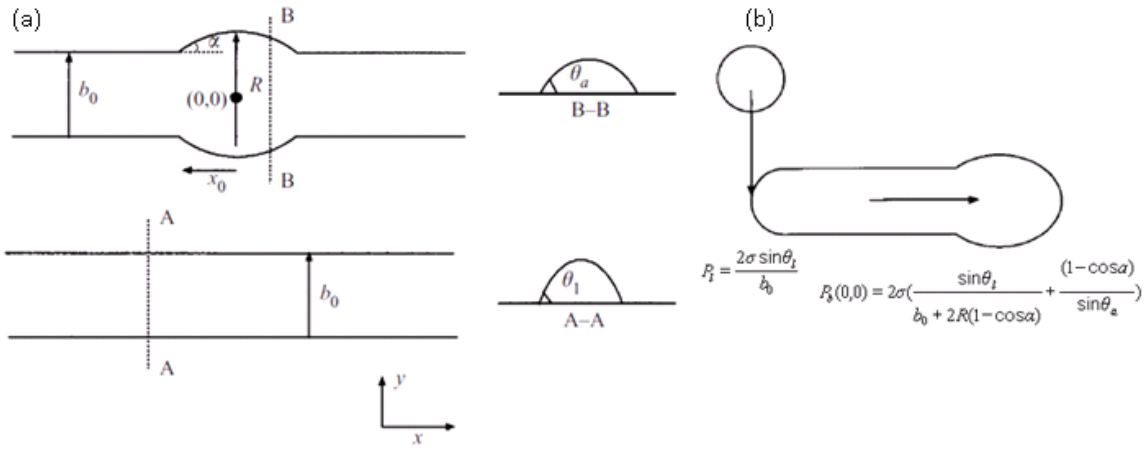

Figure 1.22. Flow of ink toward the bulge in line. (a) Top view of a stable line with a constant cross-section with contact angle θ_l, and a line with a bulge. The contact angle of the liquid in the disturbance is equal to θ_a. (b) Schematic of the start of the growth of a liquid bulge at the rear of a printed line. The pressure at the front of the line, P_f, is larger than in the bulge P_b, because of the larger curvature.

The author assumed that the flow through the liquid ridge to the fully developed bulge. Flow of the liquid Q is calculated by[48]

$$Q = \frac{s\Delta PS^2}{\mu l_r} \tag{1.1}$$

where s is the shape factor ($s = \frac{32S}{c_f p^2 \,\mathrm{Re}}$)[49], l_r is the length of the connecting liquid ridge, S is the area of the cross-section and μ is the liquid viscosity. For the no-slip boundary condition, Eq. (1.1) is valid. Then by using the zero shear stress condition on the free surface, the flow rate can be calculated by the 1-D Navier-Stokes equation given by by[48]

$$\frac{d^2u}{dz^2} = \frac{-1}{\mu}\frac{dP}{dx} \tag{1.2}$$

where u is the axial velocity of liquid in the ridge. For the no-slip boundary condition (z = 0, u = 0 and $z = h$, u = 0) and free surface boundary (z = 0, u = 0 and $z = h$, du/dz = 0) conditions, the flow rate Q can be calculated by

$$Q = \frac{4s\Delta P S^2}{\mu l_r} \tag{1.3}$$

where the shape factor s can be simplified by using $c_f \,\mathrm{Re} \approx 64$ and then calculated by $s = \frac{\theta_2 - \sin\theta_2 \cos\theta_2}{8(\sin\theta_2 + \theta_2)^2}$. At a lower θ_2, the value of s decreases thereby reducing the flow rate Q toward the bulge. The author also estimated contour of the bulge *b(x)* as $b(x) = b_0 + 2\left(\sqrt{R^2 - x^2} - R\cos\alpha\right),\ -x_0 \le x \le x_0$ where, $x_0 = R\sin\alpha$. At the maximum bulge width b_0, the relation between α and R can be given by $\alpha = \arccos\left[\frac{R + b_0}{2R}\right]$. The pressure in a liquid line (P_l) is calculated by $P_l = \frac{2\sigma\sin\theta_1}{b_0}$ and the pressure in the bulge (P_b) is smallest at the position (x,y) = (0,0), which can be calculated by

$$P_b(0,0) = 2\sigma\left(\frac{\sin\theta_a}{b_0 + 2R(1-\cos\alpha)} + \frac{(1-\cos\theta_a)}{R\sin\theta_a}\right) \tag{1.4}$$

and pressure at the front (P_f) is calculated by $P_f = \frac{2\sigma \sin\theta_a}{b_0} + \frac{2\sigma \sin\theta_2}{b_0}$, where the first term in P_f is the contribution of the individually printed drop and the second term is the pressure in the ridge.

The pressure difference between the bulge and the front of the line, ΔP can be calculated by $\Delta P = P_f - P_b$, that drives the flow into the bulge creating a higher contact angle in the bulge than the advancing contact angle, thereby spreading the bulge. As the wettability of the substrate increases for the case of UV-O_3 treated substrate, a lower θ_2 decreases the shape factor and reducing the flow rate Q toward the bulge. This increased wettability makes pumping of the liquid from the front of the line to the bulge more difficult, increasing the stability of the line.

Duineveld[45] and Subramanian and Soltman[50] used inkjet printing to print conducting polymer (PEDOT:PSS) on coated glass substrates and found parameters to print smooth conducting lines. Duineveld[45] studied the stability of ink-jet printed lines of liquid with pinned contact line on homogeneous substrates. A simple dynamic model was proposed to estimate the occurrence of liquid bulges at various wavelengths. Local contact angle of the liquid higher than the static advancing contact angle is a necessary, but not sufficient condition for bulging. Subramanian and Soltman[50] built upon the study of Duineveld[45] and proposed that spatial spacing and time delay between successive drops are important parameters to print continuous lines. The authors suggested that by decreasing distance between successive drops line behavior can be changed from individual drops to scalloped and uniform lines. However, if the distance between drops is decreased from the uniform line scenario then the lines will experience bulging. If the

delay between drops is higher than the evaporation duration of a single drop then the line pattern will look like stacked coins. Sankir[51] printed PEDOT:PSS on polyethylene, polyimide and paper. It was found that the conductivity of printed line increases after the lines were treated with ethylene glycol and increase in width of the printed PEDOT:PSS line.

Moon et al.[52] printed binders for ceramics using both continuous and drop on demand printing systems. The authors were able to achieve better resolution with the drop on demand printing system. Their experiments demonstrated that lower surface tension binders results in poor drop formation and excessive spreading, thereby adversely affecting the resolution. Stringer and Derby[53, 54] used a Microfab inkjet printing system with a programmable x-y stage to print conducting silver lines. The authors found a region of stability for printed lines as a function of drop spacing, substrate wettability and speed of the stage. Osch et al.[55] used a MicroDrop inkjet printhead to print silver lines on teflon, polyarylate, PET, and Kapton substrates. The authors found that as number of printed layers is increased the conductivity of the printed silver lines increases. Perelaer et al.[56] printed silver lines on Kapton and found that an increase in the duration of sintering increases the conductivity of the silver lines. Smith et al.[57] used a Microfab inkjet printhead to print conductive silver circuits on glass fiber reinforced polymer, polyimide and carbon fiber reinforced polymer substrates. Sintering the printed silver lines at 150° C they reduced the resistivity of these lines as low as twice of the bulk silver. Wu et al.[58] improved the conductivity of silver nitrate lines on Kapton substrate by adding poly(N-vinyl-2-pyrrolidone) in ethylene glycol. By increasing the concentration of silver nitrate and temperature of substrate lead to increased conductivity of the printed

lines. Perelaer et al.[59] printed silver lines on substrates heated at 130° C so that the silver lines get sintered instantly. Increase in sintering duration improves electric conductivity of the printed silver lines. They also observed a change in the color of the printed silver lines as the silver lines became from colorless/transparent to brown after being deposited on the substrate, and then the color changes to shiny silver. Kang and Oh[60] printed conductive lines of nanosilver particles on substrates having different temperatures and found that when the temperature of the substrate increases the evaporation rate increases and the contact line pinning is enhanced and leads to stable lines. Jahn et al.[61] printed conducting silver lines on PET and glass substrates having conductivities of 18 and 43% of the bulk silver respectively after sintering.

Berg et al.[62] printed TiO_2 particles coated with poly(vinyl methyl ether)-block-poly(vinyloxy-4-butyric acid) (PVME-b-PVOBA) diblock copolymer in aqueous solution of dipropylene glycol. This ink undergoes gelation above 36.8° C. The authors observed that due to gelation of the ink at substrate temperatures higher than 36.8° C continuous line were printed on even hydrophobic surface as ink did not dewet due to the high viscosity of the ink. Park and Moon[40] tried to use mixtures of water and diethylene glycon and water and formamide to print silica particles and suppress the coffee ring effect in drops and lines in order to get uniform deposition. Kim et al.[63] also changed solvent composition to print continuous silver lines and suppressing the coffee ring effect due to Marangoni flow.

Tekin et al.[64] inkjet printed polystyrene films. For monosolvent systems the authors experienced coffee-ring effect, and used bi-solvent mixtures to suppress this mass transfer to the edge. Kang et al.[65] found that with fixed spacing between drops and lines a

film first experiences bulges and later separation. Later Soltman et al.[66] from the same group decreased the spacing between lines as the printhead moved away from the starting point film to compensate for the mass loss during evaporation to get continuous 2-D films.

1.3.6. Applications of inkjet printing

Xia and Friend[67] inkjet printed light-emitting diodes (LEDs) using a blend of poly (9,9'-dioctyfluorene-co-bnzothiadiazole) (F8BT) with poly(9,9-dioctylfluorene-co-N-(4-butylphenyl)diphenylamine) (TFB) and achieved similar performance compared with spin-coated LEDs. The thick edge produced by the "coffee-ring" effect common in drop evaporation[37] cover only 20~30% of the total printed area which does not generate adverse effects on the performance of inkjet printed LEDs. Xia and Friend[68] later used inkjet printing to form a pattern and then print LED on an indium tinoxide substrate coated with PEDOT:PSS and poly(4-vinylphenol). The authors printed ethanol on poly(4-vinylphenol) to etch the pattern, thus, replacing photolithography and then printed F8BT in p xylene on TFB layer to get functional LEDs.

Berg et al.[69] printed 20% and 40% weight dispersion of polyurethane (particle size 100-200 nm) suspension in water in order to create stepped and gradient rectangular structures. When the authors increased the weight fraction of polyurethane, uniformity of the printed structures were improved as a higher viscosity of the suspension suppresses the coffee ring effect. Ingrosso et al.[70, 71] printed chloroform based nanocomposite inks formed of CdS and differentially sized CdSe@ZnS nanocrystals embedded in polystyrene solution which can be integrated in polymer displays and colored wall papers. They

demonstrated that inks based on the single apolar, high vapor pressure and low boiling point solvent were effectively inkjet-printed into self-standing and disk-like microstructures.

Bohmer et al.[72] used inkjet printing to synthesize monodispersed polymer particles. The authors used precision and repeatability of inkjet printed drops, in printing polymer solution in another liquid while keeping the nozzle submerged. Kim et al.[73] printed zinc tin oxide thin-film transistors using inkjet printing having performance comparable to those of amorphous silicon-based transistors. Bhatti et al.[74] used a commercial inkjet printer to print microscopic arrays of lead zirconium titanate (PZT) at elevated temperature using polyvinylbutyral binder. Bathurst and Kim[75] also printed 400 nm thick PZT film, even though the performance was a little inferior compared to spin coated PZT film there was room for improvement. Adler-Abramovich and Gazit[76] used a commercial printer to print peptide nanotubes and nanospheres on patterned ITO coated plastic substrates. Boberl et al.[77] printed photodetectors operating up to 3μm wavelengths. The authors printed HgTe nanocrystals in chlorobenzene on a glass substrate at 60°C temperature.

Gans et al.[78] used acetophenone, ethyl acetate, isopropyl acetate, toluene, n-butyl acetate and anisole on polystyrene to generate holes by inkjet etching. The authors found that the drop generated holes that were three times the diameter of the drop. As the solvent wets the polymer film and formed a thin fluid film with a circular footprint with a thickness of a few microns. Jahn et al.[79] printed a solution of ethylene glycol and water on a hydrophobic surface to get microsieves. The authors printed the ethylene glycol

solution on an Al film and then added polymer solution creating micropores in the polymer film. Then they peeled off the polymer layer and obtained microsieves.

Bietsch et al.[80] used a Microdrop inkjet printing system to coat functional material on nanomechanical cantilevers. Self-assembled monolayers of alkanethiols were deposited on gold-coated cantilevers to enhance their sensitivity to ionic concentration and pH in liquids. Abe et al.[81, 82] printed biosensors on paper to detect glucose, protein and approximate pH. The authors soaked a paper of 1% polystyrene in toluene and then printed the chemical sensing inks on the soaked paper. Presence of glucose, protein and acidic/basic liquid changed the color of the sensing unit[81]. Presence of human IgG concentration down to 10 μg/l can be detected by 20 minutes[82]. Hossain et al.[83] developed a bioactive paper sensor to detect acetylcholinesterase using inkjet printing. The authors used various ink combination by changing viscosity of the ink to examine its effect on the response of the printed sensors.

Blau and Ugniwenko[84] printed living cells on different substrates and formed rectangle patterns. The authors were demonstrating that biological cells can survive the high stresses generated during the jetting cycle of the piezoelectric inkjet printing nozzle. Xu et al.[85] printed living E. coli bacterium using two different commercial inkjet printers. The authors printed E. coli in complex patterns and high concentration colonies with varying concentrations. Roth et al.[86] printed protein solutions in different patterns demonstrating high throughput of inkjet printing. The authors used a commercially available thermal inkjet printer and created viable cellular patterns with a resolution of 350 μm. Boland et al.[87] demonstrated the viability of printing mouse endothelial cells in 3D structures using a commercially available thermal inkjet printer. The authors printed

these cells dispersed in $CaCl_2$ solution into sodium alginate and formed hydrogel by cross-linking. Printed cells were sustained in hydrogel which allowed formation of 3D structures. Xu et al.[88] printed mammalian cells using a thermal inkjet printer in patterns onto gel-based bio-papers. The authors used buffer solutions and found that more than 90% of cells were not damaged. Biase et al.[89] developed a biocompatible fluid to form rectangular wells of living cells in hydrogel. The authors found that deposition behavior of these cells was similar to the deposition of nanoparticles in suspension.

Hoth et al.[90] printed photoactive layer of P3HT:PCBM dissolved in tetralene, ortho-dichlorobenzene (oDCB) and mesitylene in a glass/indium tin oxide/PEDOT:PSS/P3HT:PCBM/CaAg solar cell. The addition of mesitylene in oDCB induced concentration gradient driven Marangoni flow inside the evaporating drops and helped the formation of a uniform film of P3HT:PCBM. The authors were able to achieve 3% efficiency with this printed solar cell. Later the same authors[91] modified the concentration of P3HT and further improved the efficiency of the solar cells from 3% to 3.5% and 5%. Aernouts et al.[92] printed PEDOT:PSS and P3HT:PCBM in a indium tin oxide/PEDOT:PSS/P3HT:PCBM/Al solar cell. The authors printed a mixture of P3HT and PCBM in 1:1 solution of chlorobenzene and tetraline to improve the uniformity the printed layer. Eom et al.[93] printed PEDOT:PSS layer in a indium tin oxide/PEDOT:PSS/P3HT:PCBM/LiF-Al solar cell. The authors added glycerol and EGBE in aqueous PEDOT:PSS solution to improve uniformity of deposition and conduction, thus, improving overall performance of the solar cell with 3.16% efficiency.

1.3.7. Summary

As the size of the drops shrinks from millimeter to micron scale, surface tension becomes more dominant in determining the final morphology of deposited functional materials. Derby[94] summarized progress in drop formation, drop impact and spreading in inkjet printing. He also reviewed stability and resolution of inkjet printed lines as a function of wettability of the substrate, successive drop spacing and delay. More has been discussed and reviewed regarding application of inkjet printing in the last decade[95-103]. Despite the recent progress in understanding drop spreading and evaporation, as well as particle deposition in inkjet printing, effects of environmental condition, particle size and type of particles on particle assembly are unknown for the smaller volume of the inkjet-printed drops.

Explanation of these questions will lead to better controlled deposition morphologies, making inkjet printing a more robust method for low cost electronics manufacturing[103], photovoltaics fabrication[101], and bioprinting for tissue engineering[100, 104]. Inks containing metal nanoparticles can be deposited into lines and sintered at a low temperature (~100-150 °C). Ability to form repeatable small drops on demand can be useful in titration in biological[105] and pharmaceutical[97] applications.

1.4. Objectives

The objective of this study is to advance the fundamental understanding of the complex physical processes involved in inkjet deposition of colloidal drops using fluorescence microscopy. The knowledge obtained is important in achieving better controlled deposition morphology and properties of printable electronics and

photovoltaics. Compared to other solvent based processes here the small volume of the drops makes surface tension and evaporation rate very dominant factors. The specific goals of this present study are to:

1. Examine the effect of the relative humidity (RH) on contact angle and deposition morphology;
2. Examine the effect of van der Waals, electrostatic and surface tension forces in pinning of the particles near the contact line as a function of substrate wettability;
3. Examine the effect of drop coalescence on deposition morphology for a range of drop spacing and temporal delay between drops;
4. Examine the effect of particle shape on coffee ring suppression;
5. Explore the application of inkjet printing for conducting lines; and finally
6. Explore the fabrication of printable organic solar cells.

1.5. Organization of chapters

In the first chapter background information about inkjet printing is provided along with the literature review and stated goals. Experimental setup is described in the second chapter. Afterwards chapters 3, 4 5and 6 focus on fundamentals of inkjet printing where effects of relative humidity, particle size, coalescence of drops and particle shape on particle deposition are studied respectively. Chapters 7 and 8 utilize findings from chapters 3-6 in printing of stable lines and solar cells. Chapters 3 4and 7 are already published and chapters 5 and 6 are submitted for publications.

the fund

Chapter 2 : EXPERIMENTAL SETUP AND PROCEDURE

The aim of the experimental setup is to observe in real time evaporation and particle deposition of inkjet printed colloidal drops from side and bottom views. An experimental setup is built to observe the drop formation at the end of the piezoelectric nozzle from the side-view and to observe the drop evaporation onto a glass substrate from the side-view using a drop observation system. A CCD camera is attached to an inverted fluorescence microscope to observe evaporation from the bottom-view. A schematic of the inkjet printing experimental setup is shown in Fig. 2.1.

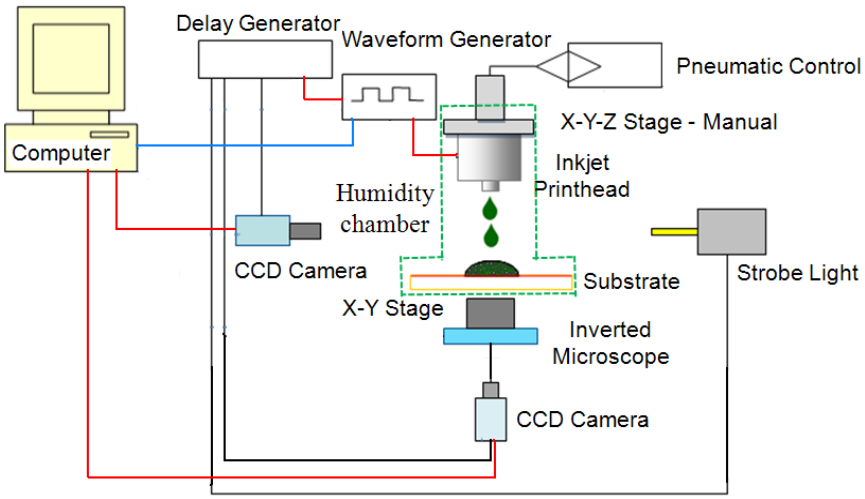

Figure 2.1. Schematic of experimental setup for real time observation of droplet evaporation in inkjet printing.

The experiment is divided into two major parts: (i) drop formation and (ii) in-situ observation of drop evaporation. Drop formation is essential as repeatable drops are needed to study the drop evaporation and particle deposition. The observation of drop formation and evaporation from side view involves a computer, a piezoelectric nozzle, a

waveform generator, a delay generator, a CCD camera (Sensicam QE) and a strobe light. Drop evaporation and particle deposition observation from the bottom-view involves a computer, a piezoelectric nozzle, a waveform generator, a delay generator, a CCD camera and a fluorescence microscope.

2.1. Ink preparation

A lot of industrial material deposition processes involve suspensions, such as metal nanoparticles suspended in carrier liquid or biological species in carrier liquid etc. Stability of the suspension is improved by having the density of the particles to be closer to carrier liquid, as settling time of the particles increases. A commercially available ink from Invitrogen molecular probes with carboxylate modified polystyrene beads of 1.1 μm, 100 nm and 20 nm in diameter in water are used after diluting the suspension from 2 to 0.5% by volume. The carboxylate modification gives them an anti-binding property which prevents them from agglomerating and hence gives a stable suspension. Ink obtained from manufacturer contains 2% volume fraction, and is usually diluted by adding DI water. The prepared solution is then sonicated for an hour to disperse the particles inside the colloidal mixture. The yellow-green fluorescent polystyrene spheres suspended in the inkjet drop were tracked using the bottom view images of drop evaporation from the start of capture until final evaporation and deposition.

2.2. Inkjet printhead and control

A piezoelectric printhead with a nozzle diameter of 60 μm (MicroFab Technologies Ltd) is used to generate the drops at 1 to 2000 Hz at 14 to 1100 pico liter

(diameter of the nozzle should be 50 times the diameter of the particles[9], for 60 μm diameter nozzle, particle diameter should be less than 1.2 μm). Jetdrive sends a voltage pulse to the piezoelectric transducer around the glass capillary tube. Voltage waveform amplitude (+65 to -65V) and pulse width (50 to 200 μs) are controlled by a jetdrive waveform generator.

Pressure is applied to the liquid in the reservoir using a pneumatics control console from Microfab, which includes pressure and vacuum regulators. The pneumatic controller allows for the maintaining of positive as well as negative pressure on the printhead depending on the viscosity and surface tension of the ink. Positive and negative pressures are required while cleaning the inkjet dispensing device and also while jetting to maintain constant liquid pressure at the orifice.

2.3. Drop observation

Drop observation is carried out for two primary purposes: (i) observation of drop formation, and (ii) observation of drop evaporation. Drop evaporation is observed from two viewing angles, side and bottom. Drop observation is synchronized with drop ejection from the piezoelectric nozzle by using the delay generator (DG645).

2.3.1. Side-view observation

A Sensicam Qe CCD camera coupled with a halogen strobe (Perkin Elmer) is used to form a drop observation system. The drop observation system is synchronized with the piezoelectric printhead through the delay generator. The camera captures 10 frames per second at full CCD resolution of 1376 X 1040 pixels or $0.538 \times 0.538\ \mu m^2$ (at

12× magnification) and at a short exposure time of 500 ns. The halogen strobe coupled with the camera provides short duration light pulses of high intensity and has a maximum flash rate of 60 Hz. Diameter and contact angle measurements of the drop for side-view images have been carried out using IMAGEJ (http:// rsbweb.nih.gov/ij/).

For repeatable phenomena such as drop formation, the flash photography technique is used to adjust delay times for the printhead and drop observation, where the printhead and the drop observation system are synchronized. By increasing the delay times of the drop observation system in steps of 10 μs, images progressively farther in time from the actuation are captured. Combination of these images provides a sequence of images of drop formation with a temporal resolution of 10 μs.

2.3.1.1. Measurement of drop diameter and velocity

The drop diameter of a single drop generated varied from 30 to 80 μm. The drop observation system is used to measure the diameter and velocity of the drops using the flash photography technique. Velocity control was attained by means of varying the voltage waveform that drives the piezoelectric crystal. The resulting velocities ranged from about 0.5 m/s to 2.0 m/s. Advanced triggering options in the delay generator allows observation of drop formation at frequencies higher than 10 Hz. At higher frequencies, say at 50 and 500 Hz every 5^{th} and 50^{th} drop is observed.

Travelling velocity of the drop is measured by changing the delay between printhead and the camera and drop observation system. Jetdrive (waveform generator) is used to change the delay between the pulses sent to the printhead and the drop observation system.

2.3.1.2. Drop evaporation

Advanced triggering options in the delay generator allows inkjetting of drops at frequencies lower than 1 Hz. Drop evaporation is observed at 10 Hz and is synchronized with the inkjet printhead in such a manner that the first frame of the evaporating drop is observed at 100 ms after ejection of the drop from the nozzle. This 100 ms delay allows completion of drop impact and spreading on the substrate. Drop evaporation is observed until no more changes are observed from the side-view. Usually, after contact angle of the drop reaches below 5° side-view does not change.

2.3.2. Bottom-view observation

SONY XCL-5005CR camera attached with an inverted microscope (Zeiss Axio Observer) is used to observe the evaporation of the drop from the bottom-view. Resolution of the camera is enhanced from 3.45 μm × 3.45 μm by using 10× and 40× objectives with 0.63×, 1× and 1.63× attachments. Fluorescent particles of 1.1 μm diameter are used as tracer particles. Fluorescent filter sets 38 endow GFP (excitement 450/490, and emission 500/550) and 45 HQ texas red (excitement 540/580, and emission 595/665) are used with the inverted microscope. The camera can take pictures at 15 fps, but it is used at 10 fps to compare data with side-view observations.

2.4. Humidity control

An environmental (humidity) chamber was built to house the printhead, camera, strobe-light and microscope. A schematic of the humidity chamber is shown in Fig. 2.2.

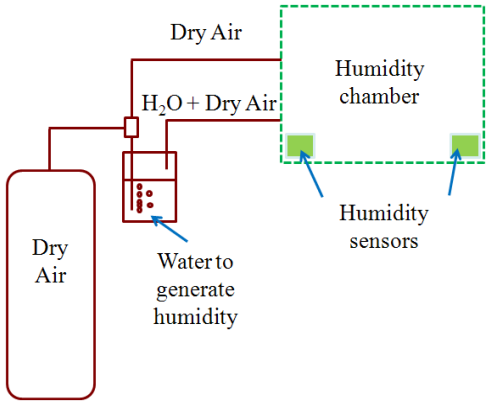

Figure 2.2. Schematic of the humidity chamber.

Humidity was controlled by allowing dry air or humid air (H_2O + dry air) inside the humidity chamber between 10 to 90%. Two OM-DVTH humidity sensors (±2% RH, from 10 to 90% RH) were kept inside the humidity chamber apart from each other as shown in Fig. 2.3. After stopping the airflow inside the chamber, ten minutes are allowed for humidity to reach equilibrium. The experiment is then carried out in next hour to keep the variation in humidity less than ±3%.

2.5. Substrate wettability modification

To obtain substrates with varying degrees of wettability, glass microscope cover slips (Bellco, ~150µm thick) underwent a sequence of cleaning, silanization, and plasma treatment. First, substrates were cleaned by sonicating in Sparkleen-DI water solution, ethanol and acetone for fifteen minutes each. Then they were immediately dried in a stream of compressed air and treated with Argon gas plasma (2 minutes each side at 18W and 250mtorr, Harrick Plasma PDC-32G). Silanization consisted of soaking the substrates for one hour in a 5mM solution of octadecyltrichlorosilane (OTS (CH_3-

$(CH_2)_{17}$-$SiCl_3$)) in hexane (both from Sigma Aldrich and used as received). This silanization was carried out inside a dry glove box with a controlled N_2 atmosphere to minimize excessive polymerization of the water-sensitive OTS molecules. Varying degrees of wettability (different receding contact angle θ_{RCA}) were obtained on the substrates by subjecting the already silanized surfaces to time-varying treatments of Ar plasma. A schematic of the procedure for substrate preparation is shown in Fig. 2.3

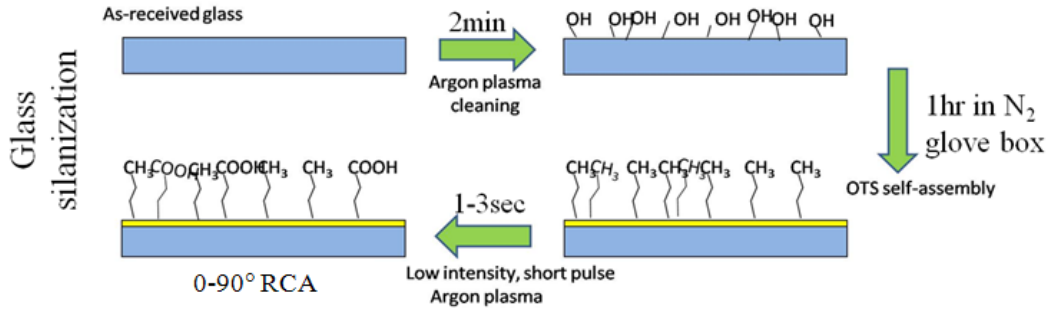

Figure 2.3. Schematic of the substrate preparation.

Low-power plasma treatment of a silanized surface functionalizes silane monolayer from hydrophobic (-CH_3) to hydrophilic (-COOH) terminal group[106]. Increasing duration of the plasma treatment generates a larger concentration of hydrophilic surface components, effectively increasing the surface wettability. In the current study, the time of treatment from 2 to 60 seconds at a power level of 6W and 250mtorr Argon pressure was used to produce systematically varied wettability of glass surfaces with no measurable change in surface roughness.

2.6. Contact angle measurement

Static advancing (θ_{ACA}) and static receding (θ_{RCA}) contact angles of the substrates were measured by using a goniometer setup using a micropipetted droplet containing DI-water to minimize the effects of evaporation and the presence of particles. The goniometer setup was built with Basler a601-f camera (9.2 μm × 9.2 μm resolution at 60 fps) and a cold light source.

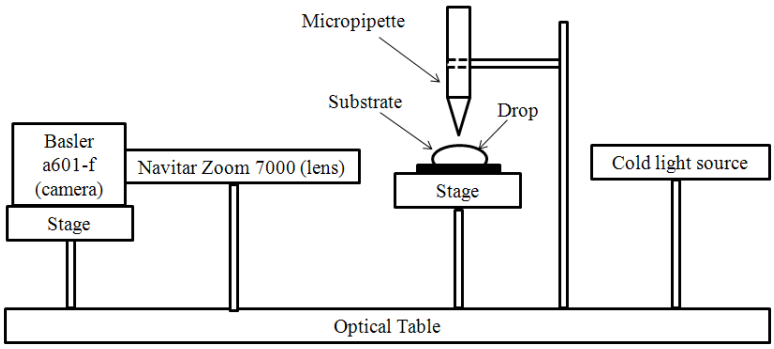

Figure 2.4. Schematic of the goniometer setup to measure contact angle of the liquid drop.

As shown in Fig. 2.4, a drop of DI water is put on the substrate. By addition/removal of water from the drop on the substrate the static advancing (θ_{ACA}) and static receding (θ_{RCA}) contact angles of the substrates are measured. Contact angles of the drops are measured by using ImageJ for 3 to 5 different drops on the substrate at different locations.

2.7. Microscope stage control

Ludl 96S106-Z3 stage is used to put a drop on the substrates at the desired location. The stage is controlled by a Mac6000 controller, through a computer. The stage is precisely controlled with a resolution of 50 nm and maximum velocity of 60 mm/sec with accuracy of ± 3μm. The controller is programmed to move the stage linearly to print 2-D and 3-D structures on substrates.

Chapter 3 : EFFECT OF RELATIVE HUMIDITY ON CONTACT ANGLE AND DEPOSITION MORPHOLOGY

3.1. Introduction

Pico liter aqueous colloidal drops used in inkjet printing evaporate within seconds, leaving evaporative and Marangoni flows as the dominant factors affecting particle deposition. The relative humidity (RH) of the ambient air is one of the several factors that affect the evaporation rate[†]. Besides the fact that RH directly influences the drop evaporation rate, i.e., a drop evaporates faster at lower RH values, Anderson and Davis[107] demonstrated that evaporation rate affects the spreading behavior of a liquid drop. Their analysis showed that the increase in dynamic contact angle during drop spreading is a result of the difference between the liquid velocity near the contact line and the contact line velocity, induced by drop evaporation. Similarly, evaporation rate affecting the spreading of liquid films has been demonstrated by Ajaev et al.[108], where the evaporation rate is modified by heating the substrate. However, the effect of evaporation rate on colloidal drop spreading and subsequent particle deposition has not been examined in detail, although this process is at the core of emerging technologies such as inkjet-printing-based additive manufacturing of functional materials into printable electronics and photovoltaics[99, 109, 110]. In this chapter, we present experimental results for

---

[†] Chhasatia, V. H.; Joshi, A. S.; Sun, Y., Effect of relative humidity on contact angle and particle deposition morphology of an evaporating colloidal drop. *Applied Physics Letters* 2010**,** 97, 231909.

inkjet-printed, evaporating pico liter aqueous colloidal drops, where the mass loss due to evaporation is significant.

3.2. Experimental details

The drop evaporation rate is modified by changing the RH inside an environmental chamber. A colloidal mixture of carboxylate-modified polystyrene fluorescent beads of 1.1 /m diameter in de-ionized water, 0.5% by volume, is used. Pico liter drops are generated using a piezoelectric-driven inkjetting nozzle (MicroFab MJ-AL-01-60, Plano, Texas). A high resolution (0.5 μm/pixel) charge-coupled device (CCD) camera system, consisting of a Sensi-Cam QE CCD camera (Romulus, Michigan) and a Navitar 12X Zoom lens (Rochester, New York), is synchronized with a halogen strobe light and the drop ejection to form a high magnification goniometer for side-view observation of drop evaporation.

Particle motion and deposition inside the colloidal drop are observed using a Zeiss inverted fluorescence microscope (Thornwood, New York) with a 20X objective and bottom-view images are captured by a Sony XCL-5005CR CCD camera (Park Ridge, New Jersey). The bottom-view and side-view cameras are both capable of capturing more than 10 frames/second. The RH levels inside the environmental chamber are controlled by supplying either dry or humid air, and RH levels of 10%, 30%, and 60% are obtained during the experiments. The ambient temperature is kept at 22 °C for all experiments. Contact angle measurements for side-view images have been carried out using IMAGEJ (http:// rsbweb.nih.gov/ij/) assuming that the drop interface remains a spherical cap at all

times. Neglecting gravitational distortion of the drop surface is justified because the Bond number is less than 0.005.

3.3.Results and discussion

Figure 3.1 shows the evaporation dynamics of an inkjet printed aqueous colloidal drop on a glass substrate. The base radius of the drop is denoted by R_b and the radius of the spherical cap is R. Upon impact, the inkjet-printed colloidal drop spreads to its maximum radius on a glass substrate within the first 0.1 s. The drop contact line is then pinned at this maximum radius, due to chemical heterogeneity or nanoscale roughness of the substrate, and remains pinned during the entire drop evaporation process, as shown in both sides [Fig. 3.1(a)] and bottom view [Fig. 3.1(b)]. The decrease in the drop height and contact angle e is observed in the side-view images as time progresses. Bottom-view images [Fig. 3.1(b)] show the evaporatively driven motion of individual 1.1 /m particles toward the pinned contact line. These particles further enhance contact line pinning. It is observed that the contact angle reduces to almost 0° during the final stages of evaporation. However, as shown in Fig. 3.1(c), the water film starts to recede near the end of the evaporation as significant mass loss due to evaporation, which makes the maintenance of the film unsustainable, leaving colloidal particles to form a coffee-ring deposit on the substrate. Film evaporation can only be observed in the bottom view because once the contact angle (θ) of the drop falls below 5°, side-view images appear similar from 0.9 to 2.1 s.

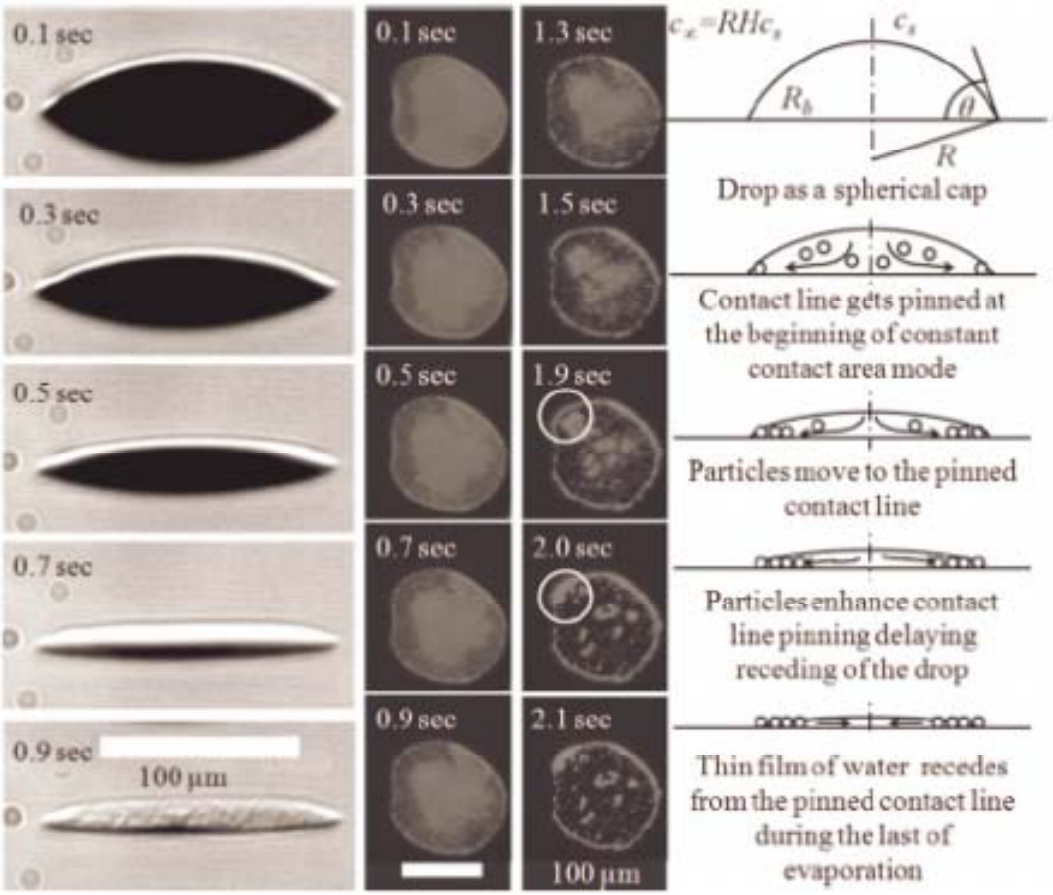

Figure 3.1. Snapshots of a drying colloidal drop at 60% relative humidity on a glass substrate from (a) side-view, (b) bottom-view, and (c) schematic of the pinned evaporation process. Particle movement toward the pinned contact line can be observed clearly between 1.9 and 2 s (circled areas).

One of the central themes we want to explore in this letter is the effect of evaporation rate on the contact angle. Empirical studies of the spreading of nonvolatile liquids on solid surfaces have led to a constitutive relation between the instantaneous (dynamic) advancing contact angle θ_A and the fluid velocity parallel to the substrate (U_{CL}), which is given by[107]

$$U_{CL} = \zeta\left(\theta_A - \theta_{ACA}\right) \tag{3.1}$$

where θ_{ACA} is the static advancing contact angle, ζ and m are the empirically determined constants. In the absence of evaporation, the contact line velocity dR_b/dt is equal to U_{CL}, satisfying mass conservation. However, if there is an evaporative mass loss J, the appropriate form of mass conservation is now given by[107]

$$\frac{dR_b}{dt} = U_{CL} - \frac{J}{\rho \sin\left(\theta_A^{'}\right)} \tag{3.2}$$

where $\theta_A^{'}$ is the (instantaneous) advancing contact angle in the presence of evaporation. Recent experiments for volatile liquids[108] have revealed that $\theta_{ACA}^{'} > \theta_{ACA}$, and $\theta_A^{'} > \theta_A$. Following Anderson and Davis[107], we assume that an expression similar to Eq. (3.1) is applicable even for volatile drops, which implies that

$$U_{CL} = \zeta\left(\theta_A^{'} - \theta_{ACA}^{'}\right)^m \tag{3.3}$$

While the exact validity of Eq. (3.3) is not yet known, our conclusions will not be affected as long as U_{CL} increases with $\theta_A^{'} - \theta_{ACA}^{'}$.

At the precise instant in time when the contact line reaches its maximum radius and gets pinned,

$$dR_b/dt = 0$$

and Eq. (3.3) can be combined with Eq. (3.2) to obtain

$$\rho \sin\left(\theta_A^{'}\right)\zeta\left(\theta_A^{'} - \theta_{ACA}^{'}\right)^m = J\,.$$

Thus, $J > 0$ implies that

$$\theta_A - \theta_{ACA} > 0$$

Equation (3.3) implies that $\theta_A^{'} - \theta_{ACA}^{'} > 0$ during the initial spreading process (moving contact line). However, the above analysis shows that when $J > 0$, $\theta_A^{'} - \theta_{ACA}^{'} > 0$ even when the contact line has reached its maximum radius and has stopped moving. Although $\theta_{ACA}^{'}$ increases with J[108], it can be argued that the difference $\theta_A^{'} - \theta_{ACA}^{'}$ remains approximately constant and does not vary significantly with J. In this case, the measured contact angle $\theta_{ACA}^{'}$ clearly increases with J because $\sin\left(\theta_A^{'}\right)$ is proportional to J.

Figure 3.2 plots the experimentally measured contact angle θ as a function of time for various RH values. It can be observed that the initial value of θ (when the contact line pins) is larger for higher evaporation rates (larger J, lower RH), confirming our theoretical analysis. The angle θ subsequently reduces for each RH value because of continued contact line pinning and evaporation. Note that the above theoretical analysis is valid only until the contact line first pins and the subsequent reduction of θ with time, as shown in Fig. 3.2, is dependent solely on the evaporation rate. For each RH value, contact angle measurements are carried out until the side-view images no longer change with time, typically until $\theta < 5°$. As discussed before (Fig. 3.1), we recognize that the evaporation process is not complete at this point, but measurement of contact angles (using the side-view camera) is no longer meaningful beyond this point. Therefore, reported values of the evaporation time for experiments correspond to these side-view observations. Each data point in Fig. 3.2 is the average contact angle for five different drops at different locations on the substrate and error bars represent the standard deviation.

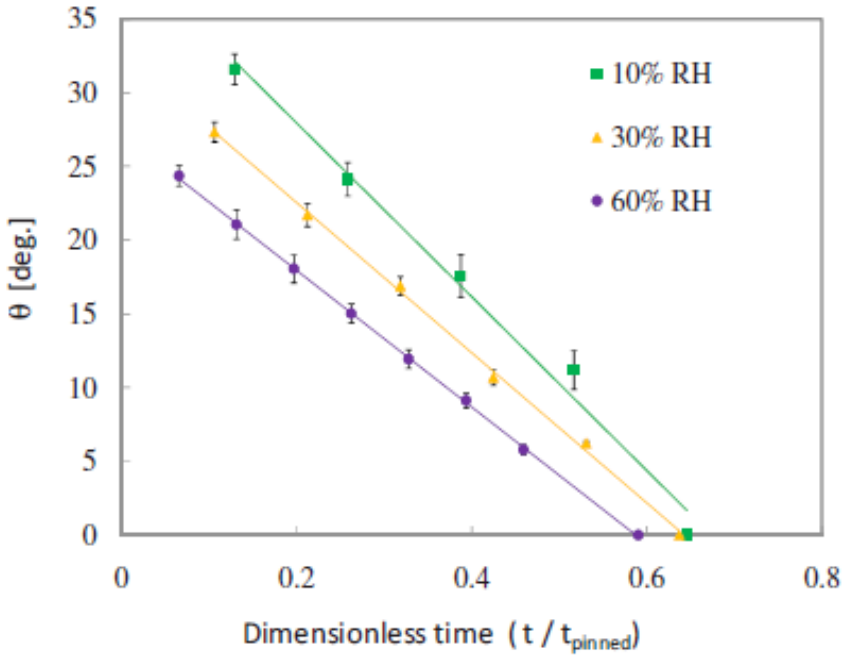

Figure 3.2. Contact angle of the drop as a function of nondimensional time at different RH values.

To gain more insight into the evaporation process, the experimental time for each RH value in Fig. 3.2 has been scaled by the theoretical evaporation time for that RH value for a pure water drop. Birdi et al.[18] expressed the rate of evaporation as

$$\rho\left(dV/dt\right) = -4\pi R^2 D\left(dC/dr\right)$$

in the quasisteady-state diffusion-driven evaporation of a spherical water drop of radius R, where V is the volume of the drop, D is the diffusion coefficient of water vapor in the air, and C is the water vapor concentration in air. It is assumed that $C = C_s$ (saturated concentration) at the drop surface and $C = C_\infty$ far away from the drop surface. With these boundary conditions, the evaporation rate can be expressed as

$$\rho\frac{dV}{dt} = -4\pi DR\left(C_s - C_\infty\right)F\left(\theta\right) \tag{3.4}$$

where $F(\theta)$ is a function introduced by Picknett and Bexon[111] to accommodate the effect of a solid surface on the vapor field. By making an analogy to an electrostatics problem of evaluating the capacitance of a conductor of the same shape as the sessile drop, an exact $F(\theta)$ was obtained by a finite polynomial fit[111]:

$$F(\theta)=\frac{1}{2}\times\begin{cases}0.6366\theta+0.09591\theta^2-0.06144\theta^3 & \text{when } 0^\circ\le\theta\le 10^\circ\\ 0.00008957+0.6333\theta+0.116\theta^2-0.08878\theta^3+0.01033\theta^4 & \text{when } 10^\circ\le\theta\le 180^\circ\end{cases}$$

The volume of a spherical cap with base radius R_b and contact angle θ [see Fig. 3.1(c)] is given by

$$V=\frac{1}{3}\pi R_b^3\beta(\theta)$$

where $\beta(\theta)=\left[2-3\cos(\theta)+\cos^3(\theta)\right]\Big/\sin^3(\theta)$. Using this relationship defining $RH=C_\infty\Big/C_s$, Eq. (3.4) can be written as

$$\frac{\pi R_b^2}{3}\frac{d}{dt}\beta(\theta)=\frac{-4\pi DC_s(1-RH)}{\rho\sin(\theta)}F(\theta) \tag{3.5}$$

Further rearrangement of Eq. (3.5) leads to

$$\frac{d\theta}{dt}=\frac{-4DC_s(1-RH))}{\rho R_b^2}\frac{2+\cos\theta}{\beta(\theta)}F(\theta) \tag{3.6}$$

Equation (3.6) may be integrated to solve for the time interval the drop spends in the pinned stage of the evaporation (t_{pinned}), which is thus given by

$$t_{pinned}=\frac{\rho R_b^2}{4DC_s(1-RH)}\int_0^\theta\frac{\beta(\theta)}{(2+\cos\theta)F(\theta)}d\theta \tag{3.7}$$

For a fixed value of RH, the contact angle decreases linearly with time, as shown in Fig. 3.2, which is consistent with the observations in literature[18] for a fixed evaporation

rate. Theoretical values of t_{pinned} using Eq. (3.7) for 10%, 30%, and 60% RH are 0.8, 0.9, and 1.5 s, respectively. The actual evaporation times in our experiments are 0.5, 0.6, and 0.9 s, respectively. These discrepancies are thought to arise because of two reasons: (i) the presence of suspended particles in experiments, which is not accounted for while deriving Eq. (3.7) above, and (ii) the evaporation time reported for our experiments corresponds to observations from the side-view camera and does not include the time spent in the final stages of evaporation, which is more akin to film evaporation, as discussed earlier with reference to Fig. 3.1(c).

Finally, we observe that the particle deposit area A, which is the area bounded by the outer edge of the coffee ring, decreases as the RH increases. To quantify this increase in area, we calculate the deposition diameter (*d*) by measuring the contact area *A* using IMAGEJ and using the relation $A = \pi d^2/4$ to calculate the diameter. The bottom-view images of the particle deposits and the deposit diameters for different RH values are shown in Fig. 3.3. At 10% RH, the final particle deposition diameter is 120 μm, and this diameter increases with increasing RH. Each data point in Fig. 3.3 is the average of ten diameter measurements for ten different deposits at different locations on the substrate, and error bars represent the standard deviation. Because the contact line does not recede during evaporation, deposition diameter changes very little during the final stages of the evaporation resulting in deposition area similar to the initial drop spreading area. The observed higher deposition diameter at higher RH (low evaporation rate) can be attributed to a lower contact angle during spreading, as discussed before and shown in Fig. 3.2. It can also be observed from Fig. 2.3 that the circularity of the final deposit deteriorates with increasing RH. This is probably caused by an enhancement of the effect

of local nonuniformities on the glass substrate at lower contact angles.

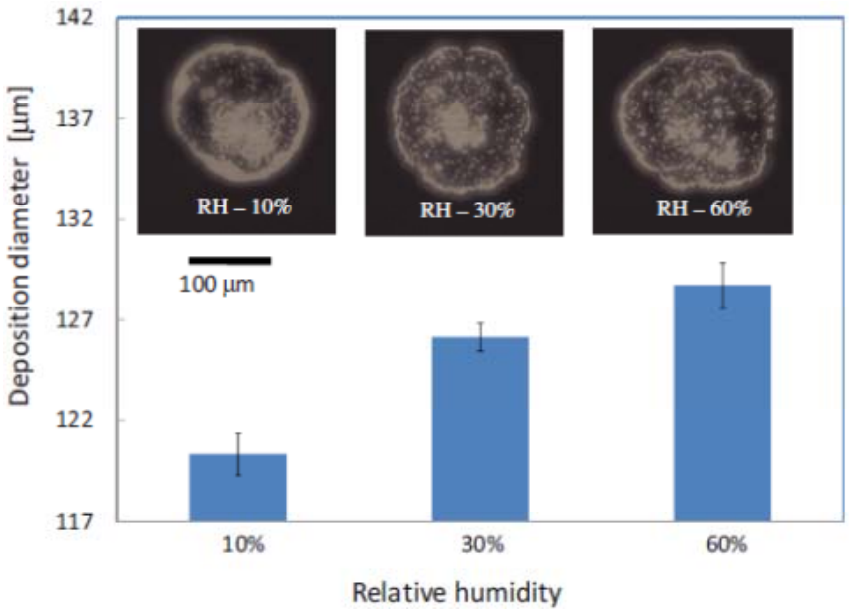

Figure 3.3. Final deposition morphology as a function of the RH. The scale bar (100 µm) is the same for all images.

3.4. Conclusions

Due to the small (pico liter) volume of the drops in inkjet printing, the RH becomes a dominant process parameter, dictating evaporation rates and deposition dynamics of aqueous colloidal drops. It is found that as the RH increases, slower evaporation results in lower contact angle of the drop and more spreading. More spreading of the drop leads to a larger particle deposition area for a pinned drop. Thus, controlling the RH is critical in ensuring repeatability of deposited patterns in inkjet printing of aqueous ink.

Chapter 4 : INTERACTION OF BI-DISPERSED PARTICLES WITH CONTACT LINE

4.1. Introduction

Evaporation of a sessile drop containing pure liquid usually occurs in three distinct stages[19], first the constant contact area mode where the contact line (CL) is pinned, followed by the constant contact angle stage where the drop contact angle reaches below the static receding contact angle and the CL depins, and finally the mixed mode where both contact area and contact angle decrease. The addition of particles in a colloidal drop extends the lifespan of the constant contact area stage. This is due to the fact that accumulation of particles along the drop edge driven by evaporation enhances CL pinning. The decrease in contact angle due to evaporation is offset by the increase in contact angle caused by new protruding ‡particles to the CL[112]. This delay of the second and third stages of evaporation in the presence of particles causes the well-known coffee-ring effect. Previous studies within our group[113], as well as others[9], have demonstrated that the particle size and contact angle between carrier liquid and substrate determine the distance away from the CL a particle gets deposited. Smaller particles move closer to the pinned CL compared to larger particles due to the liquid meniscus physically restricting the movement of larger particles.

The co-existence of micro and nanoparticles further complicates the interactions between particles and the CL. Increasing interest in using a receding liquid-vapor

---

Chhasatia, V. H.; Sun, Y., Interaction of bi-dispersed particles with contact line in an evaporating colloidal drop. *Soft Matter* 2011**,** 7, 10135-10143.

interface to guide size-dictated particle separation in evaporating drops has been developed in recent years[112, 114-120]. For example, effective isolation of virus, bacteria, and biological cells from body fluids is important to improve the sensitivity and accuracy of disease detection[116]. In the meantime, this size-induced particle separation presents a new challenge to the uniform deposition of inkjet-printed functional materials because particles of different sizes can aggregate at different locations in the final deposition. Weon and Je[120] studied the deposition of a colloidal drop containing bi-dispersed particles and showed that the liquid-vapor interface forms a wedge in the CL region and separates particles according to their sizes in an evaporating drop. The particle separation distance, *x*, between the outermost large and small particles is given by $x = r/\tan(\theta/2)$, where *r* is the radius of the particle and θ is the angle of the CL wedge. Evolution of the contact angle in time can be described by the following empirical power-law dependence[121]

$$\theta(t) = \theta_0 (t_0 - t)^{\beta} \tag{4.1}$$

where t_0 is the total time for evaporation, θ_0 and β are fitting parameters. Birdi et al.[18] explained that, for a drop with a pinned CL, the height of the drop decreases linearly with time for a drop of a low contact angle (~<30°). Increase in separation distance with time can thus be simplified as[120]

$$x(t) = \left(\frac{2r}{\theta_0}\right)(t_0 - t)^{-\beta} \tag{4.2}$$

It has been observed[114, 116, 120] that, for a colloidal drop containing micro and nanoparticles, the micron-sized particles move radially inward during the final stage of evaporation whereas the nano-sized particles remain at the drop CL. Wong et al.[114]

explained that, for a pinned CL, particles can either remain at the CL or move radially inward during drop evaporation, depending upon the balance between the attraction forces among the particles and the surface tension force acting on particles. For a large number of particles forming a monolayer along the CL, the attraction forces between particles can be stronger than the surface tension force and the particles remain pinned at the CL.

Previous studies on the deposition of bi-dispersed particles from evaporating colloidal drops[114-120] suggest that the liquid-vapor interface form a wedge at the drop CL and this wedge shape prevents particles from protruding through the liquid-vapor interface. Except for Wong et al.[114], the research focus so far has been on particle separation on hydrophilic substrates with a pinned CL inside a micron-sized sessile drop. In this paper, we present experimental results for inkjet-printed, evaporating aqueous colloidal drops containing 100 nm and 1.1 μm particles deposited on glass substrates of varying wettability. Pico liter colloidal drops produced by an inkjet printer represent a common drop size widely used for high-resolution materials printing applications. In such length scales, capillary and evaporation are the dominating mechanisms, whereas gravitational and inertia effects are negligible. The forces acting on the micro and nanoparticles, particle separation distance, as well as the pinning and depinning of the CL have been investigated on systematically varied substrates with a static contact angle ranging from 5° to 95° (measured using a pure water drop to eliminate the effect of particles). We also report the possibility of micron-sized particles protruding through the liquid-vapor interface for the case of a hydrophilic substrate, where the actual distance

between the outermost micro and nanoparticles is less than the value suggested by the CL wedge assumption.

4.2. Experimental details

A colloidal mixture of carboxylate-modified polystyrene fluorescent beads of 100 nm and 1.1 μm diameter in DI-water, each 0.5% by volume, was used in our inkjet printing experiments. Pico liter drops were generated using a piezoelectric-driven inkjetting nozzle (MicroFab MJ-AL-01). A high resolution (0.5 μm/pixel) image acquisition system, consisting of a SensiCam QE CCD camera (Romulus, Michigan) and a Navitar 12× Zoom lens (Rochester, New York), was synchronized by using a delay generator (SRS DG645, Sunnyvale, California) with a halogen strobe light and the drop ejection to form a drop side-view observation system. Particle motion and deposition inside the colloidal drop were observed from the bottom using a Zeiss inverted fluorescence microscope (Thornwood, New York) with a 40× objective and bottom-view images were captured by a Sony XCL-5005CR CCD camera (Park Ridge, New Jersey) at 10 frames per second. The ambient temperature and humidity were kept at 22 °C and 20 % relative humidity for all experiments.

4.3. Forces acting on particles near a CL

As shown in Fig. 4.1a, colloidal particles in an evaporating drop experience van der Waals and electrostatic interactions with other particles, as well as with the substrate near a CL. Here, we focus on the regime of large Peclet numbers (the ratio of shear-

driven to Brownian motion at the particle scale) and neglect the random force causing Brownian motion and the non-DLVO forces acting on the particles.

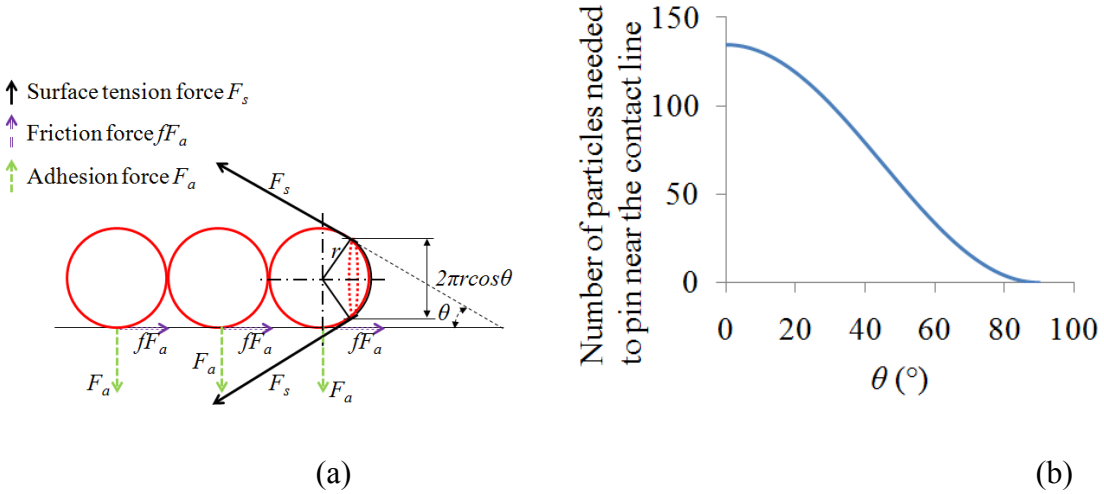

(a) (b)

Figure 4.1. Forces acting on particles near a CL. (a) Schematic of surface tension, adhesion, and friction forces acting on particles near a CL and (b) number of particles required to pin themselves near the contact line as a function of contact angle.

4.3.1. van der Waals interaction

The particle-substrate van der Waals force, F_{wps}, between particles and the substrate in a fluid medium is given by[122]

$$F_{wps} = \frac{2nA_{123}r^3}{3z^2(z+2r)^2} \tag{4.3}$$

where n is the number of particles, A_{123} is the Hamaker constant where the subscript 1 denotes the particle, 2 is the substrate, 3 denotes the fluid medium, and z is the particle-substrate separation distance. This particle-substrate adhesive force attempts to keep the particles near the substrate. Also, the van der Waals force acting among particles in a fluid medium, F_{wpp}, can be calculated by[122]

$$F_{wpp} = \frac{nA_{131}r}{12z^2} \tag{4.4}$$

where A_{131} is the Hamaker constant between particles in a fluid.

4.3.2. Electrostatic interaction

The electrostatic force acting between particles and the substrate in a fluid medium, F_{eps}, is given by[114]

$$F_{eps} = -2\mathrm{n}\pi r\varepsilon\kappa \frac{\left[\phi_1^2 + \phi_2^2 - 2\phi_1\phi_2 \exp(\kappa z)\right]}{\left[\exp(2\kappa z) - 1\right]} \tag{4.5}$$

where ε is the fluid permittivity, κ is the reciprocal of Debye length, ϕ_1 is the surface potential for particles, and ϕ_2 is the surface potential for the substrate. The electrostatic force acting among particles in a fluid medium, F_{epp}, is given by[123]

$$F_{epp} = -\frac{\varepsilon r\phi_1^2}{4} \frac{2\kappa \exp(\kappa z)}{\exp(2\kappa z) + 1} \tag{4.6}$$

Note that both particle-substrate and particle-particle electrostatic forces are repulsive.

4.3.3. Forces acting on particles parallel to substrate

The particle motion near a CL is a result of the interplay between various interaction forces as depicted in Fig. 4.1a. For example, the surface tension force acting on the particles near the CL tends to move them away from the CL, whereas the static friction force, to a certain extent, keeps particles stationary. The total attractive force, F_a, acting between particles and the substrate can be calculated by summing up the van der Waals, electrostatic, and net gravitational forces[117]

$$F_a = F_{wps} + F_{eps} + F_g \tag{4.7}$$

For neutrally buoyant particles, the net gravitational force, F_g, can be neglected. The total attractive force, F_a, induces a static friction force that prevents particles from moving parallel to the substrate away from the CL. The static friction force, fF_a, can be calculated by estimating the friction coefficient, f, based on the ratio of the drag force, F_d, to the attractive force, where the drag force acting on the particles is given by[117]

$$F_d = 6\pi r \eta v \tag{4.8}$$

Here η is the dynamic viscosity of the fluid and v is the velocity of the evaporative flow. In addition, particles near the liquid-vapor interface experience a surface tension force, F_s, given by[117]

$$F_s = 2\pi r \sigma \cos\theta \tag{4.9}$$

where σ is the surface tension of the liquid-vapor interface.

4.3.4. Estimation of forces acting on polystyrene particles in an aqueous colloidal drop on glass

Now, we estimate the van der Waals, electrostatic, surface tension, and drag forces acting on polystyrene particles in an aqueous evaporating colloidal drop on a glass substrate. Values of all constants used in the force calculations are listed in Table 4.1 and the resulting forces are listed in Table 4.2. For a substrate with a contact angle of 30°, our estimation suggests that it requires about 101 particles to pin themselves near the CL regardless of the particle radius. Note that, the forces acting among particles are in different directions and much weaker compared to particle-substrate interactions, and are therefore neglected in our estimation. Figure 4.1b shows the number of particles required

to pin themselves as a function of the contact angle. As the horizontal component of surface tension force, $F_s \cos\theta$, decreases with the increase in contact angle, less particles are required to overcome the surface tension force and pin themselves near the CL. In addition, both friction and surface tension forces depend upon the radius of the particle, and hence their ratio remains roughly the same regardless of the particle radius. However, for micro and nanoparticles of the same volume fraction, because the total number of nanoparticles is much larger than that of microparticles, nanoparticles can get closer to the CL and facilitate CL pinning much easier than their microparticle counterparts.

Table 4.1. Parameters used in force calculations of aqueous polystyrene suspensions depositing on glass.

Symbol	Physical Parameter	Value	Unit
A_{123}	Hamaker constant between polystyrene particle and glass in water	3×10^{-20} **114**	J
A_{131}	Hamaker constant between polystyrene particles in water	1×10^{-20} **124**	J
σ	Surface tension of water	0.072	N/m
Z	Minimum separation distance	0.4×10^{-9} **114**	m
ε	Permittivity of water	7×10^{-10}	Fm^{-1}
ϕ_1	Surface potential of polystyrene	15 **114**	mV
ϕ_2	Surface potential of glass	- 40 **114**	mV
η	Dynamic viscosity of water	0.9	cP
V	Velocity of water in evaporating drop	0.2	m/s
κ	Reciprocal of Debye length	$(430\times10^{-9})^{-1}$ **114**	m^{-1}

Table 4.2. Interaction forces acting on particles in an aqueous colloidal drop containing polystyrene particles on glass.

Name	For $r = 550\times10^{-9}$ m	For $r = 50\times10^{-9}$ m
F_{wps}	1.72×10^{-8} N	1.55×10^{-9} N
F_{wpp}	2.87×10^{-9} N	2.6×10^{-10} N
F_{eps}	-6.4×10^{-9} N	-5.81×10^{-10} N
F_{epp}	-5.04×10^{-14} N	-4.58×10^{-15} N
F_a	1.08×10^{-8} N	9.7×10^{-10} N
F_d	1.85×10^{-9} N	1.68×10^{-10} N
Friction coefficient $f = \frac{F_d}{F_a}$	0.17	0.17
Friction force, fF_a	1.85×10^{-9} N	1.68×10^{-10} N
F_s (θ=30°)	2.15×10^{-7} N	1.96×10^{-8} N
Number of particles required to pin, $n = \frac{F_s \cos\theta}{fF_a}$	101	101

4.4. Results and discussion

Particle deposition morphology of colloidal drops depends strongly upon substrate wettability [30], which changes the interplay between surface tension, drag, electrostatic, and van der Waals forces acting on both the micro and nanoparticles in an evaporating colloidal drop. Figure 4.2 shows the particle separation distance between the outermost micro and nanoparticles for four different substrates with the static receding contact angle, θ_{RCA}, ranging from 0 to 85°. It is shown that the particle separation increases significantly as the contact angle decreases.

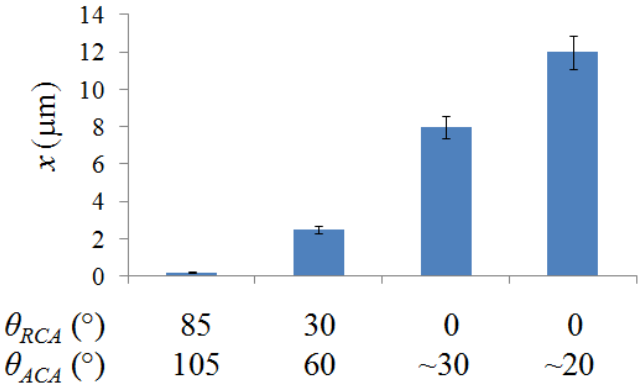

Figure 4.2. Final separation distance between outermost micro and nanoparticles (x) as a function of substrate wettability indicated by static advancing (θ_{ACA}) and static receding (θ_{RCA}) contact angles. In columns three and four, θ_{ACA} decreases while θ_{RCA} remains 0°.

The contact line radii as a function of time for an evaporating drop on substrates of $\theta_{RCA} = 80°$, 55°, 30°, 10°, and 0° are shown in Fig. 4.3. With the increase in substrate wettability, the drop evaporation time decreases and the constant contact area stage becomes increasingly dominant. For the cases of $\theta_{RCA} = 0°$ and 10°, the drops remain pinned during the entire evaporation process. Distinct three-mode evaporation, i.e., the constant contact area, constant contact angle, and mixed modes, is observed for $\theta_{RCA} = 30°$. For the cases of $\theta_{RCA} = 55°$ and 80°, the constant contact angle mode dominates drop evaporation. Different microflow patterns inside an evaporating drop for each of the three evaporation modes significantly influence the deposition morphology of bi-dispersed particles. Here, we describe particle separation in three distinct groups based

on the receding contact angle of the substrate, from well mixed, to partially separated, and finally to completely separated as θ_{RCA} decreases.

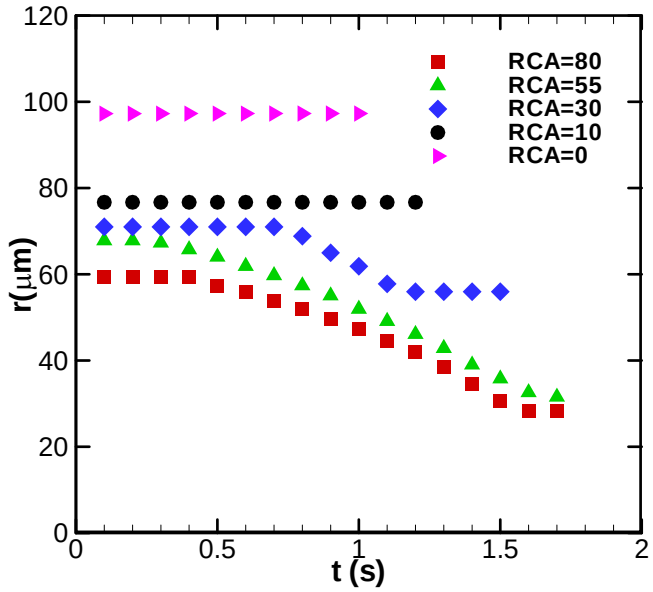

Figure 4.3. Contact line radius versus time for evaporating drops on substrates of different wettabilities. Colloidal suspension was formed from 0.1 and 1.1 μm polystyrene beads with particle volume fraction of 0.5% each in water and drop diameter before impact on glass substrates 80 μm.

The scaled radial positions of micro particles versus time in an evaporating drop on substrates of θ_{RCA}=55° and 10° are shown in Fig. 4.4. Four representative microparticles initially located at 25%, 50%, 75%, and ~100% (outmost microparticles) of the initial drop contact line radius r_{CL_0} are selected. For the case of $\theta_{RCA} = 55°$ where the constant contact angle mode dominates the drop evaporation process, the particles inside the drop move only slightly towards the contact line until being collected as the CL recedes (Fig. 4a). Whereas, for the case of $\theta_{RCA} = 10°$, the CL remains pinned during the entire evaporation process. Microparticles inside the drop move towards the pinned CL due to evaporatively driven flow whereas microparticles very close to the drop edge

move slightly inward under the surface tension of the water-air interface as nanoparticles pinned the contact line.

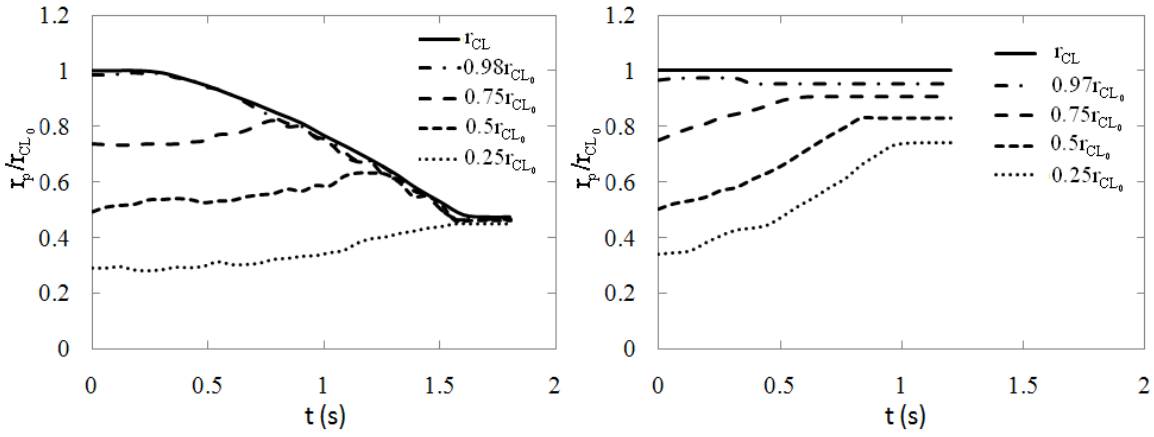

(a) (b)

Figure 4.4. Scaled radial position of micro particles versus time in an evaporating drop on substrates of different wettabilities. (a) $\theta_{RCA} = 55°$ and (b) $\theta_{RCA} = 10°$.

In the following, we describe the particle separation of bi-dispersed particles in three distinct groups based on the receding contact angle of the substrate, from mixed, to partially separated, and finally to completely separated as θ_{RCA} decreases.

4.4.1. $\theta_{RCA} > 45°$ (mixed)

For substrates with a receding contact angle higher than 45°, the first two stages of evaporation are clearly observed, as shown in side-view snapshots in Figs. 4.5a and 4.5c for the cases of θ_{RCA} =80° and θ_{RCA} =55°, respectively. In general, the higher the receding contact angle, the smaller footprint the particles deposit on the substrate. In the constant contact area stage of evaporation, colloidal particles are advected to the pinned

CL due to the evaporatively-driven flow. Once the contact angle, θ, reaches the static receding contact angle, θ_{RCA}, the CL starts receding. At the constant contact angle stage, evaporation occurs uniformly along the liquid-vapor interface and the contact area of the drop decreases linearly with time[30]. Lack of particle motion towards the CL at this stage prevents particles from accumulating near the CL to a level required for them to pin (shown in Fig. 4.1b). Micro and nanoparticles accumulate near the receding liquid-vapor interface and remain mixed as shown in Fig. 4.5e. Eventually when enough rows of particles assemble near the CL, the friction force acting on the particles overcomes the surface tension force. Particles are then pinned near the CL to facilitate CL pinning, and hence the mixed mode of evaporation is reached. However, as most of the carrier liquid has already evaporated in the first two stages, the remaining liquid does not allow particles to separate according to their sizes. This mixed deposition of micro and nanoparticles can be seen in the top-view image of the final deposit obtained by scanning electron microscopy (Fig. 4.6a) and the bottom-view image using fluorescence microscopy (Fig. 4.6b). As the constant contact angle mode dominates the entire evaporation process for the case of a large receding contact angle, the mixed mode of evaporation is very short as shown in Figs. 4.5a (side view) and 4.5b (bottom view). As the wettability of the substrate increases from $\theta_{RCA} = 80°$ to $\theta_{RCA} = 55°$, no observable changes are detected from the side-view images after $\theta < 5°$ (after t = 1.3s in Fig. 4.5c) due to film evaporation at the very late stage of evaporation[125], where the bottom-view images of drop evaporation reveal assembly of particles until the water is completely dried. A contour map indicating the number density of 1.1 μm particles is shown in Fig. 4.6c, obtained by averaging scanning electronic microscopy images of three bi-dispersed

deposition on a glass substrate of $\theta_{RCA} = 80°$. As it can be observed from the figure, microparticles are distributed all across the deposited drop. Although the other part of the solid deposit is occupied by nanoparticles that are difficult to visualize individually, from the microparticle number density map, we conclude that the bi-dispersed particles are well mixed in the deposit.

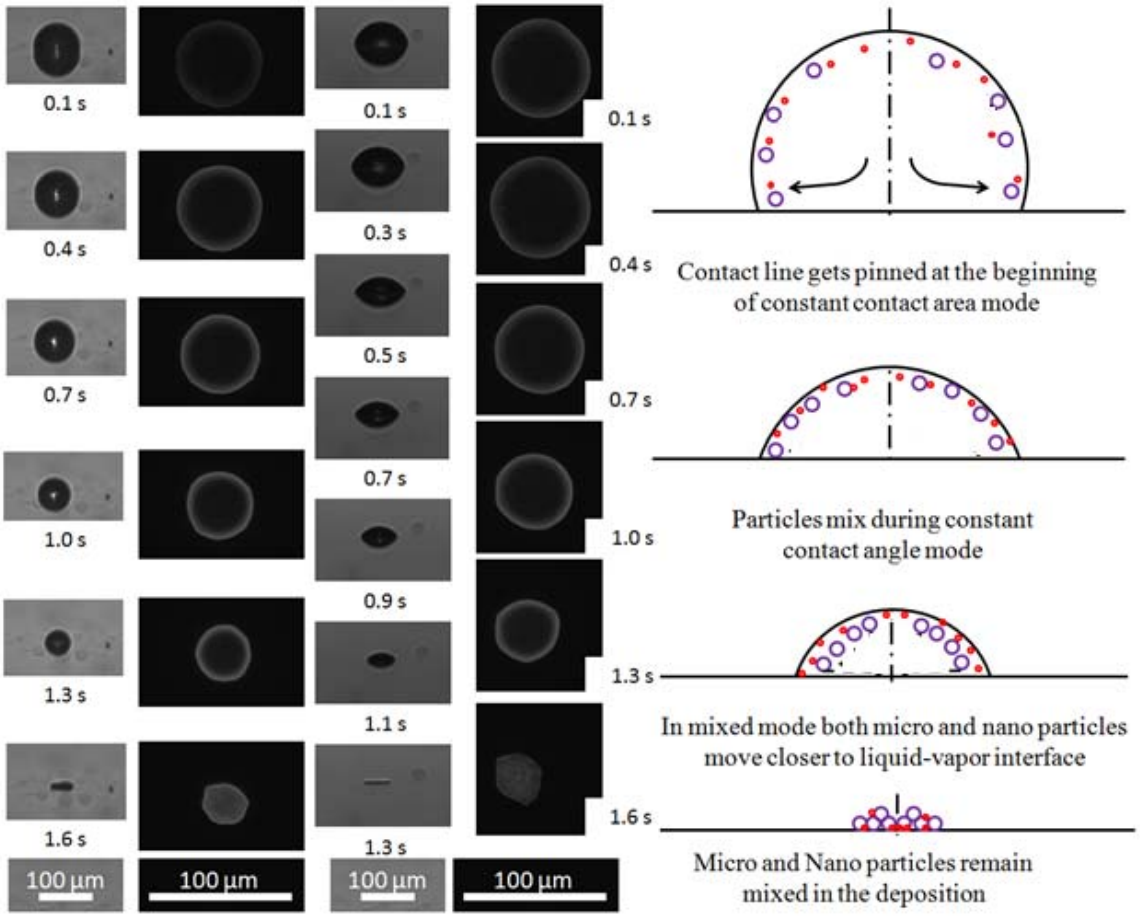

Figure 4.5. Deposition dynamics of bi-dispersed particles from an evaporating colloidal drop on a glass substrate of $\theta_{RCA} > 45°$. (a) Snapshots from side view and (b) snapshots from bottom view on a glass substrate of $\theta_{RCA} = 80°$. (c) Snapshots from side view and (d) snapshots from bottom view on a glass substrate of $\theta_{RCA} = 55°$. (e) schematic of the

evaporation process. Colloidal suspension was formed from 0.1 and 1.1 µm polystyrene beads with particle volume fraction of 0.5% each in water and drop diameter before impact was 80 µm.

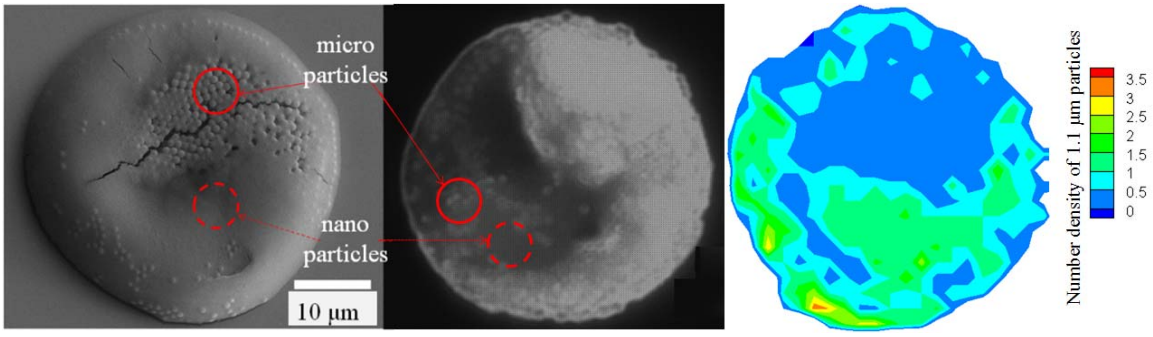

(a) (b) (c)

Figure 4.6. Deposition morphology of bi-dispersed particles on a glass substrate of $\theta_{\mathrm{RCA}} = 80°$. (a) SEM image (top view) and (b) fluorescence microscopy image (bottom view). Patches containing micro and nanoparticles are indicated by solid and dashed circles respectively. (c) Average number density of microparticles inside three deposited drops (based on top-view SEM images). Colloidal solution was formed from 0.1 and 1.1 µm polystyrene beads with particle volume fraction of 0.5% each in water and drop diameter before impact was 80 µm.

4.4.2. $0° < \theta_{RCA} < 45°$ (partially separated)

For a substrate of $0° < \theta_{\mathrm{RCA}} < 45°$, depending upon the interplay between the surface tension and friction forces acting on the particles, either all three stages or only the first stage of evaporation can be observed. In the case of $\theta_{\mathrm{RCA}} = 30°$ as shown in Figs. 4.7a and 4.7b, where $F_s \cos\theta > fF_a$, all three stages of evaporation are observed. However, for $\theta_{\mathrm{RCA}} = 10°$ shown in Figs. 4.7c and 4.7d, where $F_s \cos\theta < fF_a$, only the constant contact area mode can be observed. After the drop reaches its maximum diameter (usually within 100 ms), the CL pins due to heterogeneities on the substrate. Due to a higher evaporation rate near the CL, particles are advected near the CL region

and enhances CL pinning[37]. However, as shown in Fig. 4.1b, as the contact angle decreases during the constant contact area stage of evaporation, a higher number of particles (~100 rows) is required near the CL to maintain particle pinning. Two subsequent scenarios occur. If particles cannot form enough number of rows to pin, the CL begins to recede once the dynamic contact angle reaches θ_{RCA}. During the constant contact angle stage, the drop evaporates uniformly along the liquid-vapor interface and the surface tension force acting on the particles at the receding liquid-vapor interface pull the particles along with it. The interplay of surface tension and friction forces depins particles near the CL. During the mixed mode of evaporation shown in Fig. 4.7a, as the contact angle decreases with time, more particles are required to overcome the surface tension force to maintain particle pinning. Particles keep moving inward until they accumulate to the minimum number required to pin at about 1.3 s as shown in Fig. 4.7b. However, if the number of particles in the CL region is larger than that is required for particle pinning to occur at all time, particles near the CL will remain pinned as shown in Figs. 4.7c and 4.7d. This further facilitates contact line pinning and for this scenario, the contact angle continuously decreases until it reaches 0°. In both scenarios (Figs. 4.7a and 4.7b versus Figs. 4.7c and 4.7d), no observable changes is detected from the side-view images after $\theta < 5°$ (i.e., after $t = 1.1$ s and $t = 0.9$ s in Figs. 4.7a and 4.7c, respectively) due to film evaporation at the very late stage[125], where the bottom-view images of evaporation reveal assembly of particles until the water is completely dried.

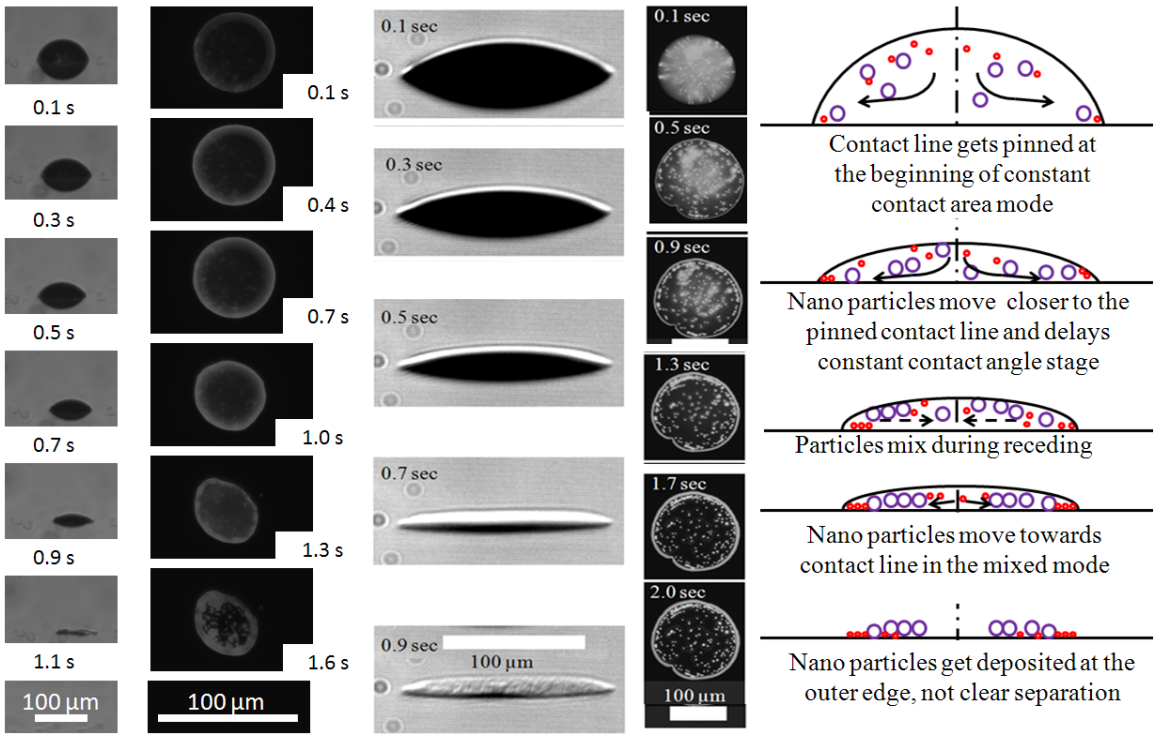

(a) (b) (c) (d) (e)

Figure 4.7. Deposition dynamics of bi-dispersed particles on a glass substrate of $0 < \theta_{RCA} < 45°$. (a) Snapshots from side view and (b) snapshots from bottom view on a glass substrate of $\theta_{RCA} = 30°$. (c) Snapshots from side view and (d) snapshots from bottom view on a glass substrate of $\theta_{RCA} = 10°$. (e) Schematic of the evaporation process. Colloidal solution was formed from 0.1 and 1.1 µm polystyrene beads with particle volume fraction of 0.5% each in water and drop diameter before impact was 80 µm.

As shown in Figs. 4.7c and 4.7d, when the CL is pinned, the CL wedge restricts the movement of microparticles closer to the edge of the drop compared to their nano-sized counterparts. As nanoparticles are 1000 times more in number compared to microparticles of the same volume fraction, more nanoparticles reach to the CL region and enhance CL pinning. As the constant contact area mode is prolonged for this case, enough microparticles quickly assemble near the CL to pin themselves. However, for

both cases of $\theta_{\mathrm{RCA}} = 30°$ and $\theta_{\mathrm{RCA}} = 10°$, particle separation near the CL is incomplete in the final deposition, where, from outermost to the center of the drop, is a region contains only nanoparticles, a region where micro and nanoparticles overlapped, and an inner ring consists of only microparticles. The interplay of surface tension and friction forces acting on particles determines the width of the middle region where micro and nanoparticles overlap. Particle separation improves when the width of this mixed region decreases at a low θ_{RCA}, where the friction force overcomes the surface tension force.

4.4.3. $\underline{\theta_{RCA} = 0°}$ (completely separated)

For a hydrophilic substrate of $\theta_{\mathrm{RCA}} = 0$, the drop CL remains pinned during the entire evaporation and only the drop contact angle decreases with time as shown in Fig. 4.8a. The liquid-vapor interface forms a wedge like shape near the pinned CL and particles are advected towards the CL due to a higher evaporative flux there[37]. As the friction force increases due to continuous accumulation of nanoparticles near the CL, it overcomes the surface tension force acting on these particles resulting in pinning of nanoparticles along the CL. The bottom-view images in Fig. 4.8b show the assembly of nanoparticles in more than a hundred rows along the CL, preventing drop from receding. A strong evaporative flow advects microparticles towards the pinned CL and due to the large momentum of these particles; some of them protrude through the liquid-vapor interface. This reduces the surface tension force acting on protruded microparticles compared with the value determined by Eq. (4.9), such that surface tension force cannot overcome the friction force to move the particles radially inward. After 0.5 s, no change can be observed from the drop side-view images in Fig. 4.8a but the inward movement of

microparticles can be seen in bottom-view images (Fig. 4.8b) until the drop is completely dried at 0.9 s. For a very hydrophilic substrate, microparticles cannot reach the minimum number of rows required to pin, and hence the surface tension acting on microparticles drives most of them moving radially inward to the center of the drop as shown in Fig. 4.8b. In the meantime, some microparticles do not move radially inward suggesting that they protrude through the liquid-vapor interface as indicated by arrows in Fig. 4.8b.

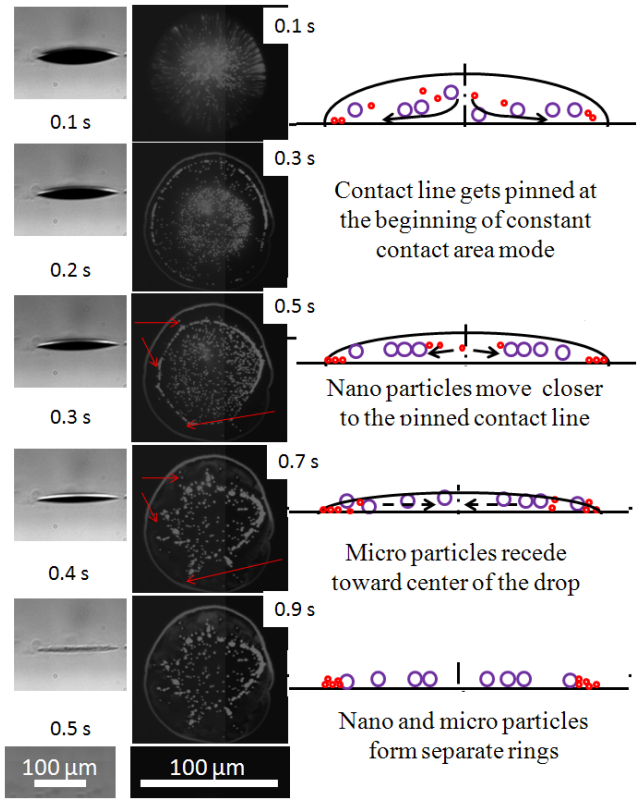

Figure 4.8. Deposition dynamics of bi-dispersed particles on a glass substrates of $\theta_{RCA} = 0°$. (a) Snapshots from side view and (b) snapshots from bottom view (particles marked by arrows do not recede inward after 0.5 s suggesting they that protrude through the liquid-vapor interface). (c) Schematic of the evaporation process. Colloidal solution was formed from 0.1 and 1.1 µm polystyrene beads with particle volume fraction of 0.5% each in water and drop diameter before impact was 80 µm.

Similar to Perelaer et al.[9] and Biswas et al.[113] that used simple trigonometry based on the CL wedge assumption to estimate the distance of the outermost particles from the CL for an inkjet-printed mono-dispersed colloidal drop, the separation distance x of the outermost micro and nanoparticles can be calculated by

$$x_{\text{theoretical}} = \frac{(r_1 - r_2)}{\tan\left(\frac{\theta}{2}\right)} \tag{4.10}$$

where r_1 and r_2 are 550 and 50 nm respectively. Figure 4.9 shows the theoretically estimated and experimentally measured separation distances as a function of time. As the drop spreads to a larger area on a hydrophilic substrate, surface irregularities reduce the drop circularity and lead to large experimental variations (~12%) in the final deposition morphology. However, it can be observed that, for the entire evaporation process, the measured separation distance is smaller than that suggested by the CL wedge assumption; this discrepancy indicates that some micro-sized particles protrude through the liquid-vapor interface and shorten the separation distance.

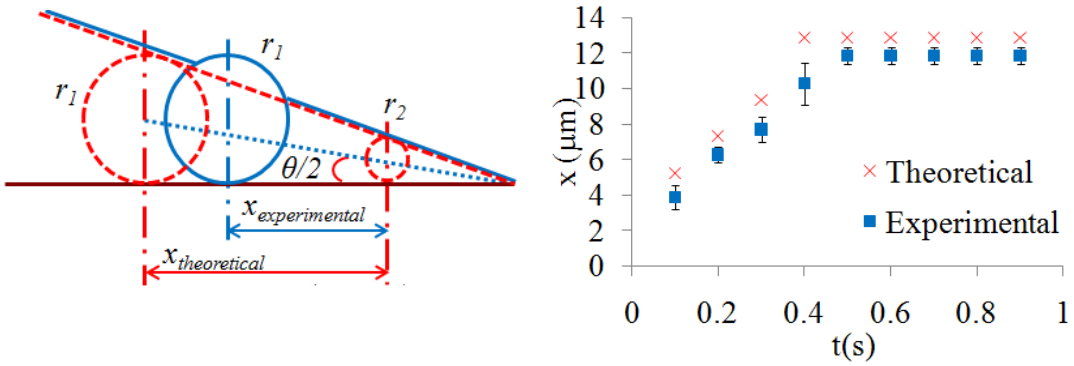

(a) (b)

Figure 4.9. Comparison of theoretically and experimentally-determined particle separation distances of outermost micro and nanoparticles on a substrate of $\theta_{RCA} = 0°$. (a) Schematic of the wedge assumption and micro-sized particle penetrating liquid-vapor interface and (b) theoretical and experimental particle separation distances as a function of time where experimental separation distance is obtained based on three separate experiments and error bars devote the standard deviation.

4.5. Conclusions

The deposition behavior of an inkjet-printed aqueous colloidal drop consisting of bi-dispersed micro and nanoparticles has been investigated using fluorescence microscopy for glass substrates of varying wettability. The values of surface tension, electrostatic, drag, and van der Waals forces acting on particles near the CL have been estimated. The results show that, the drop evaporation dynamics on substrates with θ_{RCA} from 85° to 0° show significant differences in duration of three evaporation modes and the corresponding microflow patterns inside the drop result in different particle dynamics and deposition morphologies of bi-dispersed colloidal drops. For a hydrophilic substrate of $0° < \theta_{RCA} < 45°$, particle separation is incomplete in the final deposition. Three separate regions exist from outermost to the center of the drop including a region with only nanoparticles, a mixture of micro and nanoparticles, and an inner region with only

microparticles. The width of the middle region where micro and nanoparticles overlap depends upon the interplay of the surface tension and friction forces acting on the particles. For a hydrophilic substrate of $\theta_{RCA} = 0$, nanoparticles accumulate at the CL forming a large number of rows (>~100) that prevent CL from receding. This enhanced pinning by nanoparticles permits radially outward evaporative flow toward the pinned CL and pushes some of the microparticles to protrude through the liquid-vapor interface. Reduced surface tension acting on those protruded microparticles prevent them from moving inward, whereas most other microparticles move radially inward to the center of the drop at the late stage of evaporation when enough number of particles required to pin is reached. By modifying substrate wettability, the surface tension force acting on the particles is tuned. The control of particle separation according to their sizes can therefore be achieved.

We have also found that the increase in size ratio of the bi-dispersed particles will improve the particle separation for the cases with the same particle volume fraction and substrate wettability. As the number of particles affects CL pinning, the boundaries between mixed, partially separated, and separated regions increase for a higher particle loading. The relative humidity of the environment also influences the separation distance of bi-dispersed particles. As reported in our earlier paper[125], a lower relative humidity (higher evaporation rate) will result in a higher contact angle. This leads to poor particle separation as compared to drop evaporating in a high humidity environment. Hence, by controlling the substrate wettabiliy, particle size ratio, particle loading, and relative humidity, the deposition morphology of bi-dispersed particles can be controlled.

Chapter 5 : EFFECT OF DROP COALESCENCE ON DEPOSITION MORPHOLOGY

5.1. Introduction

Deposition of individual colloidal drops has been studied in reasonable details as reviewed in previous chapters. However, applications of inkjet-printed single drops are limited. Drops are often used as building blocks for line and pattern printing where the interaction between drops plays an important role in determining the morphology and properties of deposited functional materials.

A number of studies have been carried out to examine the dynamics of sessile drop coalescence by putting two drops of pure liquid in contact with each other by pumping liquid into either of the drops[126, 127], by sliding one of the drops[128, 129], or by condensation driven drop growth[130]. The dynamics of time-dependent width of the meniscus bridge between the two merging droplets[126, 127, 131], perimeter[130] and shape[132] of the merged drop have been studied as a function of the liquid viscosity, surface tension, and density as well as substrate wettability. It was found that the merged drop slowly relaxes to a spherical cap where the characteristic relaxation time is proportional to the drop radius of the final equilibrium. This relaxation time is nearly 10^7 times larger than the bulk capillary relaxation time due to the strong dissipation of the moving contact line.

Castrejon-Pita et al.[133] observed the impact and coalescence of glycerol/water drops (2.4 mm in diameter) on a solid surface using high-speed particle image velocimetry and a droplet generator. The distance between a prior deposited sessile drop and an impacting drop was varied from no offset between two drops to completely separated. In the case of no offset between drops, axisymmetric impact and spreading are observed and the resulting merged drop remains a spherical cap. As the distance between

two drops increases to 40% of the initial drop diameter (but still below the sum of the initial drop radius and the impacting drop in-flight radius), the impacting drop lands on a pre-wetted substrate and the resulting merged drop exhibits a circular footprint. When the distance between drops is larger than the sum of the initial drop radius and the impacting drop in-flight radius, the impacting drop lands on a dry surface and two drops coalesce after the initial impact (including the kinematic, spreading and relaxation phases[35]) and wetting stages. Spreading of the second drop pushes liquid to the first drop under surface tension resulting in a smaller radius as compared to the original drop shown for the separation distances of 1.3 and 2.0mm in Figure 5.1.

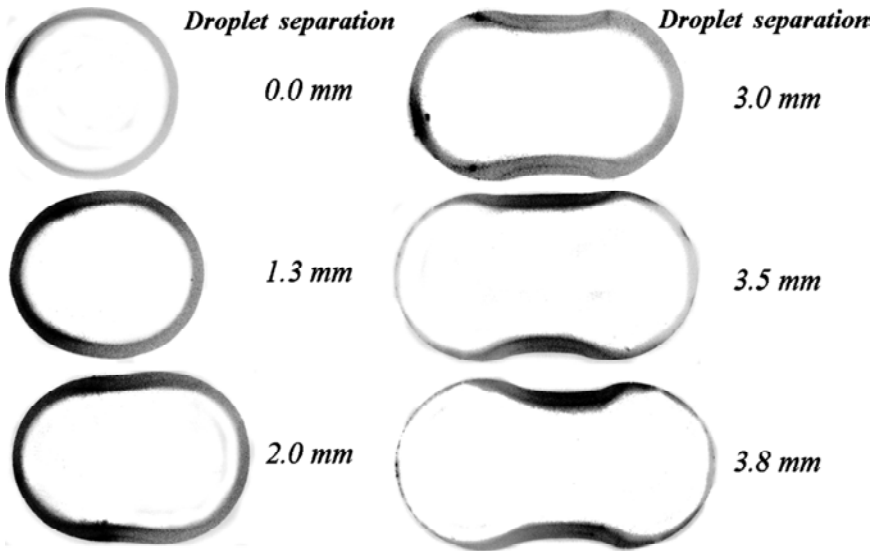

Figure 5.1. Footprints of drop coalescence for various droplet spacings. These images were taken 0.6 s after the first contact of the droplets[133].

The discussion up to now is based on pure liquid drops and the effect of evaporation on the interaction of drops is neglected. Deposition morphology of inkjet-

printed solution or suspension into line patterns has also been studied. For example, Duineveld[45] recently studied the stability of inkjet-printed lines consisting of PEDOT:PSS, a conducting polymer, using a single-nozzle drop-on-demand inkjet printing system. It was shown that the printed line becomes unstable when its contact angle is larger than the static advancing contact angle. Stringer and Derby[54] concluded that the stable line width of a printed line is bounded by two limits: the minimum line width determined by the maximum drop spacing for stable coalescence and the upper bound determined by the minimum drop spacing below which a bulging instability occurs. Based on these analyses, appropriate printing parameters and ink/substrate properties can be selected to warrant optimal deposition morphology.

Andrieu et al.[130] suggested that the rate of relaxation of slightly deformed drop to a spherical cap can be distinguished into three characteristic time scale: the inviscid inertial time ($t_e \sim$ μs), viscous inertial time ($t_i \sim$ ms) and capillary relaxation time ($t_b \sim$ μs). The inviscid inertial time, $t_e = \left(\frac{\rho R^3}{\sigma}\right)^{1/2}$ accounts for the slowing down of the relaxation by the inertia of the liquid. The viscous inertial time, $t_i = \frac{\rho R^2}{\eta}$, accounts for the dissipation in the boundary layer. The capillary relaxation time, $t_b = \frac{R\eta}{\sigma}$, is driven by the surface tension. All three time scales are much smaller than the evaporative time scale (on the order of a second) and comparable to or smaller than the steady state diffusion time (~ ms), $t_d = \frac{4R^2}{D}$. The dynamics of drop coalescence is therefore controlled by the receding motion of the contact line driven by evaporation, the slowest process. This

dissipation due to the gas-liquid phase transition near the contact line introduces a very small $K \sim 10^{-8}$ Arrhenius factor in the relation between the driving force and the contact line velocity.

In this chapter, the interaction between two inkjet-printed evaporating colloidal drops is systematically studied as a function of their temporal delay and spatial spacing upon impact. The dynamics of drop coalescence and resulting particle deposition morphology are examined as the interplay between evaporation of the first drop, impact and wetting of the second drop, and relaxation, microflows, and evaporation of the merged drop.

5.2. Experimental details

A colloidal mixture of carboxylate-modified polystyrene fluorescent beads of 1.1 μm diameter in DI-water, 0.2% by volume, was used in our inkjet printing experiments. Pico liter drops were generated using the inkjet printing setup described in section 4.2. Here, two drops with controlled temporal delay and spatial spacing are printed consecutively to observe interactions between them. The spacing between two interacting drops is varied by moving the microscope stage and the delay is created by jetting two drops at different frequency controlled by the JetDrive and a delay generator. The contact line dynamics, particle motion, and final deposition inside the merged colloidal drop were observed using an inverted fluorescence microscope with a 40× objective. The bottom-view images were captured by a Sony XCL-5005CR CCD camera at 10 frames per second. The ambient temperature and humidity were kept at 22 °C and 50 % relative humidity for all experiments.

5.3. Results and discussion

Figure 5.2 (a)-(c) shows evolution snapshots of two consecutively printed colloidal drops with a 0.9s delay time and short, medium, and long drop spacings, respectively. In addition to the evaporation-driven flow as observed in evaporation of single drops, the motion of the particles from the second drop to the first drop is observed for all three cases due to a gradient in capillary pressure as a result of different radii of curvature in two ends of the merged drop. Along with the change in drop spacing, the dynamic contact angle of the merged drop also changes, which results in different relaxation velocities along the perimeter of the merged drop. This difference in local relaxation velocity creates different radii of curvature in the merged drop. The resulting pressure imbalance pushes the liquid to flow from the second drop (smaller radius of curvature and hence higher pressure) to the first drop side (larger radius of curvature and hence lower pressure) and drags particles along with it. As the separation distance between two drops increases, the area and length of the deposition increase, but the particle number density in the second drop area of the deposit decreases. Particle concentration decreases in the deposit along the length of the major axis, defined as the axis passing through the centers of both drops, from the beginning of the first drop to the end of the second drop.

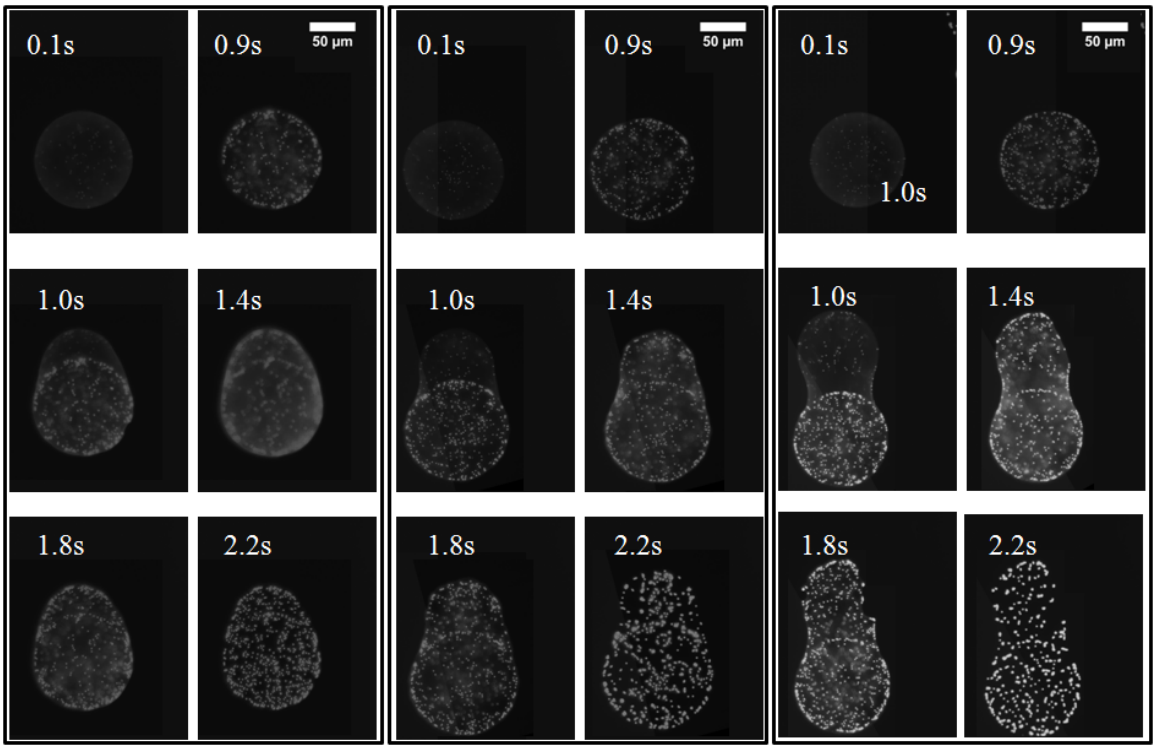

(a) (b) (c)

Figure 5.2. Snapshots of drop coalescence as drop spacing increases. (a) Short drop spacing (0.193 D_c) (b) medium drop spacing (0.453 D_c) and (c) long drop spacing (0.775 D_c). Drop spacing is defined as the distance between two consecutively printed drops and is scaled by using diameter of the first drop on the substrate (D_c).

Figure 5.3(a)-(c) shows evolution snapshots of two consecutively printed colloidal drops with the same separation distance of $0.7D_c$ (the diameter of the first drop) but with delay times of 0.2, 0.6, and 0.9s, respectively. As the delay between two drops increases, the effective total volume of the drop decreases due to increase in evaporation of the first drop. Evaporative flow gains higher velocities as evaporation progresses[134], resulting in enhanced pinning of particles near the contact line. Liquid from the second drop flows toward the pinned contact line of the first drop under a gradient in capillary pressure, carrying particles along with it. This additional flow from the second drop increases the

number of particles in the first drop making the particle density on the initial drop side of the deposit denser than the second drop side. It can also be seen from Figure 5.3 (c) that the coffee-ring deposition of the first drop is still present in the final deposition. The presence of the coffee ring from the first drop increases the non-uniformity of the deposit when compared with the cases of shorter delays.

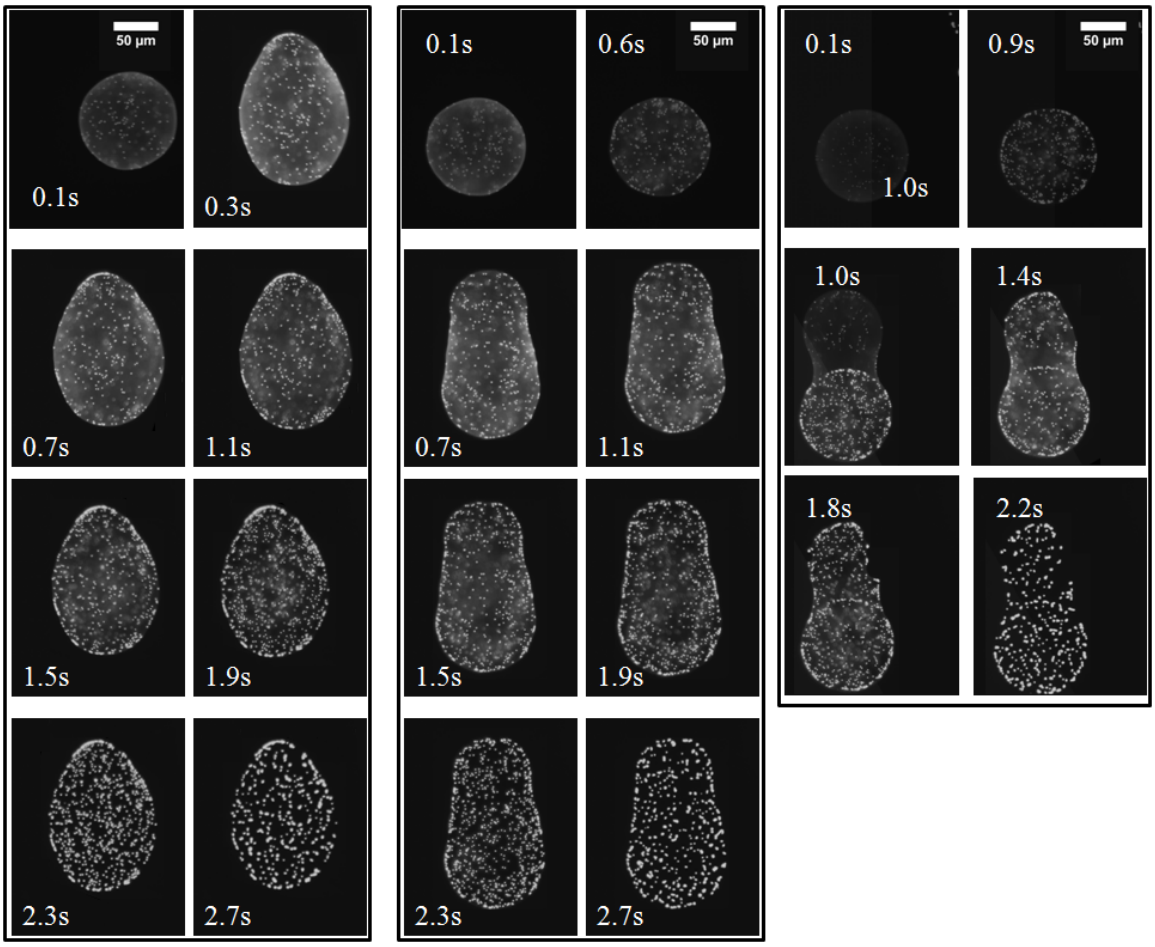

(a) (b) (c)

Figure 5.3. Snapshots of drop coalescence and particle deposition as temporal delay between consecutively printed drops increases. (a) 0.2s delay (b) 0.6s delay and (c) 0.9s delay. Spacing between two drops is kept constant at $0.7D_c$ where D_c is the diameter of the first drop on the substrate.

The scaled particle number density along the major axis of the deposit from two consecutively printed drops is plotted in Figure 5.4 for the cases with long drop spacing and delay times of 0.2, 0.6, and 0.9s. It can be observed for all three cases that the particle number density peaks at the two ends of the major axis of the deposit (i.e., scaled drop spacing D_s/D_c of 0.05 and around 1.3), implying that the coalesced drops exhibit the coffee-ring effect. Contrary to only two deposition peaks at both ends of the major axis and fairly uniform deposition in the center of a drop for the cases of small delays (0.2 and 0.6s). A third peak is observed for the case of a longer delay (0.9s). This peak in the middle of the deposit (D_s/D_c around 1.0) represents the presence of a coffee ring located at the original deposition site of the first drop Moreover, there are more particles at the peak of the initial drop side compared to the peak on the second drop side due to a capillary flow that pulls more particles to the first drop.

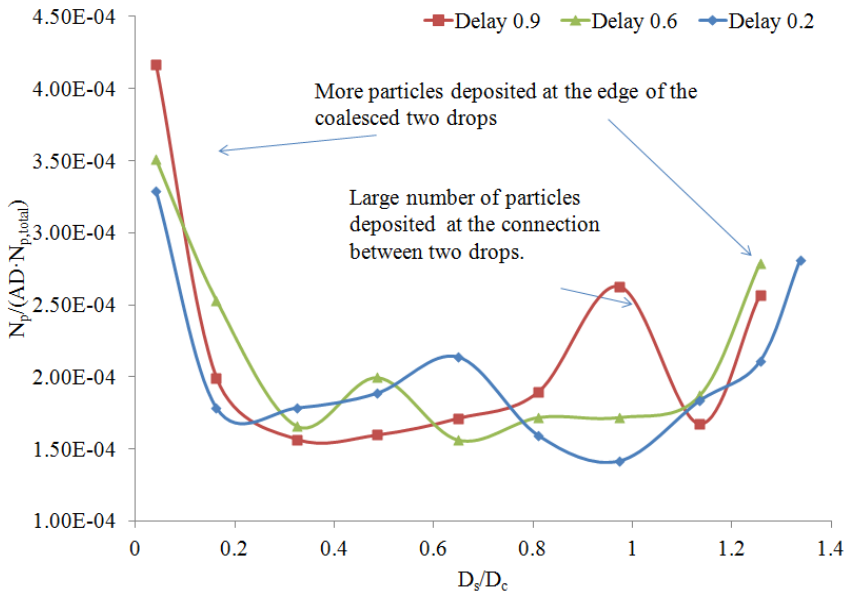

Figure 5.4. Scaled particle number density along the major axis of the deposition for the cases of long separation distance between drops. D_s is the spacing between two drops and D_c is the diameter of the first drop on the substrate.

Figure 5.5 shows the schematic of the drop coalescence of two consecutively printed colloidal drops and the consequent particle deposition process. After the impact of the first drop, the evaporative flow emerges toward the pinned contact line. Particles in the evaporating drop move toward the pinned contact line and further enhance contact line pinning. When the second drop impacts the first evaporating drop, it lands on the pre-wetted surface and spreads limitedly as much of the drop coalesces with the first evaporating drop. The liquid from the second drop flows toward the first drop under the pressure difference $\Delta P = P_f - P_b$ where P_b is the pressure in the first drop and P_f is the pressure in the impacting drop, carrying the particles along with it as shown in Figure 5.5 (b). This results in an asymmetric deposition as shown in Figure 5.5 (c)

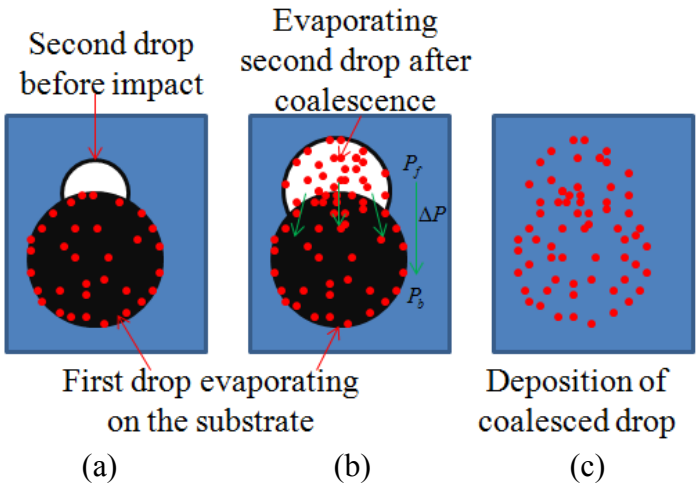

Figure 5.5. Schematic of deposition in coalesced drops. (a) Suspension drops before impact, (b) evaporation of coalesced drop and (c) deposition of the coalesced drop.

Scaled radius of curvature of the second drop upon impacting the pre-wetted surface along the major axis of the deposit from two consecutively printed drops is plotted in Figure 5.6 for various drop spacings and delay times. As shown in Figure 5.6 (a), the radius of curvature of the second drop, R, is measured by curve fitting and scaled by the radius of the first drop R_c. It is shown in Figure 5.6 (b) that, for the delay time of 0.2 s, the scaled radius of curvature decreases monotonically with the scaled drop spacing. This is because, for a short delay time, two drops completely coalesce and a larger drop spacing leads to a more elongated shape for the merged drop. For the cases of longer delay times (0.6 and 0.9s), the radius of curvature on the second drop side decreases first and then increases with the increase in drop spacing. This indicates an evidence of in-complete drop coalescence for large drop spacings when the carrier liquid is evaporated.

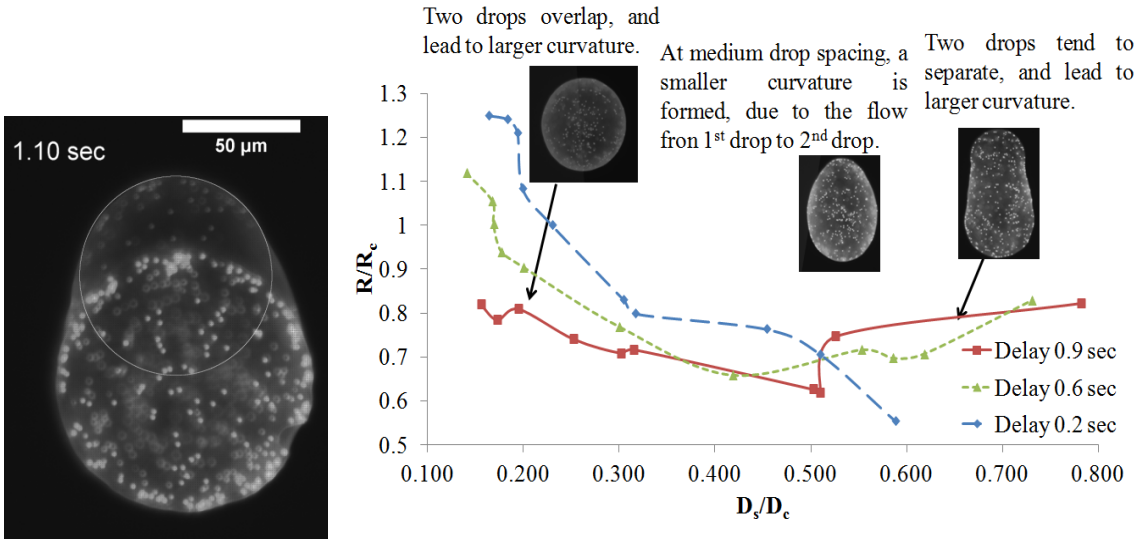

(a) (b)

Figure 5.6. Radius of curvature of the impacting drop as a function of drop spacing (a) Radius of curvature of the second drop and (b) radius of curvature when the spreading is complete. R_c is the radius of the drop-substrate contact arc, R is the radius of the curvature of the merged drop. D_s is the drop spacing and D_c is the diameter of the first drop.

As the drop spacing increases, the length of the major axis increases. This increase however does not necessarily translate into the increased radius of the merged drop. Figure 5.7 shows the circularity of the coalesced drop as a function of the drop spacing. It can be observed that, higher circularities are obtained for shorter delay times compared with those from a longer delay between ejected drops. In addition, larger drop spacing leads to poorer circularity due to elongation of coalesced drops.

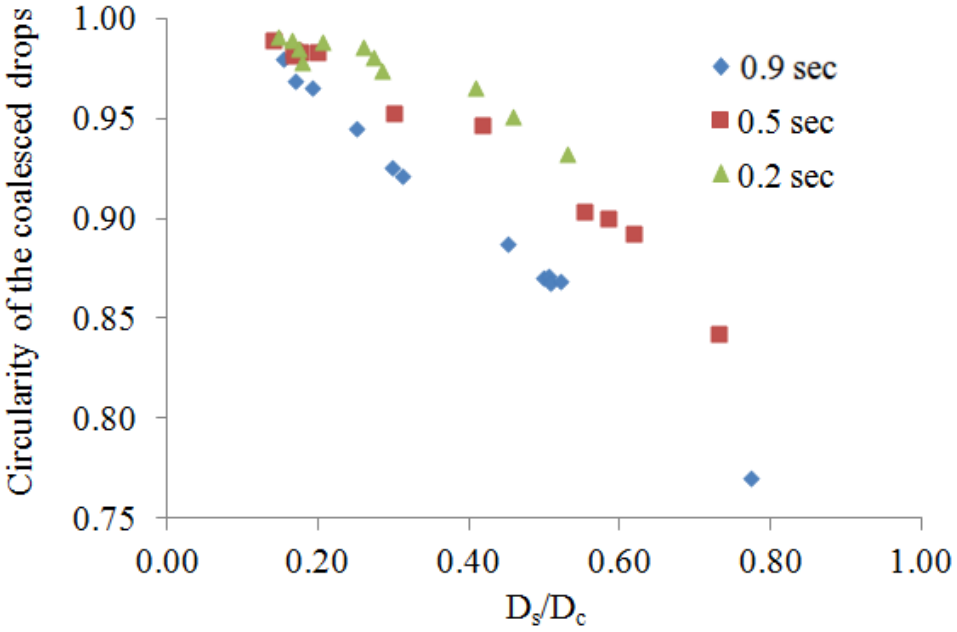

Figure 5.7. Circularity of the coalesced drop as a function of drop spacing. D_s is the drop spacing and D_c is the diameter of the first drop.

5.4. Conclusions

In this chapter, the dynamics of drop coalescence and particle deposition of two consecutively printed evaporating colloidal drops are observed in real time using a fluorescence microscope. The second droplet is printed on pre-wetted region of the first drop and the effects of both temporal delay and spatial spacing between two drops on final deposition morphology are examined. The results show that as the separation distance between two drops increases, the circularity of the coalesced drop decreases. Moreover, for the drops interacting with a longer temporal delay, a coffee ring has already established before the impact of the second drop. As the second drop impacts on the substrate and coalesces with the first drop, the capillary flow drives the carrier liquid and suspended particles in the second drop toward the first drop resulting in more

particles deposited on the first drop side. The particle number density along the major axis of the deposit shows two peaks at the two ends of the major axis for the cases with shorter delay times, but three peaks for a longer delay time with an additional peak located at the first coffee ring. For a short delay time, the scaled radius of curvature on the second drop side of the deposit decreases monotonically with the scaled drop spacing, but it decreases first and then increases with the increase in drop spacing for larger delay times. By tuning the interplay of drop spreading, evaporation, capillary relaxation, and particle assembly processes, the deposition morphology of two consecutively printed colloidal drops can hence be controlled. Moreover, it can be concluded that reduction of delay between drops (printing at higher frequency) can improve the uniformity of the printed lines.

Chapter 6 : EFFECT OF PARTICLE SHAPE ON DEPOSITION MORPHOLOGY

6.1. Introduction

Previous studies on particle deposition from evaporating colloidal drops have been focused on spherical particles[36-40, 125, 135, 136]. For the case of hydrophilic substrates, deposition morphology of a colloidal drop containing spherical particles exhibits a coffee-ring shape. This uneven distribution of particles is not suitable for line and film printing. Mixtures of solvents with different surface tensions and vapor pressures[40], as well as heating of the substrates[50], are used to suppress the coffee-ring effect for obtaining more uniform deposition.

Numerous studies have been conducted to address shape anisotropy of nano-objects at a fluid-fluid interface, including the assembly of ellipsoidal particles[42, 137], and the alignment of DNAs[138-140], nano-wires[141] and single walled carbon nanotubes[142]. In contrast to spherical particles (smaller than 5μm in diameter) that can penetrate and stick to the liquid-vapor interface without distorting the interface[143], a non-spherical particle must distort the liquid-vapor interface to maintain an equilibrium contact angle[137]. For the case of ellipsoidal particles, this distortion of the liquid-vapor interface attracts other ellipsoidal particles through strong, long range capillary attractions[43] forming branched aggregations at the liquid-vapor interface[144]. Once the ellipsoids are attracted to the liquid-vapor interface, they form loosely packed structures that prevent the motion of suspended particles toward the pinned contact line and thereby suppressing the coffee-ring effect[44].

In this chapter, the effect of particle shape on deposition morphology of inkjet-printed colloidal drops is studied. Different from a recent Nature article that focused on

the deposition of ellipsoids from a micro-liter drop[44], the typical volume of an inkjet-printed drop for functional material deposition is tens of pico-liter. Drops of that size evaporate on a time scale of several seconds and leave no more than a few seconds to form branched structures of ellipsoids at the liquid-vapor interface. It therefore becomes unclear whether those ellipsoidal particles have sufficient time to form branched structures. In addition, the Marangoni flow can become more pronounced in pico-liter drops. Its effect on ellipsoidal particle deposition is of interest as well.

6.2. Fabrication of ellipsoidal particles

Formation of ellipsoidal particles from spherical particles has been studied since 1991[145-147]. Keville et al.[145] pioneered the method by dispersing poly (methyl methacrylate) (PMMA) microspheres in a poly(dimethylsiloxane) (PDMS) matrix. The PDMS matrix was then heated to 175-180 °C such that the PMMA particles are above their glass transition temperature. The PDMS matrix was then stretched. After stretching, the matrix was cooled and dissolved to retrieve the PMMA microparticles of ellipsoidal shape. Ho et al.[146, 147] replaced PDMS with polyvinyl alcohol to stretch polystyrene particles. Different stretching ratios were applied to the PVA gel to get different aspect ratios of ellipsoidal particles.

In this study, the ellipsoidal particles are fabricated from hydrophilic spherical particles. Carboxylate-modified polystyrene particles of 1 μm diameter are dispersed in a 10% w/w solution of polyvinyl alcohol (PVA) gel in DI water. The gel is allowed to solidify with dispersed particles. The gel is then dipped into a heated oil bath at 140 °C. The gel is kept in the oil bath for 30 seconds and stretched to the desired aspect ratio. As

the gel is heated, the spherical particles inside the gel reach to their glass transition temperature (110 °C) and become soft. These soft particles are then deformed by stretching at this elevated temperature and particles become elongated in the direction of stretching. Schematic of the particle stretching process is shown in Fig. 6.1

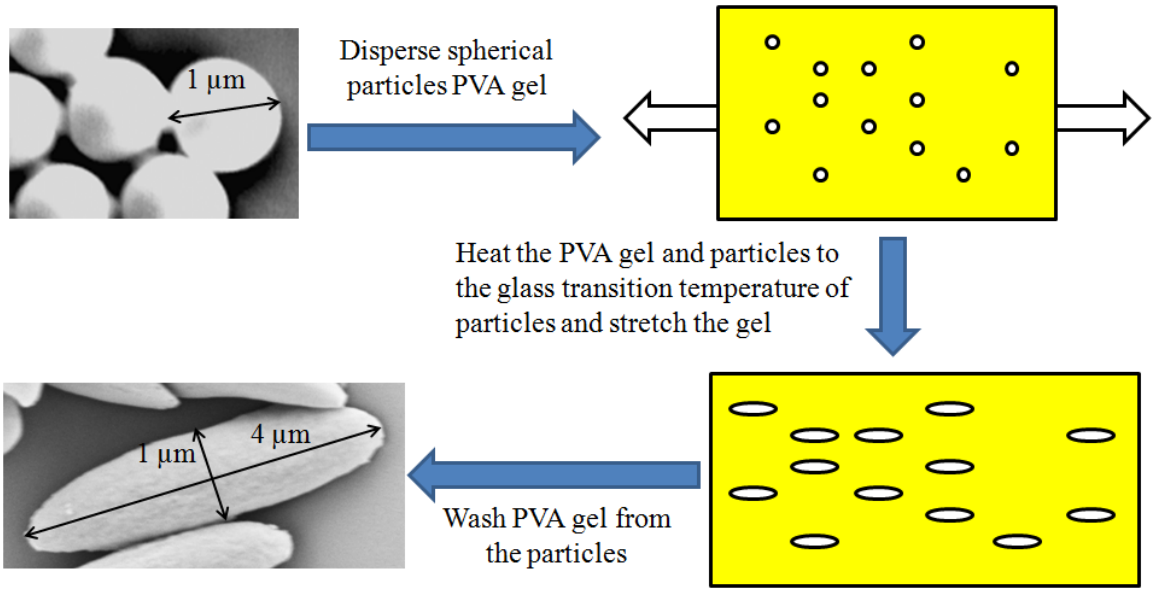

Figure 6.1. Schematic of ellipsoid particle fabrication from spherical particles.

After stretching, the gel is washed with acetone, ethanol, isopropanol and water multiple times to remove oil residues. The clean gel is submerged into a 1:1 solution of isopropanol and DI water. The processed suspension (ellipsoids, PVA gel, isopropanol and DI water) is then sonicated for six hours to dissolve the PVA gel in water. Once the PVA gel is dissolved, the suspension is put under a centrifuge to separate particles from the mixture of the dissolved PVA gel, isopropanol and water. The ellipsoidal particles are collected at the bottom of the centrifuge tube as their density is higher than water (density of polystyrene particles – 1.05 Kg/m^3 compared with density of water – 0.998 Kg/m^3).

These particles are then sonicated in DI water for two more hours to dissolve the PVA gel residue from the particles. Ten such washing cycles (sonicate-centrifuge) are needed to limit the PVA gel concentration to 0.01% w/w, after which the clean ellipsoidal particles are finally obtained. Suspension of ellipsoid particles is then sonicated for an hour before printing to remove possible aggregation of particles.

6.3. Experimental details

Ellipsoidal particles are printed using the same setup as described in section 4.2. However, major differences are in the preparation of the suspension. Here the suspension is dilute, 0.6% v/v; concentration of the suspension is limited due to the tendency of particle aggregation. To prevent clogging of the nozzle during printing, a nozzle of a larger (80 μm) diameter is used (MJ-AL-01-80). The drops are printed on glass substrates of three different wettabilities (θ_{RCA} = 85°, 20° and 0°). The ambient temperature and humidity were kept at 22 °C and 30 % relative humidity for all experiments.

6.4. Results and discussion

Deposition behavior of ellipsoidal particles from an inkjet-printed colloidal drop is captured in real time. In a dilute suspension, the contact line of the evaporating drop can recede due to surface tension[38]. However, on hydrophilic substrates, the movement of particles toward the drop center due to a receding contact line is limited, thus resulting in coffee ring deposition even for dilute suspensions[30, 135].

Figure 6.2 shows the comparison of bottom view images of colloidal drops consisting of spherical and ellipsoidal particles evaporating on a relative hydrophilic

glass substrate (θ_{RCA} = 20°) at 50% RH. As the colloidal drop containing spherical particles evaporates on a glass substrate, the spherical particles are carried toward the pinned contact line and hence enhance contact line pinning as shown in Figure 6.2 (a). Contrary to this movement of spherical particles toward the contact line, ellipsoidal particles do not move to the contact line allowing the contact line to recede during evaporation. It can be seen from Figure 6.2 (b) that up to 2.1 seconds into the evaporation (80% of the total evaporation duration), the ellipsoidal particles do not come near the glass substrate. The absence of particles near the contact line during evaporation does not enhance contact line pinning. This results in a receding contact line, which suppresses the coffee-ring effect as observed in spherical particle suspensions.

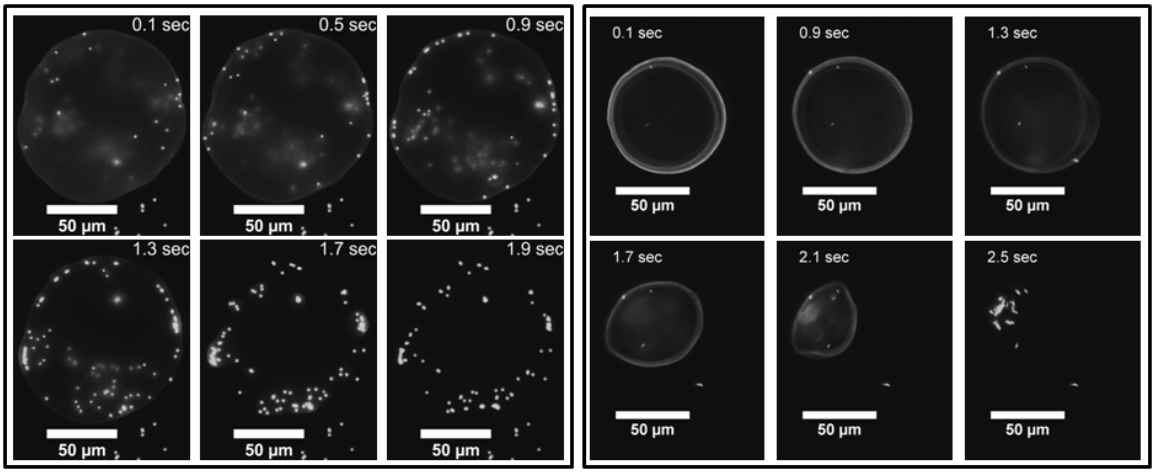

(a) (b)

Figures 6.2. Snapshots of evaporating colloidal drops consisting of (a) spherical particles (0.8% v/v) and (b) ellipsoidal particles (0.6% v/v). Colloidal drops are printed onto a clean glass substrate (θ_{RCA} = 20°) at RH = 50%. During evaporation, the contact line recedes and the coffee-ring effect is suppressed for the case of ellipsoid particles, in contrary to the case of spherical particles where the contact line remains pinned and a coffee ring is obtained.

Ellipsoidal particles have stronger capillary interactions among themselves compared to the spherical particles[43]. These higher capillary interactions result in higher attractions among particles near the liquid-vapor interface during evaporation. For the case of spherical particles, the particles move and deposit toward the pinned contact line due to the evaporative flow and result in a coffee-ring deposition as shown in Figure 6.3 (a). In contrast, ellipsoidal particles move toward the liquid-vapor interface by the same outward flow that causes the coffee-ring effect for spheres. Strong capillary attractions between the ellipsoidal particles results in the formation of loosely packed structures at the liquid-vapor interface. Such structures prevent ellipsoids from reaching the pinned contact line. Lack of particles near the contact line allows for the contact line to recede freely during the constant contact angle stage. More ellipsoidal particles are collected at the liquid-vapor interface with the shrinking drop and finally deposit uniformly onto the substrate, suppression the coffee-ring effect as observed for spheres.

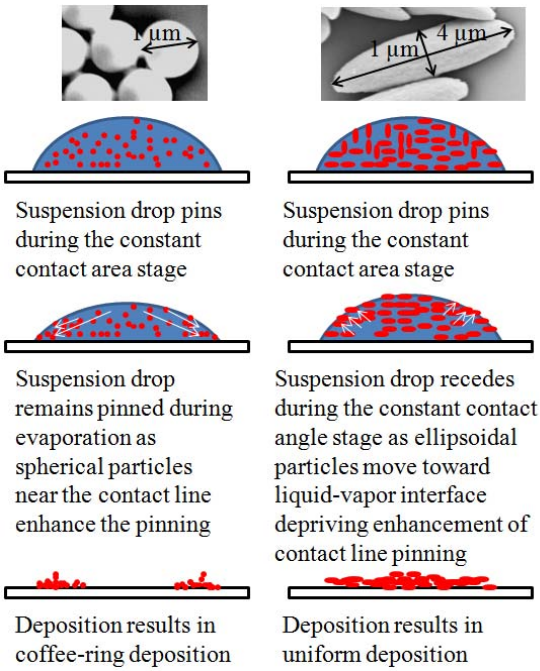

Figure 6.3. Schematic of deposition of particles from inkjet-printed evaporating colloidal drops consisting of (a) spherical particles and (b) ellipsoid particles.

It has been demonstrated for the case of spherical particles that the substrate wettability plays an important role in deposition morphology. The coffee-ring effect can be suppressed for a hydrophobic surface where the uniform evaporation rate along the liquid-vapor interface in the constant contact angle stage prevents an outward flow that carries particles to the contact line region. Similar behavior is observed in both Figures 6.2 (b) and 6.4 (a) for ellipsoidal particles. On a hydrophobic substrate, the deposition footprint is much more contained due to a smaller initial wetting area of the drop. In Figure 6.4 (a), the contact line continuously recedes during evaporation and ellipsoidal particle are collected at the liquid-vapor interface suppressing the coffee ring effect. Evaporation of an inkjet-printed colloidal drop on a hydrophilic substrate also does not

result in a coffee-ring deposition as shown in Figure 6.4 (b). Here, as the drop evaporates, the contact line remains pinned for most of the evaporation process (80% of the total evaporation duration). Even at such a late stage of evaporation, lack of the movement of particles toward the pinned contact line can only be explained by their presence near the liquid-vapor interface where there is a limited evaporative flow towards the pinned contact line.

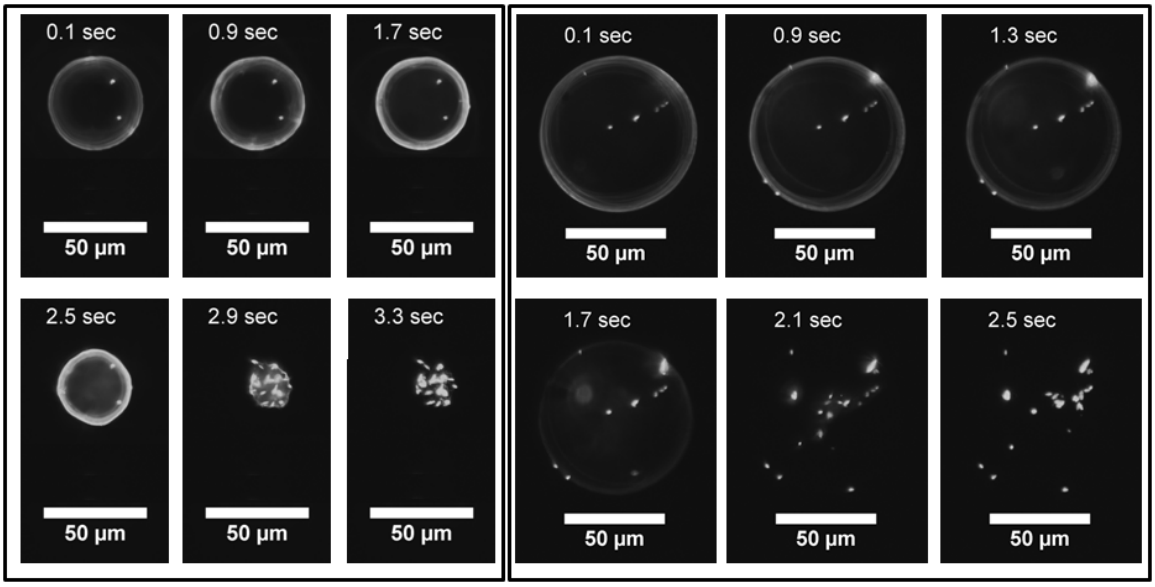

(b) (b)

Figure 6.4. Snapshots of evaporating colloidal drops consisting of ellipsoidal particles (0.6% v/v). Colloidal drops are printed onto a clean glass substrate with (a) θ_{RCA} = 85° and (b) θ_{RCA} = 0° at RH = 50%. During evaporation, the contact line recedes continuously for the case of a hydrophobic drop and the coffee-ring effect is suppressed.

6.4. Conclusions

Deposition behavior of ellipsoidal particles from an inkjet-printed colloidal drop is captured in real time using fluorescence microscopy. In contrast to the coffee-ring

effect observed for the case of a dilute colloidal drop containing spherical particles evaporating on a hydrophilic substrate, ellipsoids deposit more uniformly due to the strong assembly of particles near the liquid-vapor interface preventing them from reaching the drop edge. The effect of substrate wettability on the deposition of ellipsoidal particles is also examined. Although the deposition area decreases as the increase in drop static receding contact angle, the coffee ring is not observed in all cases studied.

Chapter 7 : INKJET PRINTING APPLICATION I: CONDUCTING LINES

7.1. Introduction

In recent years, organic conducting polymers such as poly(3,4-ethylenedioxythiophene) poly(sty[§]renesulfonate) (PEDOT:PSS) have been used as a key component for flexible electronics. PEDOT:PSS is a low energy bandgap conductive conjugated polymer and the chemical structures of PEDOT and PSS are shown in Fig. 7.1. PEDOT:PSS can be dispersed in water to form stable inks that are jettable using an inkjet printer. When the thickness of the PEDOT:PSS layer is below 800nm, it also shows good transparency.

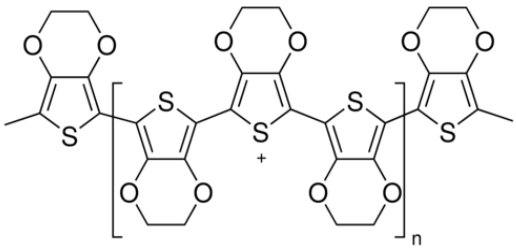

poly(3,4-ethylenedioxythiophene) (PEDOT)

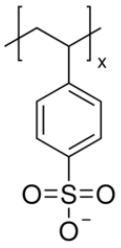

poly(styrenesulfonate) (PSS)

Figure 7.1. Chemical structure of PEDOT and PSS[148].

M Fleischman, B Lee, V Rodriguez-Santiago, V Chhasatia, Y Sun, D Pappas, "Hybrid Method Involving Atmospheric Plasma Treatment and Inkjet Deposition for the Development of Conductive Patterns on Flexible Polymers", Surface and Coatings Technology 2012 (Accepted), SURFCOAT-D-11-02628.

As reviewed in Section 1.3.5, inkjet printing of conducting lines consisting of PEDOT:PSS have been examined by Duineveld[45] and Subramanian and Soltman[50], among others[149]. It was found that the stability of printed lines is determined by drop spacing and substrate wettability. Recent studies have shown that changing the wettability of a substrate through plasma treatments does affect the morphology and quality of inkjet printed lines and single drops. Drop morphology of silver nanoparticles on hydrophobic and hydrophilic glass substrates was studied by Lee and Oh[150]. In their study, glass substrates were exposed to low pressure C_4F_8 plasma for 2 minutes to produce hydrophobic surfaces. The hydrophilic surfaces were produced through treatment under low pressure oxygen plasma for 2 minutes. The formed drops on the hydrophobic surfaces had thick morphologies compared to those on hydrophilic surfaces. In a study by Wang et. al.[151], the sharpness of pigment-based inkjet printed lines was investigated on control and plasma treated polyester fabric. The fabric was treated with low pressure oxygen plasma for 9 minutes which resulted in a sharper printed line compared to the untreated fabric. Atmospheric pressure air-argon plasma has also been used to improve the wettability of polyester fabrics[152, 153]. In this study, Zhang and Fang improved the sharpness of pigment inkjet printed patterns on 150 second plasma treated polyester fabric.

In this chapter, the wettability of flexible polymer substrate polyethylene naphthalate (PEN) was modified under two different plasma chemistries, namely helium-oxygen (He-O_2) and helium-water vapor (He-H_2O) plasmas at atmospheric pressure and room temperature. Printing was performed using the conductive PEDOT:PSS on the as-

received and plasma treated PEN surfaces where the shape and morphology of the lines were studied.

7.2. Experimental details

The experiment has been divided in two major parts. The first part includes atmospheric plasma modification and characterization of 50 μm thick PEN (Polyethylene naphthalate (Dupont: Teonex Q51)) substrates, and the second part consists of printing of PEDOT:PSS on the PEN substrates. The first part was conducted in collaboration with the Army Research Laboratory in Aberdeen, MD.

7.2.1. Sample preparation

PEN was chosen because of its better thermal, barrier, and mechanical properties compared to other polymers such as polyethylene terephthalate (PET). PEN substrates have static water contact angle of 86°. The substrates were rinsed in an ethanol bath for 10 minutes to remove residual surface contamination and then were air-dried once removed.

The atmospheric plasma system used in this study was a dielectric barrier discharge system from Sigma Technologies International, Inc. (model: APC 2000). PEN samples were plasma treated under helium-oxygen (He-O_2) and helium-water vapor (He-H_2O) plasmas. For the He-O_2 plasma, a constant helium flow of 14 L/min was used while the oxygen flow was varied from 70 – 700 sccm (standard cubic centimeters per minute). These flow rates were divided equally to each electrode. The amount of water vapor introduced into the plasma can be controlled by changing the temperature and flow of the

carrier gas in the evaporator. In this study, the temperature of the evaporator was kept at 25°C and the flow of the carrier gas (helium in this case) was kept at 12 L/min which provided a water vapor mass fraction of 65.2 mg/g. For the He-H_2O plasma experiments, one electrode (#2) was used for pre-treatment using the carrier gas (helium) and the other electrode (#1) was used for functionalization purposes using the reactive gas (water vapor). The cleaned PEN samples were mounted on the rotating dielectric surface, and the plasma exposure time was varied between 0.27 and 27 seconds by changing the rotating speed of the roller and varying the number of rotations. The effect of surface wettability/chemistry on power density and exposure time was investigated for each plasma chemistry. The oxygen concentration was varied to achieve the lowest water contact angle.

7.2.2. PEN surface characterization

Wettability testing was carried out using a static contact angle setup and by applying the sessile drop method. Water contact angles were measured using de-ionized water, and surface energies were obtained by measuring the contact angle using de-ionized water, dimethyl formamide, and diiodomethane as test liquids. These test liquids were used due to their wide range of polarities. Six drops (5 μL each) of the test liquid were used for the control and plasma treated samples, and the values were averaged to obtain a contact angle value.

Atomic force microscopy (AFM) was used to study the morphological changes to the PEN that arose from plasma treatment. The AFM system used was a Dimension 3100 microscope with a Nanoscope V controller (Digital Instruments/Veeco). Imaging was

done in tapping mode, using TESP (silicon) cantilevers (Veeco Probes) with an oscillation frequency of 300 kHz and at a 0.6 Hz scan rate while the selected scan areas were 50 × 50 μm. Using Nanoscope software (v7.30), images were flattened to the third order, followed by roughness analysis. Root mean square (rms) roughness values from 3 images, obtained from different locations on each sample were averaged.

7.2.3. Printing of PEDOT:PSS

A custom piezoelectric inkjet printing setup was used for this work and a schematic of the setup is shown in Figure 2.1. It consists of a high resolution (0.5 μm/ pixel) Sensi-Cam QE charged coupled device (CCD) camera (Romulus, Michigan) and a Navitar 12× zoom lens (Rochester, New York), synchronized with a halogen strobe light and the drop ejection to form a high magnification goniometer for side-view observation. The piezoelectric print head (MicroFab MJ-AL-01-80, Plano, Texas) allows for drop-on-demand inkjet printing; whereas, the CCD camera and the strobe light are used for visualization of the drop during flight in order to determine drop stability. The substrates were attached to a programmable x-y stage, which allowed for the substrate to translate while the printing nozzle remained fixed.

The effect of drop spacing on line deposition for each of the different plasma treated PEN substrates was observed by varying the spacing between the centers of two consecutive drops from 25% to 125% of the measured in flight drop diameter. All inkjet printing experiments were conducted at normal ambient room conditions (i.e. 23°C, atmospheric pressure, and 30% relative humidity) with a printing frequency of 20 Hz, a nozzle diameter of 80 μm, and a drop flight distance of approximately 1 mm. The PEDOT:PSS ink used in this work consisted of a 1:2 ratio of PEDOT:PSS (Clevios PH

500) to water which resulted in the PEDOT:PSS ink having a viscosity of 5.69 ± 0.12 cP and a surface tension of 63.21 ± 0.18 mN/m.

7.2.4. PEDOT:PSS printing characterization

Optical images of the inkjet printed PEDOT:PSS lines were obtained using a standard optical microscope (Nikon Eclipse ME600) at a magnification of 5× in order to determine and compare the overall line morphology between the as-received PEN and the plasma treated samples. The scanning electron microscope (SEM) that was used for this study was a Zeiss Supra 50VP using a bias voltage of 5.0 kV and a working distance of 2.0 mm. SEM was used in order to understand the particle morphology and deposition within the inkjet-printed drops of PEDOT:PSS on the plasma treated substrates.

7.3. Results and discussion

7.3.1. PEN surface modification

A power density of 0.94 W/cm^2 for the helium-oxygen plasma and 1.04 W/cm^2 for the helium-water vapor plasma were used. The water contact angle (WCA) exhibits a dramatic decrease from 86° (as-received film) to an average of about 25° and 11° for the PEN treated under He-O_2 and He-H_2O plasmas, respectively. WCA measurements as a function of exposure time for He-O_2 (0.5% oxygen in helium) and He-H_2O plasma treated PEN were also conducted. Surface modification occurs within fractions of a second of plasma exposure where the minimum WCA was reached at 0.42 seconds of exposure for He-H_2O treated PEN and 1.35 seconds of exposure for He-O_2 treated PEN.

The maximum WCA decrease was 68% and 85% for He-O_2 and He-H_2O plasma treated PEN, respectively.

The shelf life of the plasma treated PEN is a property that needs to be considered. Aging of a plasma modified polymer surface can occur when the newly formed polar groups migrate into the bulk of the polymer through chain rotations and translations. This results in non-polar groups moving to the surface and increasing the WCA. The aging effect of the plasma treated PEN is shown in Figure 7.2. PEN samples were treated under 0.5% oxygen in helium plasma with a power density of 0.94 W/cm^2 for 13.5 seconds. Similarly, PEN samples were treated under a He-H_2O plasma with a power density of 1.04 W/cm^2 for 6.75 seconds. The WCA for these samples was measured periodically up to 700 hours or one month. The WCA for the He-O_2 treated PEN started at 25° and increased to 53° 1 month after the day of plasma exposure. This final value is about 30° lower than that of the untreated PEN. When comparing these equations, the He-H_2O plasma treated PEN is aging twice as fast as the He-O_2 plasma treated PEN. It is important to note that during this aging study, the WCA never reached the as-received value. Also, the WCA measurements for the He-H_2O plasma treated PEN always remained lower than that of the He-O_2 plasma treated PEN.

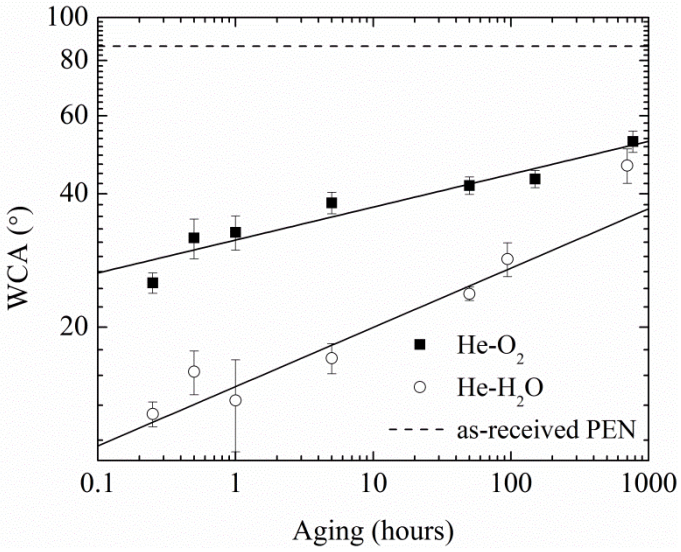

Figure 7.2. Water contact angle (WCA) data as a function of aging of the PEN surface exposure to He-O2 plasma and He-H2O plasma.

The morphology of the untreated and plasma modified PEN obtained from AFM studies is shown in Figure 7.3. The features on the surface are about 2 μm wide and 200 nm tall and they are found over the entire as-received sample (Figure 7.3(a)). The root mean square (rms) roughness for the untreated PEN is 13.3 nm. Figures 7.3(b), (c), (d), and (e) show the surface morphology of plasma treated PEN versus treatment time. The samples treated with He-O_2 plasma have an rms roughness of 11.5 nm and 16.3 nm for short and long exposure times, respectively. The slight increase in roughness after 27.0 seconds of exposure is attributed to the nano-roughness among the tall spikes as seen in Figure 7.3(b). The rms roughness for the short and long exposure to He-H_2O plasma are 12.9 nm and 11.8 nm, respectively. After 27.0 seconds of exposure to He-H_2O plasma, the spiked features are etched. Overall, there is no significant roughness change between the untreated and plasma-treated PEN leading to the conclusion that the overall

improvement of the surface wettability of plasma modified PEN is due to the oxidation of the surface and not due to the increased surface roughness.

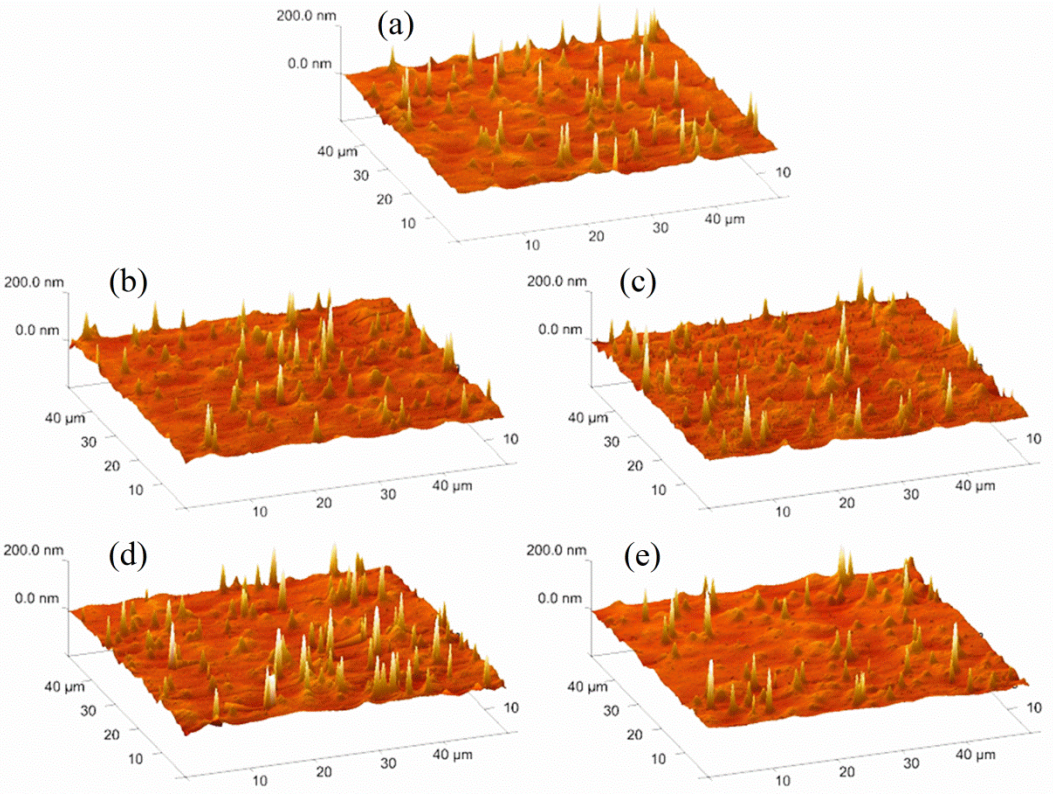

Figure 7.3. AFM 3D images of (a) as-received PEN and plasma treated PEN (b) He-O2 treatment for 1.3 s, (c) He-O2 treatment for 27.0 s, (d) He-H2O treatment for 1.3 s, and (e) He-H2O treatment for 27.0 s.

7.3.2. Inkjet printing of PEDOT:PSS

Inkjet printing of PEDOT:PSS was done on three different types of PEN samples: untreated samples, He-O_2 plasma treated samples, and He-H_2O plasma treated samples. The conditions for the He-O_2 plasma treated PEN were chosen to be 0.5% oxygen in helium, a power density of 0.94 W/cm^2, and exposure time of 13.5 seconds. The

conditions for the He-H_2O plasma-treated PEN were chosen to be a power density of 1.04 W/cm^2 and exposure time of 6.75 seconds. These conditions resulted in the lowest water contact angle and the maximum surface energy, as presented above. Since aging of the samples does occur, the printing was done within 24 hours of plasma treatment. The interaction between the different PEN surfaces and a single drop of PEDOT:PSS and printed lines of PEDOT:PSS was studied.

Figure 7.4 presents the single drop study of PEDOT:PSS on the three different types of PEN surfaces. The PEDOT:PSS particles agglomerated to the center of the drop on the untreated PEN sample due to its low surface energy leading to continuous contact line dewetting during drop evaporation. The deposition diameter of this drop is 65 μm. As the surface energy increases, the PEDOT:PSS particles spread more evenly inside the drop to eventually form a uniform deposition on the He-H_2O plasma treated PEN surface. The diameter of the drop deposit on the He-O_2 plasma treated PEN surface is also 65 μm, but the drop spreads to 135 μm in diameter on the He-H_2O plasma treated PEN. From Figure 7.4(a), the PEDOT:PSS drop on as-received substrate experiences all three stages of evaporation (i.e., constant contact area, constant contact angle, and mixed mode). In the constant contact area stage of evaporation, PEDOT:PSS ink is advected to the pinned contact line due to the evaporatively-driven flow. Once the contact angle reaches the static receding contact angle soon after a short constant contact area stage, the contact line starts to recede. At the constant contact angle stage, drop evaporation occurs uniformly along the liquid-vapor interface and the contact area of the drop decreases linearly with time[30]. The lack of long outward evaporative flow regime increases the PEDOT:PSS volume fraction inside the evaporative drop which increases the aggregation

of PEDOT:PSS. The receding liquid-vapor interface forces these aggregations toward the center of the drop[120]. In Figure 7.4(b), it can be seen that due to the aggregation of PEDOT:PSS near the contact line during constant contact area creates a "coffee ring" deposition on the He-O_2 plasma treated PEN substrate[37]. Here, improved wettability of the substrate restricts the receding of the contact line and limits aggregation of PEDOT:PSS compared to the as-received PEN substrate. In Figure 8.4(c), the He-H_2O plasma treated PEN substrate has a lower WCA which results in more spreading of the drop and restricts evaporation to only the constant contact area stage. Here, the lack of receding of the liquid-vapor interface restricts the formation of PEDOT:PSS aggregates. Overall, the increased surface energy reduced agglomeration of the PEDOT:PSS.

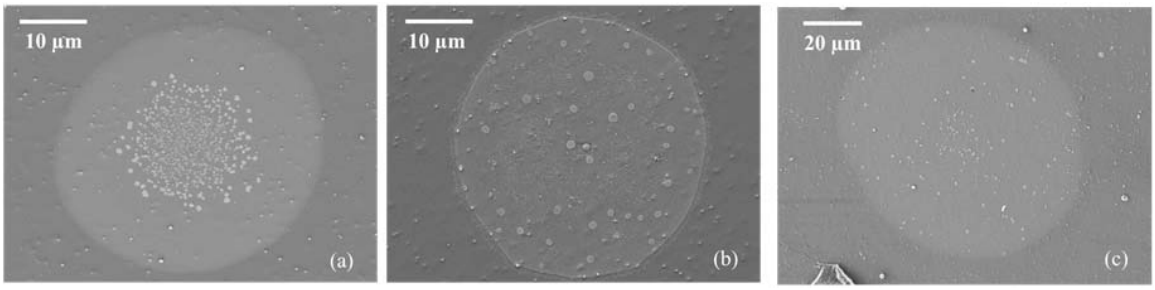

Figure 7.4. SEM images of PEDOT:PSS single drops on (a) untreated PEN, (b) He-O_2 plasma treated PEN, and (c) He-H_2O plasma treated PEN.

The effects of varied drop spacing on inkjet-printed PEDOT:PSS lines were examined. The as-received PEN sample does not allow for the formation of a connected uniform line but only allows for the deposition of isolated drops that get significantly larger as the drop spacing decreases (see Figure 7.5(a)). This is a result of the as-received PEN having a high water contact angle, which will result in a high advancing contact

angle and a receding contact angle that cannot be neglected. In Figures 7.5(b) and 7.5(c), the He-O_2 and He-H_2O plasma treated PEN samples show a large liquid instability at low drop spacing. This instability is reduced and a stable line deposition is produced as the drop spacing increases. However, if this drop spacing is too large then the uniform line starts to show a scalloped shape[50], which can be seen in Figure 7.5(c) for the 125% of drop spacing case on the He-H_2O plasma treated sample. The instability of the PEDOT:PSS line at lower drop spacing, which causes the bulges within the inkjet printed line, is a result of the instantaneous contact angle of the liquid with the substrate being greater than the static advancing contact angle[45]. However, it can be seen that uniform PEDOT:PSS lines can be formed on both the He-O_2 and He-H_2O plasma treated substrates at different drop spacing, where the particle deposition within the lines for the He-O_2 and He-H_2O PEN substrates are different. Nonetheless, there is optimal drop spacing for printed lines on the He-O_2 and He-H_2O plasma treated PEN surface and they are 50% and 100% of the drop diameter, respectively. Since these surfaces differ in surface energy and water contact angle, it is expected that the optimal printing condition for the 2 plasma chemistries (helium-oxygen and helium-water vapor) would be different.

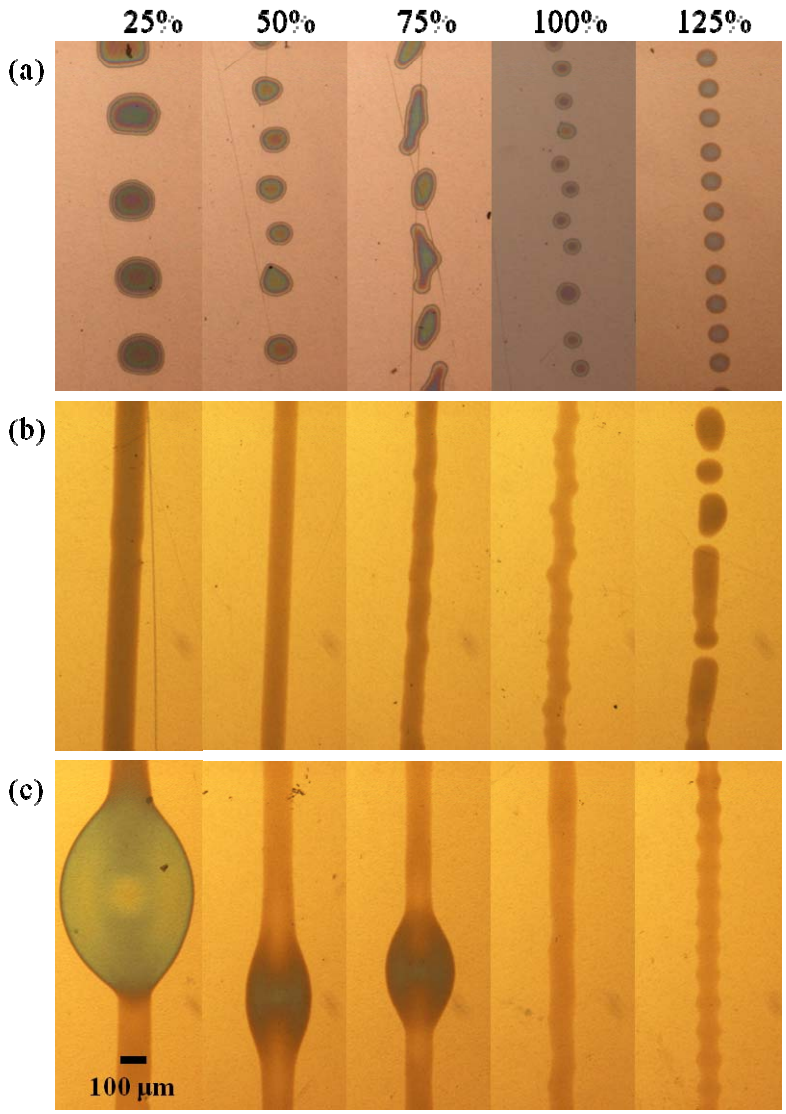

Figure 7.5. Optical images of printed PEDOT:PSS lines versus drop spacing on (a) as-received PEN, (b) He-O_2 plasma treated PEN, and (c) He-H_2O plasma treated PEN plasma treated PEN.

7.4.Conclusions

Atmospheric pressure helium-oxygen and helium-water vapor plasma chemically modified the surface of PEN promoting the formation of well-defined and uniform printed PEDOT:PSS lines. The total WCA decrease was 68% and 85% for He-O_2 and He-H_2O plasma treated PEN, respectively, which is attributed to oxidation of the surface

and not increased surface roughness. This significant decrease in WCA was observed for plasma treatments of only fractions of a second to a few seconds. After He-O_2 plasma treatment, the surface energy of PEN increased by 35%. The surface energy of PEN increased by 42% after He-H_2O plasma treatment. This resulted in a significant change in the polar and dispersive components. XPS results confirm the oxidation of the PEN surface upon plasma treatment and show addition of new O-C-O and OH-C=O groups on the surface of plasma treated PEN. Aging of the newly functionalized PEN surface occurs. He-H_2O plasma treated PEN ages twice as fast as the He-O_2 plasma treated PEN, but after one month the water contact angles are still at least 30° lower than that of the untreated PEN. With this improved wettability, continuous PEDOT:PSS lines were printed on plasma treated PEN. Atmospheric plasma offers a more attractive method to modify the surface energy of flexible polymer substrates. The hybrid method of atmospheric plasma processing and inkjet printing of water based organic ink allows for an earth-friendly technique for producing conductive patterning on flexible substrates for the fabrication of light emitting diodes, thin film photovoltaics, and polymer electronics.

Chapter 8 : INKJET PRINTING APPLICATION II: ORGANIC SOLAR CELLS

8.1. Introduction

Growing environmental concerns around the globe regarding carbon emissions from the power plant and the rising awareness of sustainability are driving the development of renewable and alternative energy sources. Among various alternative energy strategies, solar energy is the most abundant energy on Earth and its diverse use may enable a secure and clean energy future. In recent years, research in solar cells has been growing exponentially and new records of solar cell efficiencies have been made every year as summarized in Figure 8.1.

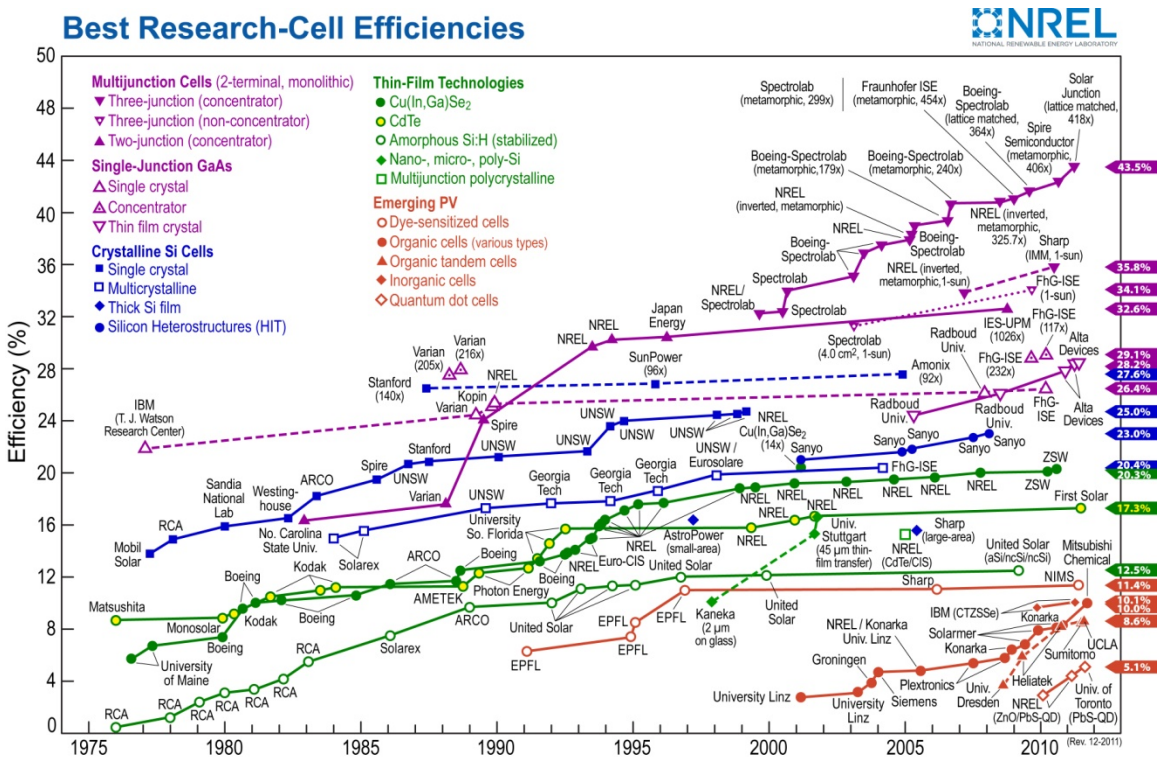

Figure 8.1. Progress in solar cell performance[154].

Traditional crystalline silicon based solar cells still hold the highest efficiency as seen from Figure 8.1. The second generation solar cells are based on thin film technologies of semiconductor materials and the third generation solar cells are made from a variety of materials, including polymer solar cells, nanocrystalline cells, and dye-sensitized solar cells, to reduce initial materials cost. Since the beginning of the millennium, organic solar cells have become an active area of research, especially the bulk heterojunction cells (e.g., P3HT:PCBM) where almost one new research article has been published every day since 2008[155]. Figures 8.2 (a) and (b) show the chemical structures of P3HT and PCBM. Published values of efficiencies for P3HT:PCBM based bulk heterojunction cells have reached to 5% for the active layer thickness of 100 nm as shown in Fig. 8.2 (c).

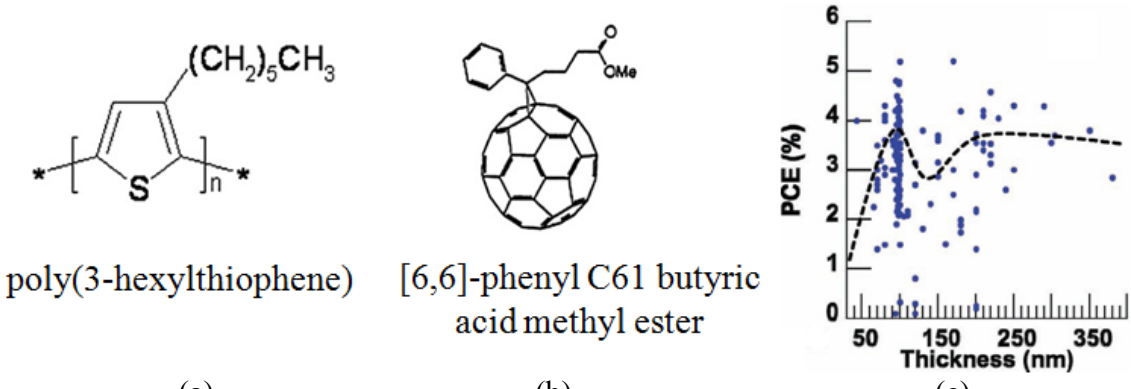

(a) (b) (c)

Figure 8.2. Structures of P3HT and PCBM, and published efficiencies of P3HT:PCBM based solar cells. (a) Structure of P3HT, (b) structure of PCBM and (c) published efficiencies of bulk heterojunction solar cells as a function of thickness of P3HT:PCBM[155].

In bulk heterojunction photovoltaic cells, the electron donor and acceptor are mixed together to form a polymer blend. The excitons (electron and hole pairs) will

separate efficiently if the characteristic length scale of the blend is similar to the exciton diffusion length so that most of excitons generated in either material may reach the interface. Electrons move to the acceptors are then collected by one electrode, and holes are collected on the other side as shown in the Figure 8.3. As the light shines on a P3HT:PCBM bulk heterojunction solar cell, electron and hole pairs are generated in the photoactive (P3HT:PCBM) layer. In a regular solar cell, the electrons are collected by the metal electrode (–ve electrode, usually Al) and the holes are collected by PEDOT:PSS. The ITO layer acts as the other electrode (+ve electrode) as shown in Figure 8.3 (a). In inverted solar cells shown in Fig. 8.3 (b), the photoactive materials can be printed after depositing a layer of ZnO or TiO_2 on ITO-coated substrates. A high work function metal such as Ag collects holes. ZnO or TiO_2 is used as a hole-blocking layer that improves photovoltage. In addition, the inverted structure can be processed, stored, and tested in air, rendering it much more robust than conventional OPV designs that must be handled in an inert atmosphere. Air-stability is an important advantage for manufacturability and device lifetime.

Spin coating has served as an excellent means to evaluate and optimize the chemical structure of the materials as well as the nanomorphology of the deposited photoactive layers. However, spin coating is not a scalable process and it wastes a lot of ink. The roll-to-roll compatible printing process is expected to be much faster and less expensive.

Printing of the photoactive layer has been carried out by Hoth et al.[91, 156], Aernouts et al.[92] and Eom et al.[93] Research in the printing of inverted solar cells has been lacking so far. In this chapter, the fabrication of inverted solar cells with the

Glass/ITO/ZnO/P3HT:PCBM/Ag structure is performed. The effects of printing parameters on the photoactive layer thickness, morphology, cell performance, and stability are examined.

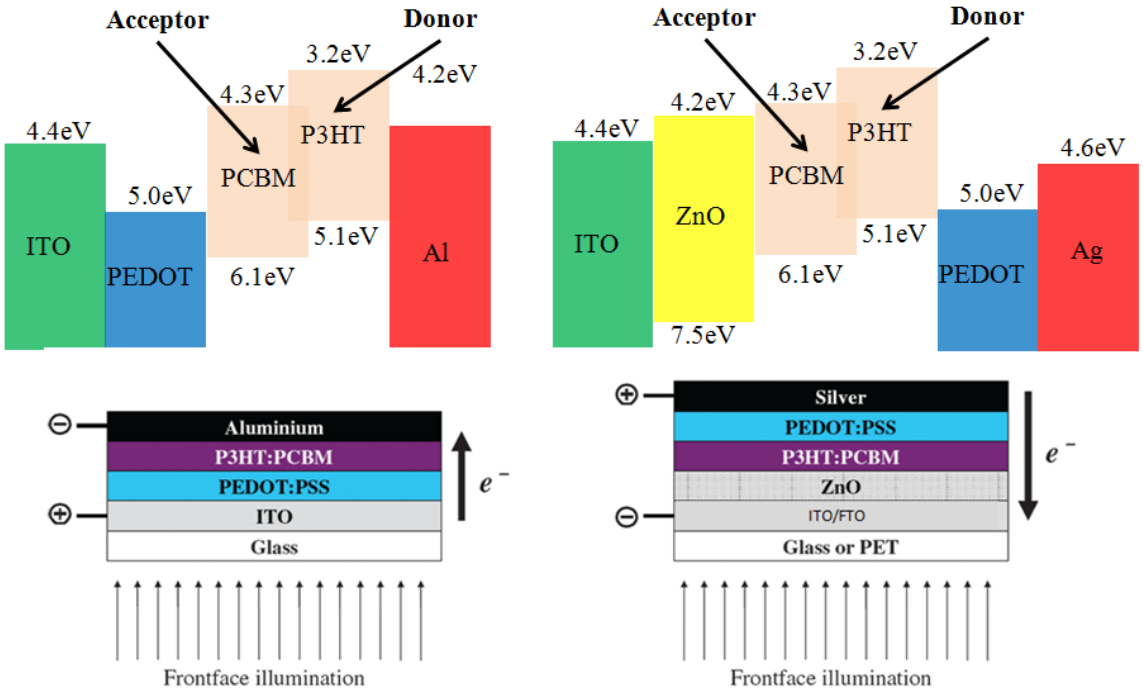

Figure 8.3. Structures of bulk heterojunction solar cells. (a) Regular solar cell and (b) inverted solar cell.

8.2. Experimental details

The layers of inverted solar cells were fabricated using the combination of dip-coating, inkjet printing, and thermal evaporation. ITO coated glass substrates purchased from Colorado Concepts Coatings (Loveland, Colorado) have a 130 nm ITO layer. A 70 nm thick ZnO thin film is coated on top of the ITO using a custom made dip-coater. Substrates were seeded with a thin ZnO film by dip-coating in an ethanol solution that

contains 0.375 M zinc acetate and 0.375 M monoethanolamine (MEA), with a withdrawal rate of 200 mm/min[157, 158]. Substrates were then annealed on a hotplate at 400 °C for 20 min. The 1wt% P3HT (Sigma Aldrich, USA) is blended with 1% PCBM (American Dye Source, Canada) in 68% oDCB and 32% Mesitylene solution. The ink is then heated at 100°C for 15 seconds and stirred overnight to dissolve P3HT:PCBM in the oDCB:Mesitylene bi-solvent. The prepared ink can be printed by using a Dimatix DMP-2831 printer with a DMC-11610 cartridge that is capable of jetting 10 pL drops. Here, the printing frequency and spacing between the drops have been changed systematically to examine their effects on the thickness, morphology, and property of printed layers.

Printed P3HT:PCBM layers are then annealed at 140 °C for 10 minutes to remove oDCB:Mesitylene residue from the deposition. Annealing also improves the crystallinity of P3HT. Later Ag (150 nm) is coated on the P3HT:PCBM layer by using a thermal evaporator. The solar cells are finally tested for their I-V response by subjecting them under a solar simulator (light intensity – 100 mW/cm^2). Absorption spectrum of the printed P3HT:PCBM layer is also obtained to improve performance of the solar cell.

8.3. Results and discussion

The printed layer of P3HT:PCBM is observed under an optical microscope to check for the presence of visible pin holes. It was found from printing of PEDOT:PSS lines that for steady lines to form, liquid drops must not de-pin the substrate[45]. The ink consisting of P3HT:PCBM in o-DCB:Mesityline has a 0° receding contact angle with a ZnO substrate. However, on a fluidphilic substrate, the supply of ink should balance the spreading and evaporation of the ink, otherwise line bulging can occur. To prevent the

bulging effect, the jetting frequency was varied, while keeping the drop spacing fixed at 55 µm. Optical images of printed P3HT:PCBM layers on ZnO/ITO/glass substrates for jetting frequencies of 0.7, 1, 1.5, and 2 kHz with 55 µm drop and line spacing are shown in Fig. 8.4. It can be observed that the most stable lines and hence the most uniform film are obtained at a jetting frequency of 1.5 KHz. At a higher frequency, the excessive liquid from printed drops results in the formation of bulges and puddles, while at a lower frequency a higher solvent evaporation rate leads to discontinuous lines and pin holes.

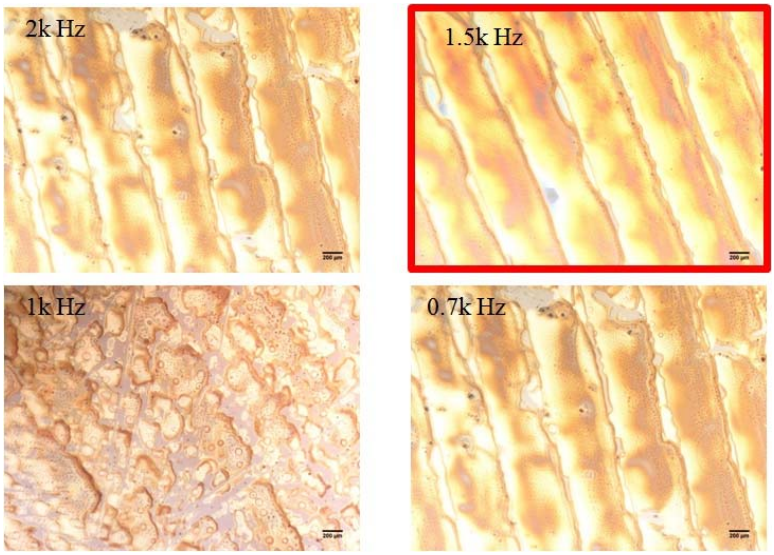

Figure 8.4. Optical images of printed P3HT:PCBM layers on ZnO/ITO/Glass substrates at 2, 1.5, 1 and 0.7 KHz with 55 µm drop and line spacing.

The drop and line spacing was then varied when keeping the jetting frequency fixed at 1.5 KHz. Optical images of printed P3HT:PCBM layers on ZnO/ITO/glass substrates for drop and line spacing of 55, 60, 65, and 70 µm are shown in Fig. 8.5. As the drop and line spacing vary, the amount of ink available to wet the substrate changes

and the thickness of the deposited layer changes as well. It can be observed from Fig. 8.5 that the most stable lines and hence the most uniform film are obtained for a drop spacing of 65 µm. For a lower spacing, the excessive liquid results in the formation of bulges and puddles, and at a higher spacing, the lack of solvent yields incomplete wetting of the substrate.

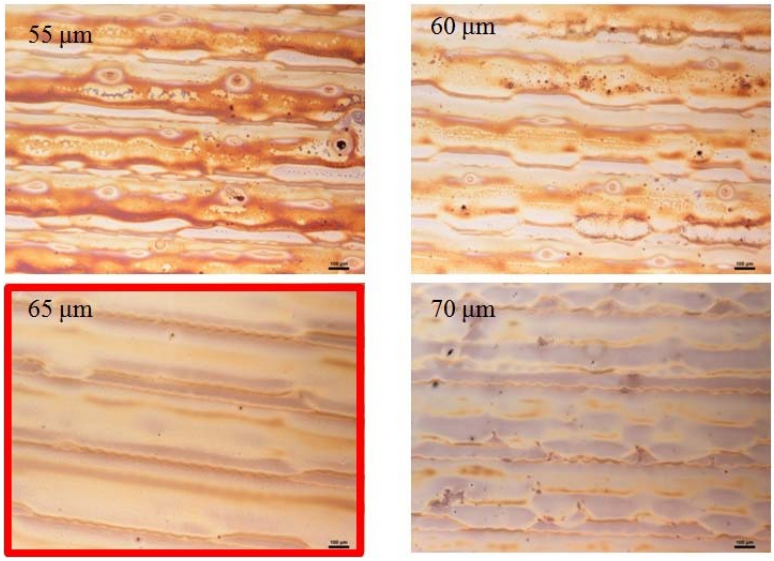

Figure 8.5. Optical images of printed P3HT:PCBM layer on ZnO/ITO/glass substrates at 55, 60, 65 and 70 µm drop and line spacing and jetting frequency of 1.5 KHz.

Ink formulation also plays an important role on deposition morphology and properties. To avoid gelling/aggregation and surface roughness, P3HT with a lower molecular weight is recommended for inkjet printing. The solvents used to dissolve P3HT:PCBM blends affect the resulting morphology of the deposit[159]. In inkjet printing, a bi-solvent mixture is often used to suppress the coffee ring effect and hence create more uniform depositions[40]. Bi-solvent mixtures of mesitylene and o-DCB have been used in

literature[91, 156]. In this study, a greater contrast in solvent boiling points was explored, where mesitylene (15 °C difference in boiling point compared with o-DCB =) was replaced with toluene (69 °C boiling temperature difference with o-DCB), but both solvents have similar surface tensions. As shown in Fig. 8.6 (a) and (b), poor film morphologies are obtained for toluene containing inks. The corresponding I-V curves for P3HT:PCBM film based on toluene-o-DCB also show poor performance as compared with that of mesitylene-o-DCB based cells.

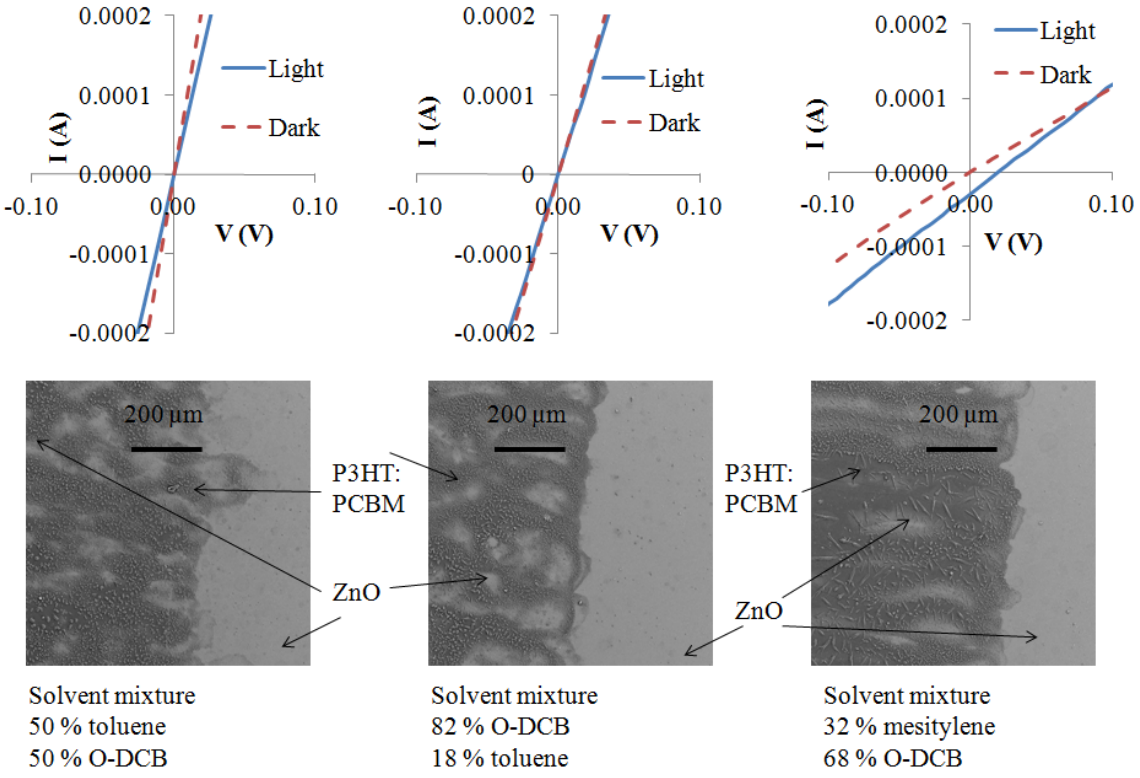

(a) (b) (c)

Figure 8.6. Top-view SEM images of the printed P3HT:PCBM layer and the corresponding I-V curve for the printed solar cell using different solvent compositions. (a) 50% toluene, 50% o-DCB, (b) 82% toluene, 18% o-DCB, and (c) 32% mesitylene, 68% o-DCB . All cells were printed at 1.5 KHz and 65 µm drop/line spacing.

The top-view SEM image of a solar cell printed using solvent composition of 32% mesitylene and 68% o-DCB, jetting frequency of 1.5 KHz, and /line spacing of 65 µm is shown in Fig. 8.7 (a). The presence of pin holes in the P3HT:PCBM layer creates an equivalent circuit that consists of a photo-diode and a resistor in parallel as the silver electrode comes in contact with the ZnO coating. These pin holes significantly deteriorate the performance of solar cells as shown in the I-V curve shown in Fig. 8.7 (b).

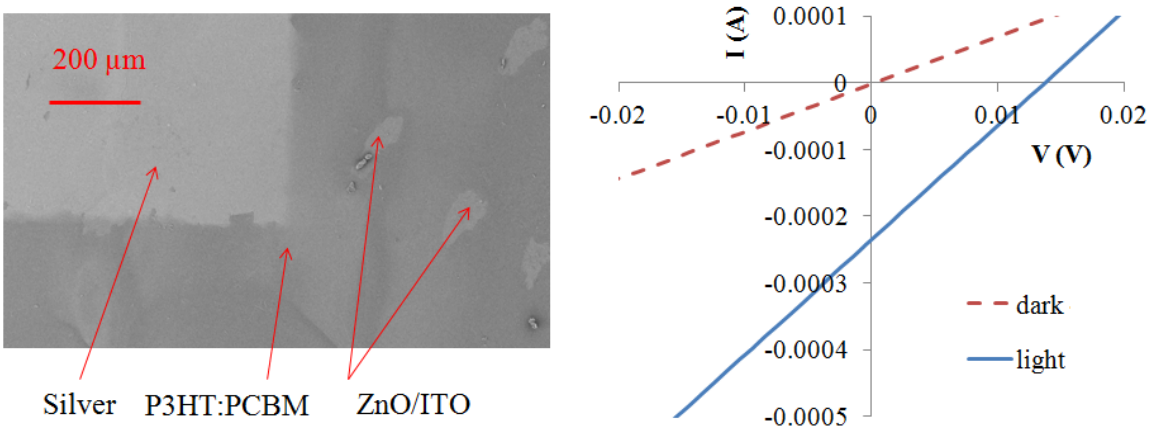

(a) (b)

Figure 8.7. Effect of pin holes in printed P3HT:PCBM layer on solar cell performance. (a) Top-view SEM image of printed solar cell and (b) I-V curve of the solar cell. The difference between light and dark curves indicates the presence of a photoactive layer. The solar cell was printed at 1.5 KHz and 65 µm drop/line spacing.

To avoid the formation of pin holes in the photoactive layer, the effect of multiple printing passes was examined. The comparison of deposition morphology of the photoactive layer using a single and multiple printing passes is shown in Fig. 8.8. It is shown that for the cases of two layers printed parallel and the single pass deposit, strong

line patterns are visible as shown in Figs. 8.8 (a) and (b). These strong line patterns can result in micro- or even nanoscale pin holes in the printed layers, and hence lead to poor cell performance as shown in Fig. 8.9. If the second pass is printed perpendicular to the direction of the first printing pass, the uniformity of the deposited film and cell performance are both improved as shown in Figs. 8.8 (c) and 8.9. Printing of two parallel layers increases the surface roughness of the printed film as shown in the SEM images (Fig. 8.8), causing worsening of the short circuit current as compared to the case of a single layer (Fig. 8.9 and Table 8.1). Printing of the second layer perpendicular to the first layer improves both I_{sc} and V_{oc} as the smoothness of the printed film increases and the holes are filled. The performance parameters of solar cells printed using a single, two parallel, and two perpendicular passes are summarized in Table 8.1.

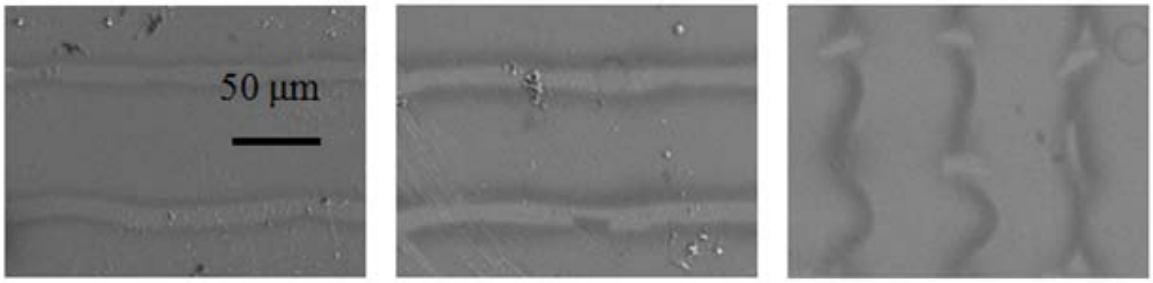

(a) (b) (c)

Figure 8.8. Comparison of deposition morphology of the photoactive (P3HT:PCBM) layer using a single and multiple printing passes. (a) Top-view SEM image of a single pass, (b) top-view SEM image of two parallel passes and (c) top-view SEM image of two crossed passes of P3HT:PCBM deposits. Solar cells were printed at 1.5 KHz and 65 µm drop/line spacing.

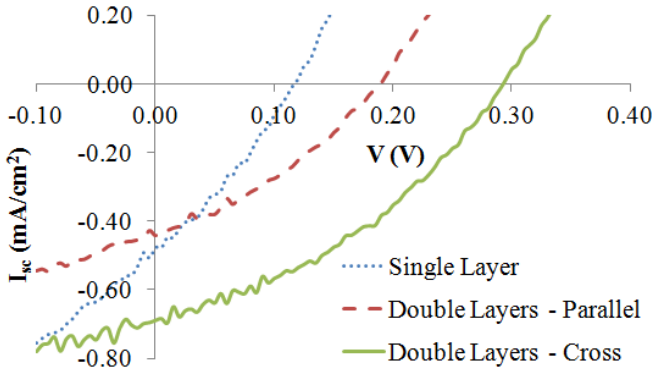

Figure 8.9. Light I-V curves of printed cells of a single, two parallel, and two crossed photoactive layers.

Table 8.1. Performance of printed solar cells of a single, two parallel, and two crossed layers.

Layer orientation (thickness - nm)	I_{sc} (mA/cm^2)	V_{oc} (V)	Fill factor	Efficiency (%)
Single layer (150)	0.49	0.12	0.300	0.017
Double layers – parallel (300)	0.44	0.19	0.343	0.028
Double layers – cross (300)	0.69	0.29	0.373	0.077

The absorption spectrum of the printed P3HT:PCBM layer is shown in Fig. 8.10. It can be seen that printing of two perpendicular layers increases the light absorption which facilitates cell performance However, the increase in light absorption comes with the increased thickness of the P3HT:PCBM layer, causing possible exciton recombinations.

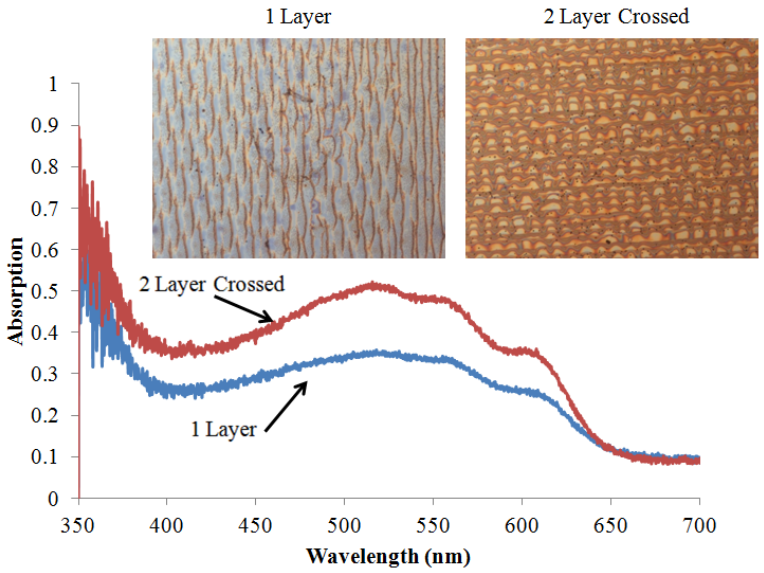

Figure 8.10. Absorption spectrum of the printed P3HT:PCBM layers.

The stability of printed solar cells is also studied by exposing them under light for longer time duration and the I-V curves for light exposure time of 0, 5, and 10 minutes are shown in Fig. 8.11. As the solar cell is exposed to light for longer duration, the solar cell performance degrades, primarily due to the degradation of the ZnO layer. The performance parameters for light exposure time of 0, 5, and 10 minutes are summarized in Table 8.2. As the light exposure time increases to 10 mins, the solar cell efficiency drops to 0.004%.

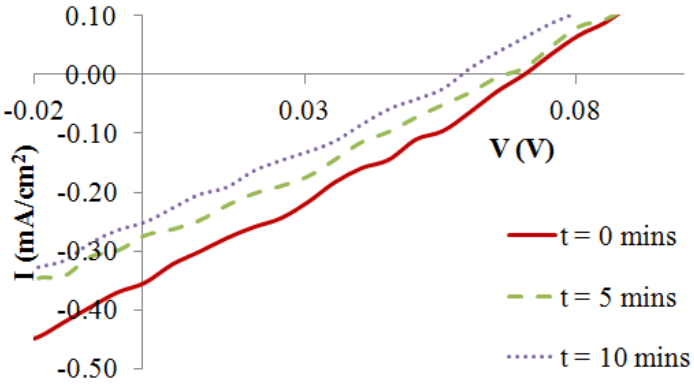

Figure 8.11. I-V curves for printed solar cells with 0, 5, and 10 mins light exposure time.

Table 8.2. cell performance of printed solar cells with different light exposure time.

Exposure time	I_{sc} (mA/cm^2)	V_{oc} (V)	Fill factor	Efficiency
0 minutes	0.36	0.07	0.269	0.007
10 minutes	0.29	0.07	0.271	0.005
20 minutes	0.26	0.06	0.269	0.004

The other parameter that affects the cell performance is the crystallinity of P3HT:PCBM due to annealing. As shown in Fig. 8.12 (a), large micron-sized crystals are observed in the top-view SEM image of the P3HT:PCBM layer. These crystals contain sulphur and oxygen beside carbon [Figs. 8.12 (b) and (c)] indicating the presence of P3HT (S) and PCBM (O). The crystallization of P3HT:PCBM results in locally concentrated P3HT:PCBM and causes performance degradation of printed solar cells.

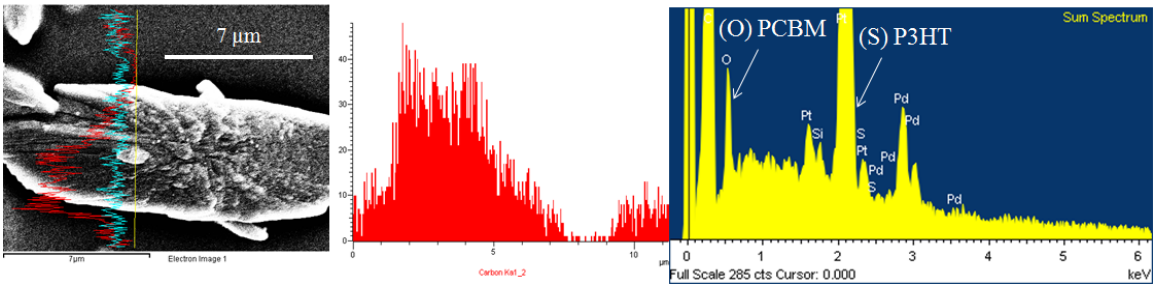

(a) (b) (c)

Figure 8.12. Characterization of the printed P3HT:PCBM layer after annealing (a) top-view SEM image and (b) EDS detection of carbon (c) EDS detection of oxyegen and sulphur.

8.4. Summary

Inverted organic solar cells are fabricated by using inkjet printing. The effects of solvent composition, drop/line spacing, jetting frequency, and printing patterns on deposition morphology of the P3HT:PCBM layer and performance of the solar cell are examined. Results show that the change in solvent composition from mesitylene to toluene weakens cell performance. Optimal printing parameters are explored and it is found that by printing two crossed layers, micro and nanoscale pin holes can be avoided. Performance of the solar cell can be improved with better control of P3HT:PCBM crystallization during the annealing process and replacing the ZnO layer with TiOx to improve the cell stability.

Chapter 9: CONCLUSIONS AND RECOMMENDATIONS

9.1. Conclusions

The ability to use low-cost, high volume inkjet printing technology for the manufacture of microdevices on flexible substrates can lead to the next revolution in microelectronics. To realize the tremendous potential of this technology, understanding of transport phenomena associated with the fabrication of printable devices is important. An attempt is made in this study to examine the effects of various parameters of colloids (e.g., size, volume fraction, and shape of the suspended particles, as well as the viscosity and surface tension of the carrier liquid), substrate wettability and environmental conditions on evaporation and particle deposition of inkjet-printed colloidal drops.

An experimental setup has been built to observe in real time the evaporation of colloidal drops from side and bottom views inside a well-controlled humidity chamber. The effect of relative humidity on drop evaporation and particle deposition was first studied. It was found that as humidity increases, slower evaporation results in a lower contact angle and more spreading of the printed drop. This in turn leads to a larger deposition area of suspended particles, thus, the RH is an important parameter dictating the evaporation rate and deposition dynamics of aqueous colloidal drops.

The deposition behavior of an inkjet-printed aqueous colloidal drop consisting of bi-dispersed micro and nanoparticles has been investigated for glass substrates of varying wettability. The surface tension, electrostatic, drag, and van der Waals forces acting on particles near the CL were estimated. The results show that, as the static receding contact angle, θ_{RCA}, varies from 85° to 0°, the duration of the three evaporation modes of a

colloidal drop significantly differ and so does the corresponding microflow patterns inside the evaporating drop. The differences in drop evaporation dynamics result in different particle assembly and deposition behaviors of bi-dispersed colloidal drops. For a hydrophilic substrate ($\theta_{RCA} = 0°$), the separation of micro and nano particles can be achieved. On a relatively hydrophobic surface ($\theta_{RCA} > 45°$) the micro and nano particles mix with each other. Partial separation of micro and nano particles can be obtained on a relatively hydrophilic substrate ($0° < \theta_{RCA} < 45°$). By modifying the substrate wettability, the interaction of forces acting on the particles is tuned. The control of particle separation according to their sizes can therefore be achieved.

The dynamics of coalescence, evaporation, and particle deposition of two inkjet-printed colloidal drops have been studied by jetting a second droplet on the pre-wetted region of the first printed drop. The effect of separation distance between two drops on particle deposition morphology has been examined. As the separation distance increases, the circularity of the deposition decreases. Moreover, the time delay between the ejection of two consecutive drops has been varied to observe the effect of printing frequency on final deposition. The interplay of three important time scales present during deposition of two consecutively printed colloidal drops, i.e., the evaporation time, drop delay time, and characteristic time for drop coalescence, determines the final deposition morphology. The results show that a longer delay between two printed drops causes the formation of two separate coffee rings as more particles deposited in the spreading area of the first drop. This is due to the capillary flow induced by a pressure gradient between the first and second drops, which pulls liquid from the second drop to flow into the first drop. While a

shorter delay leaves sufficient time for two drops to coalesce into one drop before particles are completely deposited.

The effect of particle shape on deposition morphology has been studied to suppress the "coffee-ring" deposit. In contrast to the coffee-ring deposit from a dilute colloidal drop containing spherical particles evaporating on a hydrophilic substrate, ellipsoidal particles deposit more uniformly due to the strong assembly of particles near the liquid-vapor interface preventing more particles from reaching the drop edge to pin the contact line. The effect of substrate wettability on deposition of ellipsoidal particles is also examined and the results show that, although the deposition area decreases as the increase in drop static receding contact angle, the coffee ring is not observed in all cases studied.

Applications of inkjet printing in deposition of conducting lines and fabrication of solar cells were explored. Printing was performance using the conductive PEDOT:PSS ink on as-received and atmospheric plasma treated PEN surfaces. It was found that the contact angle decrease was 68% and 85% for He-O_2 and He-H_2O plasma treated PEN, respectively, without any significant change in surface roughness. With this improved wettability, continuous and stable PEDOT:PSS lines were printed on plasma treated PEN. Finally, inverted organic solar cells were fabricated by inkjet printing. The effects of solvent composition, drop/line spacing, jetting frequency, and printing patterns on deposition morphology of the P3HT:PCBM layer and performance of the solar cell are examined. Optimal printing parameters were explored and it is found that pin holes can be avoided by applying two printing passes perpendicular to each other. Performance of

the solar cell needs to be improved with better control of P3HT:PCBM crystallization during annealing and by replacing the ZnO layer with TiOx to improve the cell stability.

The major achievements of this dissertation include:

- Designed and built an experimental setup for real time observation of evaporation of inkjet-printed drops using side-view and bottom-view imaging.
- Established the relationship between relative humidity (RH) and particle deposition morphology for aqueous inks, higher the RH, higher the spread of deposition.
- Established the criterion for distinguishing different colloidal droplet evaporation stages by providing a phase diagram for pining of particles near the contact line.
- Examined the deposition of bi-dispersed particles on substrates of varying wettability and controlled mixing (hydrophobic), partial separation and separation (hydrophilic) of particles according to their size in evaporating drops.
- Explored the relationship of drop spacing and delay time on coalescence of two consecutively printed colloidal drops and found that lower delay time improves uniformity of the deposition.
- Fabricated ellipsoidal particles from the spherical particles and printed them on substrates of varying wettability to observe the suppression of “coffee-ring”.
- Optimized parameters to print stable PEDOT:PSS (conducting polymer) lines on transparent substrates by treating the PEN substrates with atmospheric plasma and uniform P3HT:PCBM (photoactive) films by controlling ink formulation.

9.2. Recommendations for future research

The present work builds on the knowledge of material deposition from inkjet-printed colloidal drops. Some suggestions for the future work are:

- Effect of density mismatch on deposition morphology: In this study, neutrally buoyant suspensions were used. However, in inkjet printing of function materials, particle settling induced by the density difference between particles and carrier liquid can affect particle deposition morphology for both spherical and non-spherical particles and hence needs to be explored.
- Interaction of multiple drops: Coalescence of two drops is a starting point for the study of line deposition. Evolution of a single drop on a substrate after impact has been studied in detailed[2-5], and four different stages of evolution have been identified as kinematic, spreading, relaxation and equilibrium. Inertia, viscosity and capillary act as the determining factors during kinematic, spreading and relaxation stages respectively. Evolution of drop diameter during each of the stage is shown in the figure 9.1.

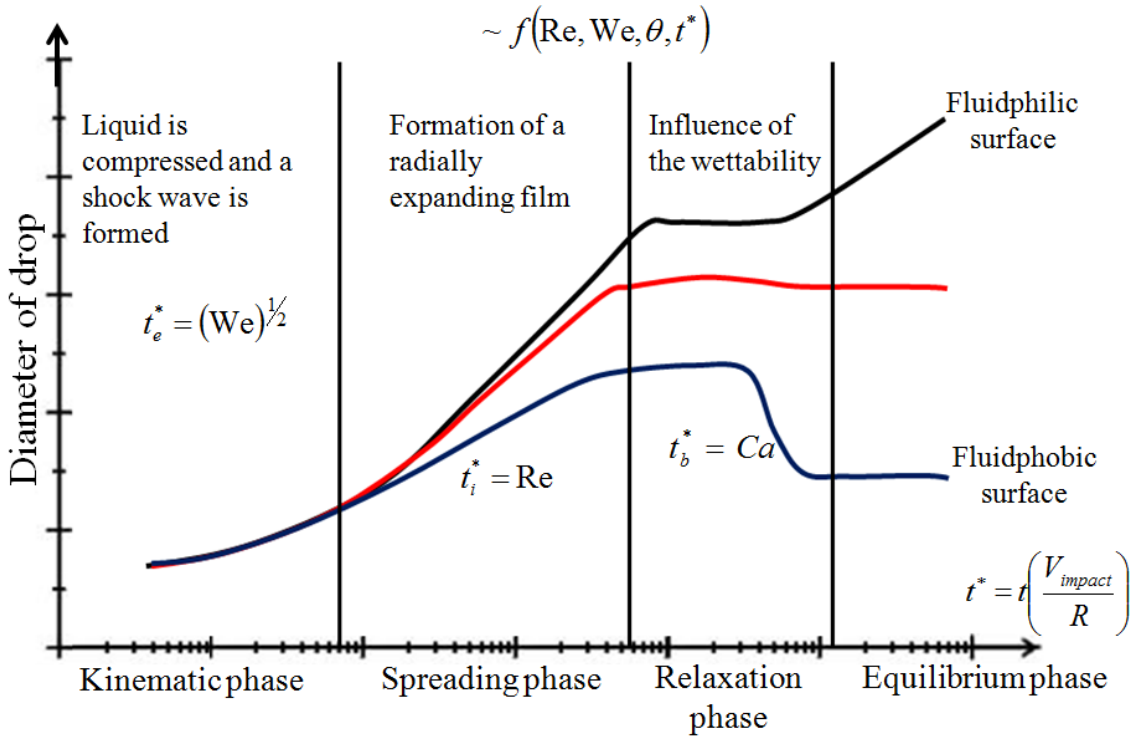

Figure.9.1. Evolution of drop diameter after impact of drop on a substrate.

However, effects of inertia, viscosity and capillary are not clear for coalescence of drops. Inclusion of a third drop can change the deposition behavior by introducing a long ridge between the first and third drop. In this long ridge, the competition between evaporative and capillary flows determines the microflow and particle deposition morphology during line printing.

- Heat transfer enhancement by the use of metal nanoparticle suspensions: Inkjet printing can be used to enhance cooling on local hotspots on a heat sink. By addition of nanoparticles, the receding contact angle of the colloidal drop can be decreased and heat transfer by evaporation can be increased due to the increase in contact line perimeter.

The experimental setup built here can be used to visualize the formation, impact, spreading, coalescence and evaporation of inkjet-printed drops in a wide range of applications. In the absence of fluorescent particles, the side-view images can provide real time information, and with the presence of fluorescent particles both the side and bottom view images can be compared with nano-second resolution using flash photography.

REFERENCES

1. Dong, H. M.; Carr, W. W.; Morris, J. F., An experimental study of drop-on-demand drop formation. *Physics of Fluids* 2006**,** 18, 072102.

2. Dong, H. M.; Carr, W. W.; Morris, J. F., Visualization of drop-on-demand inkjet: Drop formation and deposition. *Review of Scientific Instruments* 2006**,** 77, 085101.

3. Dong, H. M.; Carr, W. W.; Bucknall, D. G.; Morris, J. F., Temporally-resolved inkjet drop impaction on surfaces. *AIChE Journal* 2007**,** 53, 2606-2617.

4. van Dam, D. B.; Le Clerc, C., Experimental study of the impact of an ink-jet printed droplet on a solid substrate. *Physics of Fluids* 2004**,** 16, 3403-3414.

5. Lim, T.; Han, S.; Chung, J.; Chung, J. T.; Ko, S.; Grigoropoulos, C. P., Experimental study on spreading and evaporation of inkjet printed pico-liter droplet on a heated substrate. *International Journal of Heat and Mass Transfer* 2009**,** 52, 431-441.

6. Kaneda, M.; Ishizuka, H.; Sakai, Y.; Fukai, J.; Yasutake, S., Film formation from polymer solution using inkjet printing method. *AIChE Journal* 2007**,** 53, 1100-1108.

7. Le, H. P., Progress and trends in ink-jet printing technology. *Journal of Imaging Science and Technology* 1998**,** 42, 49-62.

8. Doring, M., Ink-jet printing. *Philips Technical Review* 1982**,** 40, 192-198.

9. Perelaer, J.; Smith, P. J.; Hendriks, C. E.; van den Berg, A. M. J.; Schubert, U. S., The preferential deposition of silica micro-particles at the boundary of inkjet printed droplets. *Soft Matter* 2008**,** 4, 1072-1078.

10. Yarin, A. L., Drop impact dynamics: Splashing, spreading, receding, bouncing. *Annual Review of Fluid Mechanics* 2006**,** 38, 159-192.

11. M, R.; A, F., A numerical study of the mechanism of splashing. *Int. J. Heat Fluid Flow* 1999**,** 20, 455.

12. Nicolas, M., Spreading of a drop of neutrally buoyant suspension. *Journal of Fluid Mechanics* 2005**,** 545, 271-280.

13. Pesach, D.; Marmur, A., Marangoni Effects in the Spreading of Liquid-Mixtures on a Solid. *Langmuir* 1987**,** 3, 519-524.

14. Hoffman, R. L., A study of the advancing interface. I. Interface shape in liquid-gas systems. *Journal of Colloid and Interface Science* 1975**,** 50, 228-41.

15. Strom, G.; Fredriksson, M.; Stenius, P.; Radoev, B., Kinetics of steady-state wetting. *Journal of Colloid and Interface Science* 1990**,** 134, 107-116.

16. Cox, R. G., The dynamics of the spreading of liquids on a solid surface. I. Viscous flow. *Journal of Fluid Mechanics* 1986**,** 168, 169-94.

17. Bonn, D.; Eggers, J.; Indekeu, J.; Meunier, J., Wetting and spreading. *Reviews of Modern Physics* 2009**,** 81, 739-805.

18. Birdi, K. S.; Vu, D. T.; Winter, A., A Study of the Evaporation Rates of Small Water Drops Placed on a Solid-Surface. *Journal of Physical Chemistry* 1989**,** 93, 3702-3703.

19. Kim, J. H.; Ahn, S. I.; Kim, J. H.; Zin, W. C., Evaporation of water droplets on polymer surfaces. *Langmuir* 2007**,** 23, 6163-6169.

20. Hocking, L. M., On contact angles in evaporating liquids. *Physics of Fluids* 1995**,** 7, 2950-2954.

21. Hu, H.; Larson, R. G., Evaporation of a sessile droplet on a substrate. *Journal of Physical Chemistry B* 2002**,** 106, 1334-1344.

22. Girard, F.; Antoni, M.; Sefiane, K., On the effect of Marangoni flow on evaporation rates of heated water drops. *Langmuir* 2008**,** 24, 9207-9210.

23. Dunn, G. J.; Wilson, S. K.; Duffy, B. R.; David, S.; Sefiane, K., A mathematical model for the evaporation of a thin sessile liquid droplet: Comparison between experiment and theory. *Colloids and Surfaces a-Physicochemical and Engineering Aspects* 2008**,** 323, 50-55.

24. Starov, V.; Sefiane, K., On evaporation rate and interfacial temperature of volatile sessile drops. *Colloids and Surfaces a-Physicochemical and Engineering Aspects* 2009**,** 333, 170-174.

25. Barash, L. Y.; Bigioni, T. P.; Vinokur, V. M.; Shchur, L. N., Evaporation and fluid dynamics of a sessile drop of capillary size. *Physical Review E* 2009**,** 79, 046301.

26. Bourges-Monnier, C.; Shanahan, M. E. R., Influence of Evaporation on Contact Angle. *Langmuir* 1995**,** 11, 2820-2829.

27. Cazabat, A.-M.; Guena, G., Evaporation of macroscopic sessile droplets. *Soft Matter* 2010**,** 6, 2591-2612.

28. Ristenpart, W. D.; Kim, P. G.; Domingues, C.; Wan, J.; Stone, H. A., Influence of substrate conductivity on circulation reversal in evaporating drops. *Physical Review Letters* 2007**,** 99, 234502-234504.

29. Kuncicky, D. M.; Velev, O. D., Surface-Guided Templating of Particle Assemblies Inside Drying Sessile Droplets†. *Langmuir* 2007**,** 24, 1371-1380.

30. Kuncicky, D. M.; Velev, O. D., Surface-guided templating of particle assemblies inside drying sessile droplets. *Langmuir* 2008**,** 24, 1371-1380.

31. Eggers, J., Nonlinear dynamics and breakup of free-surface flows. *Reviews of Modern Physics* 1997**,** 69, 865-929.

32. Jang, D.; Kim, D.; Moon, J., Influence of Fluid Physical Properties on Ink-Jet Printability. *Langmuir* 2009**,** 25, 2629-2635.

33. Furbank, R. J.; Morris, J. F., An experimental study of particle effects on drop formation. *Physics of Fluids* 2004**,** 16, 1777-1790.

34. Rioboo, R.; Voue, M.; Adao, H.; Conti, J.; Vaillant, A.; Seveno, D.; De Coninck, J., Drop Impact on Soft Surfaces: Beyond the Static Contact Angles. *Langmuir* 2010**,** 26, 4873-4879.

35. Rioboo, R.; Marengo, M.; Tropea, C., Time evolution of liquid drop impact onto solid, dry surfaces. *Experiments in Fluids* 2002**,** 33, 112-124.

36. Deegan, R. D.; Bakajin, O.; Dupont, T. F.; Huber, G.; Nagel, S. R.; Witten, T. A., Contact line deposits in an evaporating drop. *Physical Review E* 2000**,** 62, 756-765.

37. Deegan, R. D.; Bakajin, O.; Dupont, T. F.; Huber, G.; Nagel, S. R.; Witten, T. A., Capillary flow as the cause of ring stains from dried liquid drops. *Nature* 1997**,** 389, 827-829.

38. Chhasatia, V. H.; Sun, Y., Interaction of bi-dispersed particles with contact line in an evaporating colloidal drop. *Soft Matter* 2011**,** 7, 10135-10143.

39. Hu, H.; Larson, R. G., Marangoni effect reverses coffee-ring depositions. *Journal of Physical Chemistry B* 2006**,** 110, 7090-7094.

40. Park, J.; Moon, J., Control of colloidal particle deposit patterns within picoliter droplets ejected by ink-jet printing. *Langmuir* 2006**,** 22, 3506-3513.

41. Lim, J. A.; Lee, W. H.; Lee, H. S.; Lee, J. H.; Park, Y. D.; Cho, K., Self-Organization of Ink-jet-Printed Triisopropylsilylethynyl Pentacene via Evaporation-Induced Flows in a Drying Droplet. *Advanced Functional Materials* 2008**,** 18, 229-234.

42. Loudet, J. C.; Alsayed, A. M.; Zhang, J.; Yodh, A. G., Capillary Interactions Between Anisotropic Colloidal Particles. *Physical Review Letters* 2005**,** 94, 018301.

43. Park, B. J.; Furst, E. M., Attractive interactions between colloids at the oil-water interface. *Soft Matter* 2011**,** 7, 7676-7682.

44. Yunker, P. J.; Still, T.; Lohr, M. A.; Yodh, A. G., Suppression of the coffee-ring effect by shape-dependent capillary interactions. *Nature* 2011**,** 476, 308-311.

45. Duineveld, P. C., The stability of ink-jet printed lines of liquid with zero receding contact angle on a homogeneous substrate. *Journal of Fluid Mechanics* 2003**,** 477, 175-200.

46. Davis, S. H., Moving contact lines and rivulet instabilities .1. The satatic rivulet. *Journal of Fluid Mechanics* 1980**,** 98, 225-242.

47. Schiaffino, S.; Sonin, A. A., Formation and stability of liquid and molten beads on a solid surface. *Journal of Fluid Mechanics* 1997**,** 343, 95-110.

48. Berker, R., *Intégration des équations du mouvement d'un fluide visqueux incompressible*. Springer-Verlag: 1963; Vol. 8(2).

49. Sparrow, E. M.; Haji-Sheikh, A., Flow and heat transfer in ducts of arbitrary shape with arbitrary thermal boundary conditions. *American Society of Mechanical Engineers -- Transactions -- Journal of Heat Transfer* 1966**,** 88, 351-358.

50. Soltman, D.; Subramanian, V., Inkjet-printed line morphologies and temperature control of the coffee ring effect. *Langmuir* 2008**,** 24, 2224-2231.

51. Sankir, N. D., Selective deposition of PEDOT/PSS on to flexible substrates and tailoring the electrical resistivity by post treatment. *Circuit World* 2008**,** 34, 32-37.

52. Moon, J.; Grau, J. E.; Knezevic, V.; Cima, M. J.; Sachs, E. M., Ink-Jet Printing of Binders for Ceramic Components. *Journal of the American Ceramic Society* 2002**,** 85, 755-762.

53. Stringer, J.; Derby, B., Limits to feature size and resolution in inkjet printing. *Journal of the European Ceramic Society* 2009**,** 29, 913-918.

54. Stringer, J.; Derby, B., Formation and Stability of Lines Produced by Inkjet Printing. *Langmuir* 2010**,** 26, 10365-10372.

55. Van Osch, T. H. J.; Perelaer, J.; De Laat, A. W. M.; Schubert, U. S., Inkjet printing of narrow conductive tracks on untreated polymeric substrates. *Adv Mater* 2008**,** 20, 343-345.

56. van Osch, T. H. J.; Perelaer, J.; de Laat, A. W. M.; Schubert, U. S., Inkjet printing of narrow conductive tracks on untreated polymeric substrates. *Advanced Materials* 2008**,** 20, 343-345.

57. Smith, P.; Shin, D. Y.; Stringer, J.; Derby, B.; Reis, N., Direct ink-jet printing and low temperature conversion of conductive silver patterns. *Journal of Materials Science* 2006**,** 41, 4153-4158.

58. Wu, J.-T.; Hsu, S. L.-C.; Tsai, M.-H.; Hwang, W.-S., Direct Inkjet Printing of Silver Nitrate/Poly(N-vinyl-2-pyrrolidone) Inks To Fabricate Silver Conductive Lines. *The Journal of Physical Chemistry C* 2010**,** 114, 4659-4662.

59. Jolke, P.; et al., One-step inkjet printing of conductive silver tracks on polymer substrates. *Nanotechnology* 2009**,** 20, 165303.

60. Kang, B. J.; Oh, J. H., Geometrical characterization of inkjet-printed conductive lines of nanosilver suspensions on a polymer substrate. *Thin Solid Films* 2010**,** 518, 2890-2896.

61. Jahn, S. F.; Blaudeck, T.; Baumann, R. R.; Jakob, A.; Ecorchard, P.; Ruffer, T.; Lang, H.; Schmidt, P., Inkjet Printing of Conductive Silver Patterns by Using the First Aqueous Particle-Free MOD Ink without Additional Stabilizing Ligands. *Chemistry of Materials* 2010**,** 22, 3067-3071.

62. van den Berg, A. M. J.; de Laat, A. W. M.; Smith, P. J.; Perelaer, J.; Schubert, U. S., Geometric control of inkjet printed features using a gelating polymer. *Journal of Materials Chemistry* 2007**,** 17, 677-683.

63. Kim, D.; Jeong, S.; Park, B. K.; Moon, J., Direct writing of silver conductive patterns: Improvement of film morphology and conductance by controlling solvent compositions. *Applied Physics Letters* 2006**,** 89, 264101.

64. Tekin, E.; de Gans, B.-J.; Schubert, U. S., Ink-jet printing of polymers - from single dots to thin film libraries. *Journal of Materials Chemistry* 2004**,** 14, 2627-2632.

65. Kang, H.; Soltman, D.; Subramanian, V., Hydrostatic Optimization of Inkjet-Printed Films. *Langmuir* 2010**,** 26, 11568-11573.

66. Soltman, D.; Smith, B.; Kang, H.; Morris, S. J. S.; Subramanian, V., Methodology for Inkjet Printing of Partially Wetting Films. *Langmuir* 2010**,** 26, 15686-15693.

67. Xia, Y.; Friend, R. H., Controlled Phase Separation of Polyfluorene Blends via Inkjet Printing. *Macromolecules* 2005**,** 38, 6466-6471.

68. Xia, Y. J.; Friend, R. H., Nonlithographic patterning through inkjet printing via holes. *Applied Physics Letters* 2007**,** 90.

69. van den Berg, A. M. J.; Smith, P. J.; Perelaer, J.; Schrof, W.; Koltzenburg, S.; Schubert, U. S., Inkjet printing of polyurethane colloidal suspensions. *Soft Matter* 2007**,** 3, 238-243.

70. Ingrosso, C.; Kim, J. Y.; Binetti, E.; Fakhfouri, V.; Striccoli, M.; Agostiano, A.; Curri, M. L.; Brugger, J., Drop-on-demand inkjet printing of highly luminescent CdS and CdSe@ZnS nanocrystal based nanocomposites. *Microelectronic Engineering* 2009**,** 86, 1124-1126.

71. Joo Yeon, K.; Ingrosso, C.; Fakhfouri, V.; Striccoli, M.; Agostiano, A.; Curri, M. L.; Brugger, J., Inkjet-printed multicolor arrays of highly luminescent nanocrystal-based nanocomposites. *Small* 2009**,** 5, 1051-1057.

72. Böhmer, M. R.; Schroeders, R.; Steenbakkers, J. A. M.; de Winter, S. H. P. M.; Duineveld, P. A.; Lub, J.; Nijssen, W. P. M.; Pikkemaat, J. A.; Stapert, H. R., Preparation of monodisperse polymer particles and capsules by ink-jet printing. *Colloids and Surfaces A: Physicochemical and Engineering Aspects* 2006**,** 289, 96-104.

73. Kim, D.; Jeong, Y.; Song, K.; Park, S.-K.; Cao, G.; Moon, J., Inkjet-Printed Zinc Tin Oxide Thin-Film Transistor. *Langmuir* 2009**,** 25, 11149-11154.

74. Bhatti, A. R.; Mott, M.; Evans, J. R. G.; Edirisinghe, M. J., PZT pillars for 1-3 composites prepared by ink-jet printing. *Journal of Materials Science Letters* 2001**,** 20, 1245-1248.

75. Bathurst, S. P.; Kim, S. G., Designing direct printing process for improved piezoelectric micro-devices. *CIRP Annals - Manufacturing Technology* 2009**,** 58, 193-196.

76. Adler-Abramovich, L.; Gazit, E., Controlled patterning of peptide nanotubes and nanospheres using inkjet printing technology. *Journal of Peptide Science* 2008**,** 14, 217-223.

77. Boberl, M.; Kovalenko, M. V.; Gamerith, S.; List, E. J. W.; Heiss, W., Inkjet-printed nanocrystal photodetectors operating up to 3 m wavelengths. *Advanced Materials* 2007**,** 19, 3574-3578.

78. de Gans, B. J.; Hoeppener, S.; Schubert, U. S., Polymer relief microstructures by inkjet etching. *Journal of Materials Chemistry* 2007**,** 17, 3045-3050.

79. Jahn, S. F.; Engisch, L.; Baumann, R. R.; Ebert, S.; Goedel, W. A., Polymer microsieves manufactured by inkjet technology. *Langmuir* 2009**,** 25, 606-610.

80. Bietsch, A.; Zhang, J. Y.; Hegner, M.; Lang, H. P.; Gerber, C., Rapid functionalization of cantilever array sensors by inkjet printing. *Nanotechnology* 2004**,** 15, 873-880.

81. Abe, K.; Suzuki, K.; Citterio, D., Inkjet-printed microfluidic multianalyte chemical sensing paper. *Analytical Chemistry* 2008**,** 80, 6928-6934.

82. Abe, K.; Kotera, K.; Suzuki, K.; Citterio, D., Inkjet-printed paperfluidic immuno-chemical sensing device. *Analytical and Bioanalytical Chemistry* 2010**,** 398, 885-893.

83. Zakir Hossain, S. M.; Luckham, R. E.; Smith, A. M.; Lebert, J. M.; Davies, L. M.; Pelton, R. H.; Filipe, C. D. M.; Brennan, J. D., Development of a bioactive paper sensor for detection of neurotoxins using piezoelectric inkjet printing of sol-gel-derived bioinks. *Analytical Chemistry* 2009**,** 81, 5474-5483.

84. Blau, A.; Ugniwenko, T., Induction and analysis of cell adhesion and differentiation on inkjet micropatterned substrates. *Physica Status Solidi C* 2007**,** 4, 1873-1876.

85. Xu, T.; Petridou, S.; Lee, E. H.; Roth, E. A.; Vyavahare, N. R.; Hickman, J. J.; Boland, T., Construction of High-Density Bacterial Colony Arrays and Patterns by the Ink-Jet Method. *Biotechnology and Bioengineering* 2004**,** 85, 29-33.

86. Roth, E. A.; Xu, T.; Das, M.; Gregory, C.; Hickman, J. J.; Boland, T., Inkjet printing for high-throughput cell patterning. *Biomaterials* 2004**,** 25, 3707-3715.

87. Boland, T.; Xu, T.; Damon, B. J.; Manley, B.; Kesari, P.; Jalota, S.; Bhaduri, S., Drop-on-demand printing of cells and materials for designer tissue constructs. *Materials Science & Engineering C, Biomimetic and Supramolecular Systems* 2007**,** 27, 372-376.

88. Xu, T.; Jin, J.; Gregory, C.; Hickman, J. J.; Boland, T., Inkjet printing of viable mammalian cells. *Biomaterials* 2005**,** 26, 93-99.

89. Di Biase, M.; Saunders, R. E.; Tirelli, N.; Derby, B., Inkjet printing and cell seeding thermoreversible photocurable gel structures. *Soft Matter* 2011**,** 7, 2639-2646.

90. Hoth, C. N.; Choulis, S. A.; Schilinsky, P.; Brabec, C. J., High photovoltaic performance of inkjet printed polymer: Fullerene blends. *Advanced Materials* 2007**,** 19, 3973-3978.

91. Hoth, C. N.; Schilinsky, P.; Choulis, S. A.; Brabec, C. J., Printing highly efficient organic solar cells. *Nano Letters* 2008**,** 8, 2806-2813.

92. Aernouts, T.; Aleksandrov, T.; Girotto, C.; Genoe, J.; Poortmans, J., Polymer based organic solar cells using ink-jet printed active layers. *Applied Physics Letters* 2008**,** 92, 033306.

93. Eom, S. H.; Senthilarasu, S.; Uthirakumar, P.; Yoon, S. C.; Lim, J.; Lee, C.; Lim, H. S.; Lee, J.; Lee, S.-H., Polymer solar cells based on inkjet-printed PEDOT:PSS layer. *Organic Electronics: physics, materials, applications* 2009**,** 10, 536-542.

94. Derby, B., Inkjet printing of functional and structural materials: Fluid property requirements, feature stability, and resolution. *Annual Review of Materials Research* 2010**,** 40, 395-414.

95. Calvert, P., Inkjet Printing for Materials and Devices. *Chemistry of Materials* 2001**,** 13, 3299-3305.

96. de Gans, B. J.; Duineveld, P. C.; Schubert, U. S., Inkjet printing of polymers: State of the art and future developments. *Advanced Materials* 2004**,** 16, 203-213.

97. Yu, D. G.; Zhu, L. M.; Branford-White, C. J.; Yang, X. L., Three-dimensional printing in pharmaceutics: Promises and problems. *Journal of Pharmaceutical Sciences* 2008**,** 97, 3666-3690.

98. Derby, B., Bioprinting: inkjet printing proteins and hybrid cell-containing materials and structures. *Journal of Materials Chemistry* 2008**,** 18, 5717-5721.

99. Tekin, E.; Smith, P. J.; Schubert, U. S., Inkjet printing as a deposition and patterning tool for polymers and inorganic particles. *Soft Matter* 2008**,** 4, 703-713.

100. Delaney, J. T.; Smith, P. J.; Schubert, U. S., Inkjet printing of proteins. *Soft Matter* 2009**,** 5, 4866-4877.

101. Singh, M.; Haverinen, H. M.; Dhagat, P.; Jabbour, G. E., Inkjet Printing-Process and Its Applications. *Advanced Materials* 2010**,** 22, 673-685.

102. Mathews, N.; Lam, Y. M.; Mhaisalkar, S. G.; Grimsdale, A. C., Printing materials for electronic devices. *International Journal of Materials Research* 2010**,** 101, 236-250.

103. Perelaer, J.; Smith, P. J.; Mager, D.; Soltman, D.; Volkman, S. K.; Subramanian, V.; Korvink, J. G.; Schubert, U. S., Printed electronics: The challenges involved in printing devices, interconnects, and contacts based on inorganic materials. *Journal of Materials Chemistry* 2010**,** 20, 8446-8453.

104. Boland, T.; Xu, T.; Damon, B.; Cui, X., Application of inkjet printing to tissue engineering. *Biotechnology Journal* 2006**,** 1, 910-917.

105. Hauschild, S.; Lipprandt, U.; Rumplecker, A.; Borchert, U.; Rank, A.; Schubert, R.; Forster, S., Direct preparation and loading of lipid and polymer vesicles using inkjets. *Small* 2005**,** 1, 1177-1180.

106. Xue, C.-Y.; Yang, K.-L., Chemical Modifications of Inert Organic Monolayers with Oxygen Plasma for Biosensor Applications. *Langmuir* 2007**,** 23, 5831-5835.

107. Anderson, D. M.; Davis, S. H., The spreading of volatile liquid droplets on heated surfaces. *Physics of Fluids* 1995**,** 7, 248-65.

108. Ajaev, V. S.; Gambaryan-Roisman, T.; Stephan, P., Static and dynamic contact angles of evaporating liquids on heated surfaces. *Journal of Colloid and Interface Science* 2010**,** 342, 550-558.

109. Haverinen, H. M.; Myllyla, R. A.; Jabbour, G. E., Inkjet printing of light emitting quantum dots. *Applied Physics Letters* 2009**,** 94, 073108.

110. Walther, M.; Ortner, A.; Meier, H.; Loffelmann, U.; Smith, P. J.; Korvink, J. G., Terahertz metamaterials fabricated by inkjet printing. *Applied Physics Letters* 2009**,** 95, 251107.

111. Picknett, R. G.; Bexon, R., The evaporation of sessile or pendant drops in still air. *Journal of Colloid and Interface Science* 1977**,** 61, 336-350.

112. Sangani, A. S.; Lu, C.; Su, K.; Schwarz, J. A., Capillary force on particles near a drop edge resting on a substrate and a criterion for contact line pinning. *Physical Review E* 2009**,** 80, 011603.

113. Biswas, S.; Gawande, S.; Bromberg, V.; Sun, Y., Effects of Particle Size and Substrate Surface Properties on Deposition Dynamics of Inkjet-Printed Colloidal Drops for Printable Photovoltaics Fabrication. *Journal of Solar Energy Engineering* 2010**,** 132, 021010.

114. Wong, T.-S.; Chen, T.-H.; Shen, X.; Ho, C.-M., Nanochromatography Driven by the Coffee Ring Effect. *Anal Chem* 2011**,** 83, 1871-1873.

115. Jung, J.-Y.; Kwak, H.-Y., Separation of microparticles and biological cells inside an evaporating droplet using dielectrophoresis. *Analytical Chemistry* 2007**,** 79, 5087-5092.

116. Jung, J.-Y.; Young, W. K.; Jung, Y. Y., Behavior of particles in an evaporating didisperse colloid droplet on a hydrophilic surface. *Analytical Chemistry* 2009**,** 81, 8256-8259.

117. Jung, J.-Y.; Kim, Y. W.; Yoo, J. Y.; Koo, J.; Kang, Y. T., Forces acting on a single particle in an evaporating sessile droplet on a hydrophilic surface. *Analytical Chemistry* 2010**,** 82, 784-788.

118. Hodges, C. S.; Ding, Y.; Biggs, S., The influence of nanoparticle shape on the drying of colloidal suspensions. *Journal of Colloid and Interface Science* 2010**,** 352, 99-106.

119. Monteux, C. c.; Lequeux, F. o., Packing and Sorting Colloids at the Contact Line of a Drying Drop. *Langmuir* 2011**,** 27, 2917-2922.

120. Weon, B. M.; Je, J. H., Capillary force repels coffee-ring effect. *Physical Review E* 2010**,** 82, 015305.

121. Poulard, C.; Benichou, O.; Cazabat, A. M., Freely receding evaporating droplets. *Langmuir* 2003**,** 19, 8828-8834.

122. Elimelech, M. G., J.; Jia, X.; Williams, R., A.;, *Particle deposition and aggregation*. 1 ed.; Butterworth Heinemann publication: Woburn, MA, 1998.

123. Hogg, R.; Healy, T. W.; Fuerstenau, D. W., Mutual coagulation of colloidal dispersions. *Transactions of the Faraday Society* 1966**,** 62, 1638-1651.

124. Visser, J., On Hamaker constants: A comparison between Hamaker constants and Lifshitz-van der Waals constants. *Advances in Colloid and Interface Science* 1972**,** 3, 331-363.

125. Chhasatia, V. H.; Joshi, A. S.; Sun, Y., Effect of relative humidity on contact angle and particle deposition morphology of an evaporating colloidal drop. *Applied Physics Letters* 2010**,** 97, 231909.

126. Ristenpart, W. D.; McCalla, P. M.; Roy, R. V.; Stone, H. A., Coalescence of spreading droplets on a wettable substrate. *Physical Review Letters* 2006**,** 97, 064501-1.

127. Kapur, N.; Gaskell, P. H., Morphology and dynamics of droplet coalescence on a surface. *Physical Review E (Statistical, Nonlinear, and Soft Matter Physics)* 2007**,** 75, 56315-1.

128. Menchaca-Rocha, A.; Martinez-Davalos, A.; Nunez, R.; Popinet, S.; Zaleski, S., Coalescence of liquid drops by surface tension. *Physical Review E (Statistical, Nonlinear, and Soft Matter Physics)* 2001**,** 63, 046309-1.

129. Nilsson, M. A.; Rothstein, J. P., The effect of contact angle hysteresis on droplet coalescence and mixing. *Journal of Colloid and Interface Science* 2011**,** 363, 646-654.

130. Andrieu, C.; Beysens, D. A.; Nikolayev, V. S.; Pomeau, Y., Coalescence of sessile drops. *Journal of Fluid Mechanics* 2002**,** 453, 427-438.

131. Aarts, D.; Lekkerkerker, H. N. W.; Guo, H.; Wegdam, G. H.; Bonn, D., Hydrodynamics of droplet coalescence. *Physical Review Letters* 2005**,** 95.

132. Borcia, R.; Bestehorn, M., On the coalescence of sessile drops with miscible liquids. *The European Physical Journal E: Soft Matter and Biological Physics* 2011**,** 34, 1-9.

133. Castrejon-Pita, J. R.; Betton, E. S.; Kubiak, K. J.; Wilson, M. C. T.; Hutchings, I. M., The dynamics of the impact and coalescence of droplets on a solid surface. *Biomicrofluidics* 2011**,** 5.

134. Hamamoto, Y.; Christy, J. R. E.; Sefiane, K., Order-of-magnitude increase in flow velocity driven by mass conservation during the evaporation of sessile drops. *Physical Review E - Statistical, Nonlinear, and Soft Matter Physics* 2011**,** 83.

135. Deegan, R. D., Pattern formation in drying drops. *Physical Review E* 2000**,** 61, 475-485.

136. Ko, H.-Y.; Park, J.; Shin, H.; Moon, J., Rapid self-assembly of monodisperse colloidal spheres in an ink-jet printed droplet. *Chemistry of Materials* 2004**,** 16, 4212-4215.

137. Loudet, J. C.; Yodh, A. G.; Pouligny, B., Wetting and Contact Lines of Micrometer-Sized Ellipsoids. *Physical Review Letters* 2006**,** 97, 018304.

138. Bensimon, A.; Simon, A.; Chiffaudel, A.; Croquette, V.; Heslot, F.; Bensimon, D., Alignment and sensitive detection of DNA by a moving interface. *Science* 1994**,** 265, 2096-2098.

139. Dugas, V.; Broutin, J.; Souteyrand, E., Droplet evaporation study applied to DNA chip manufacturing. *Langmuir* 2005**,** 21, 9130-9136.

140. Smalyukh, I. I.; Zribi, O. V.; Butler, J. C.; Lavrentovich, O. D.; Wong, G. C. L., Structure and dynamics of liquid crystalline pattern formation in drying droplets of DNA. *Physical Review Letters* 2006**,** 96.

141. Patla, I.; Acharya, S.; Zeiri, L.; Israelachvili, J.; Efrima, S.; Golan, Y., Synthesis, two-dimensional assembly, and surface pressure-induced coalescence of ultranarrow PbS nanowires. *Nano Letters* 2007**,** 7, 1459-1462.

142. Duggal, R.; Hussain, F.; Pasquali, M., Self-assembly of single-walled carbon nanotubes into a sheet by drop drying. *Advanced Materials* 2006**,** 18, 29-34.

143. Monteux, C.; Jung, E.; Fuller, G. G., Mechanical Properties and Structure of Particle Coated Interfaces: Influence of Particle Size and Bidisperse 2D Suspensions. *Langmuir* 2007**,** 23, 3975-3980.

144. Madivala, B.; Fransaer, J.; Vermant, J., Self-Assembly and Rheology of Ellipsoidal Particles at Interfaces. *Langmuir* 2009**,** 25, 2718-2728.

145. Keville, K. M.; Franses, E. I.; Caruthers, J. M., Preparation and characterization of monodisperse polymer microspheroids. *Journal of Colloid and Interface Science* 1991**,** 144, 103-126.

146. Ho, C. C.; Keller, A.; Odell, J. A.; Ottewill, R. H., Monodisperse ellipsoidal polystyrene latex particles: preparation and characterisation. *Polymer International* 1993**,** 30, 207-211.

147. Ho, C. C.; Keller, A.; Odell, J. A.; Ottewill, R. H., Preparation of monodisperse ellipsoidal polystyrene particles. *Colloid and Polymer Science* 1993**,** 271, 469-479.

148. Xing, K. Z.; Fahlman, M.; Chen, X. W.; Inganas, O.; Salaneck, W. R., Electronic structure of poly(3,4-ethylene-dioxythiophene): Studied by XPS and UPS. *Synthetic Metals* 1997**,** 89, 161-165.

149. Chen, B.; Cui, T.; Liu, Y.; Varahramyan, K., All-polymer RC filter circuits fabricated with inkjet printing technology. *Solid-State Electronics* 2003**,** 47, 841-847.

150. Lee, D. J.; Oh, J. H. In *Shapes and morphologies of inkjet-printed nanosilver dots on glass substrates*, Southern Gate, Chichester, West Sussex, PO19 8SQ, United Kingdom, 2010; John Wiley and Sons Ltd: Southern Gate, Chichester, West Sussex, PO19 8SQ, United Kingdom, 2010; pp 1261-1265.

151. Chunying, W.; Chaoxia, W., Surface pretreatment of polyester fabric for ink jet printing with radio frequency O2 plasma. *Fibers and Polymers* 2010**,** 11, 87-92.

152. Chunming, Z.; Kuanjun, F., Surface modification of polyester fabrics for inkjet printing with atmospheric-pressure air/Ar plasma. *Surface & Coatings Technology* 2009**,** 203, 2058-63.

153. Kuanjun, F.; Chunming, Z., Surface physical-morphological and chemical changes leading to performance enhancement of atmospheric pressure plasma treated polyester fabrics for inkjet printing. *Applied Surface Science* 2009**,** 255, 7561-7.

154. http://www.nrel.gov/ncpv/images/efficiency_chart.jpg

155. Dang, M. T.; Hirsch, L.; Wantz, G., P3HT:PCBM, best seller in polymer photovoltaic research. *Advanced Materials* 2011**,** 23, 3597-3602.

156. Hoth, C. N.; Choulis, S. A.; Schilinsky, P.; Brabec, C. J., High photovoltaic performance of inkjet printed polymer:Fullerene blends. *Advanced Materials* 2007**,** 19, 3973-3978.

157. Majidi, H.; Baxter, J. B., Electrodeposition of CdSe coatings on ZnO nanowire arrays for extremely thin absorber solar cells. *Electrochimica Acta* 2011**,** 56, 2703-2711.

158. McPeak, K. M.; Baxter, J. B., Microreactor for high-yield chemical bath deposition of semiconductor nanowires: ZnO nanowire case study. *Industrial and Engineering Chemistry Research* 2009**,** 48, 5954-5961.

159. Schilinsky, P.; Asawapirom, U.; Scherf, U.; Biele, M.; Brabec, C. J., Influence of the Molecular Weight of Poly(3-hexylthiophene) on the Performance of Bulk Heterojunction Solar Cells. *Chemistry of Materials* 2005**,** 17, 2175-2180.

Appendix A: EXPERIMENTAL PROCEDURE

The ink is prepared by diluting the Invitrogen ink with DI water and sonicating for two hours. Then the ink is put in the reservoir and then the computer is used to send a waveform for piezoelectric nozzle (40 to 150 μm in diameter) through a waveform generator to get pico liter drops (100 to 200 pico liters). A pneumatic controller is used to maintain a constant pressure in the reservoir. The waveform generator sends a pulse to a delay generator, which sends synchronized pulses to a CCD camera and a strobe light. The camera and strobe light, in synchronization with the jetting, forms a drop observation system to confirm repeatable drop formation. The delay generator sends synchronized signals to CCD camera and strobe light to observe drop formation. The humidity chamber is used to control the humidity in the chamber by controlling the flow of dry/wet air.

The substrates are prepared by coating OTS on glass substrates and then using plasma treatment for different duration. The goniometer is used to measure advancing and receding contact of the substrates. After obtaining repeatable drops, the printhead assembly is moved to jet on a targeted substrate. Then drop evaporation is observed by side-view and through a transparent glass, PET and PEN substrates using an inverted microscope. The bottom view of the evaporating drop is obtained through a CCD camera attached with the fluorescence microscope. ImageJ is used to measure contact angles and contact area of the drops.

VITA

Viral Chhasatia was born on August 20, 1984 to Harendrasinh and Anilaben Chhasatia. He and his younger brother, Anup, grew up in Vadodara, Gujarat India. Viral has long loved reading and travelling. In recent years, all of these interests have served as stress relief from the mental rigors of college and graduate school. Viral's interest in science was first piqued at a very young age by his parents, who encouraged him to read and think independently. His interest grew and expanded as he was introduced to chemistry, physics, history and astronomy while in grade school.

Viral went off to Faculty of Technology & Engineering in his hometown Vadodara, much to his parents' delight. He graduated with his Bachelor of Engineering in Mechanical Engineering in 2006 with distinction. Then upon receiving Dr. Bhagawan Gajwani Fellowship at Binghamton University, NY he joined Master of Science in Mechanical Engineering in Fall of 2007. There he met his mentor Dr. Ying Sun and completed his MS in Mechanical Engineering under her guidance on the topic of characterization of thermal interface materials using flash diffusivity and infrared microscopy methods. Upon graduation, he joined Drexel University where he has since worked in the field of colloid science. He got married to Unnati in 2011 while working on his PhD.

Education

- **Ph.D.** Mechanical Engineering, (GPA: 3.94/4)

Drexel University, PA March 2012

- **M.S.** Mechanical Engineering, (GPA: 3.46/4)

SUNY at Binghamton, NY August 2009

- **B.E.** Mechanical Engineering, (First class with distinction)

Faculty of Tech. & Engg., India July 2006

Thesis and project work

- **PhD Dissertation**: Solvent Evaporation and Particle Deposition of Colloidal Drops in Inkjet Printing Process. (Advisor: Dr. Ying Sun)
- **Masters Thesis:** Characterization of Thermal Interface Materials using Flash Diffusivity and Infrared Microscopy Methods. (Advisor: Dr. Ying Sun)
- **Undergraduate Project:** Design Development and Fabrication of Embedded Controller for Pneumatic Engine. (Advisor: Praful Desai)

Professional experience

- **Graduate Research Assistant, Complex Fluids and Multiphase Transport Lab at Drexel University (Sep'09 to Present)**
  - Performed in-situ experiments to examine particle deposition and interaction of inkjet printed evaporating colloidal drops
  - Designed an in-situ observation system for formation, impact and deposition of inkjet printed colloidal drop
  - Built a solar cell tester to test inkjet printed conventional and inverted solar

cells

- Supervised three undergraduate senior design projects, two NSF-REU student projects and two Hess honors' students in building a goniometer, and an environmental chamber

- **Graduate Research Assistant, Computational Materials & Multiphase Flows Lab at SUNY Binghamton (Sep'07 to Aug'09)**
  - Characterization thermal properties of nano-structured thermal interface materials using flash diffusivity, differential scanning calorimetry and infrared microscopy techniques
  - Designed a horizontal thermal gradient stage for testing nano-structured thermal interface materials
  - Carried out thermal and thermomechanical analysis in electronics packaging using ANSYS and Comsol software packages
- **Summer Internship at Larsen &Toubro (May'05 to Jun'05)**
  - Summarized submerged arc welding and electro slag strip cladding for hi-pressure vessels

Journal publications

1. V Chhasatia, A Joshi, Y Sun, "Effect of relative humidity on contact angle and particle deposition morphology of an evaporating colloidal drop", Applied Physics Letters 2010, 97, 231909.
2. V Chhasatia, Y Sun, "Interaction of bi-dispersed particles with contact line in an evaporating colloidal drop", Soft Matter 2011, 7, 10135-10143.
3. M Fleischman, B Lee, V Rodriguez-Santiago, V Chhasatia, Y Sun, D Pappas,

"Hybrid Method Involving Atmospheric Plasma Treatment and Inkjet Deposition for the Development of Conductive Patterns on Flexible Polymers", Surface and Coatings Technology 2012 (Accepted), SURFCOAT-D-11-02628.

Conference publications

1. V Chhasatia, Y Sun, F Zhou, L Huang, H Wang, "Design optimization of custom engineered silver-nanoparticle thermal interface materials," the 11th IEEE Intersociety Conference on Thermal and Thermomechanical Phenomena in Electronic Systems, I-THERM, 419-427, May 2008.
2. V Chhasatia, Y Sun, F Zhou, L Huang, H Wang, "Thermal and thermomechanical analysis of custom engineered ag-nanoparticle thermal interface materials", ASME International Mechanical Engineering Congress & Exposition, IMECE2008 - 68896, Nov 2008.

Conference presentations

1. V Chhasatia, Y Sun, F Zhou, L Huang, H Wang, "Design optimization of custom engineered silver-nanoparticle thermal interface materials," the 11th IEEE Intersociety Conference on Thermal and Thermomechanical Phenomena in Electronic Systems, I-THERM, 419-427, May 2008.
2. V Chhasatia, Y Sun, F Zhou, L Huang, H Wang, "Thermal and thermomechanical analysis of custom engineered ag-nanoparticle thermal interface materials", ASME International Mechanical Engineering Congress & Exposition, IMECE2008 - 68896, Nov 2008.
3. V Chhasatia, M Wang, Y Sun, "3-D Printing of cellular filaments via the drop-on-demand inkjet printing technique", 2010 International Conference on

Biofabrication, P-A213, Philadelphia, PA, October 2010.

4. A Joshi, V Chhasatia, Y Sun, "Particle deposition and assembly of inkjet-printed colloidal drops in line and pattern printing", American Vacuum Society 57th International Symposium & Exhibition, IJ+BI+MN+MoM4, Albuquerque, NM, October 2010.
5. A Joshi, V Chhasatia, Y Sun, "Deposition of bi-dispersed particles in inkjet-printed evaporating colloidal drop", 63rd Annual Meeting of the American Physical Society CS.00008, Long Beach, CA, November 2010.
6. V Chhasatia, A Joshi, Y Sun, "Effect of relative humidity on contact angle of inkjet-printed evaporating colloidal drop", 63rd Annual Meeting of the American Physical Society MS.00007, Long Beach, CA, November 2010.
7. V Chhasatia, A Joshi, Y Sun, "Deposition of bi-dispersed particles in inkjet-printed evaporating colloidal drops", 2010 Materials Research Society Fall Meeting D6.9, Boston, MA, December 2010.
8. D Pappas, V Rodriguez-Santiago, A Bujanda, B Lee, V Chhasatia, Y Sun, "Atmospheric pressure plasma treatment of polymers for ink-jet deposition of flexible solar cell platforms", 38th International Conference on Metallurgical Coatings and Thin Films G3-1, San Diego, CA, May 2011.
9. B Lee, T Perlenfein, V Chhasatia, J Baxter, Y Sun, "Fabrication of Printable Hybrid Solar Cells based on P3HT and ZnO", 5th International Conference on Energy Sustainability 54229, Washington DC, August 2011.
10. V Chhasatia, Y Sun, "Effects of particle number on interaction of particles with contact line in inkjet-printed evaporating colloidal drops", 64rd Annual Meeting

of the American Physical Society M4.00009, Baltimore, MD, November 2011.

11. V Chhasatia, Y Sun, "Interaction of bi-dispersed particles with contact line in inkjet-printed evaporating colloidal drops", 64rd Annual Meeting of the American Physical Society R6.00007, Baltimore, MD, November 2011.
12. B Lee, T Perlenfein, V Chhasatia, J Baxter, Y Sun, "Fabrication of Printable Hybrid Solar Cells based on P3HT and CdSe nanocrystals", Materials Research Society Fall Meeting S4.8, Boston MA, December 2011.

Research skills

- Experimental:
  - In-situ Observation: Fluorescent and Infrared Microscopes, CCD Cameras, Thermal Gradient Stage, Goniometer
  - Material Characterization: Flash Diffusivity Tester, Surface Tensiometer, Differential Scanning Calorimetry, Rheology, Surface Profilometry, Atomic Force Microscopy, Scanning Electron Microscopy
  - Sample Preparation: Thermal Evaporator, Centrifuge, Plasma cleaner, Sonicator, Magnetic Stir, Spin coater
- Computational:
  - Commercial Softwares: ANSYS, COMSOL, LabView, Fluent, Pro-Engineer, AutoCAD, MatLab
  - Programming Languages: C, FORTRAN

Awards

- 2009-10 Dean's Fellowship at Drexel University, PA.
- 2007-08 Dr. Bhagawan Gajwani Fellowship at Binghamton University, NY.